UNIVERSIDADE FEDERAL DE PERNAMBUCO
DEPARTAMENTO DE FÍSICA – CCEN

PROGRAMA DE PÓS-GRADUAÇÃO EM FÍSICA

EUCLIDES CÉSAR LINS ALMEIDA

# ULTRAFAST DYNAMICS OF NANOSCALE SYSTEMS: $NaNbO_3$ NANOCRYSTALS, COLLOIDAL SILVER NANOPARTICLES AND DYE FUNCTIONALIZED $TiO_2$ NANOPARTICLES

Recife
2012

EUCLIDES CÉSAR LINS ALMEIDA

# ULTRAFAST DYNAMICS OF NANOSCALE SYSTEMS: $NaNbO_3$ NANOCRYSTALS, COLLOIDAL SILVER NANOPARTICLES AND DYE FUNCTIONALIZED $TiO_2$ NANOPARTICLES

Tese apresentada ao Programa de Pós-Graduação em Física da Universidade Federal de Pernambuco, como requisito parcial para a obtenção do título de Doutor em Física.

Orientador:
Prof. Dr. Cid Bartolomeu de Araújo
Universidade Federal de Pernambuco

Recife
2012

Catalogação na fonte
Bibliotecário Jefferson Luiz Alves Nazareno CRB 4-1758

A498u Almeida, Euclides César Lins.
Ultrafast dynamics of nanoscale systems: NaNbO3 nanocrystals, colloidal silver nanoparticles and dye functionalized TiO2 nanoparticles / Euclides César Lins Almeida. – 2012.
155f.: fig., tab.

Orientador: Cid Bartolomeu de Araújo.
Tese (Doutorado) – Universidade Federal de Pernambuco. CCEN. Física. Recife, 2012.
Inclui referências e apêndice

1. Óptica não-linear . 2. Dinâmica ultrarrapida . 3. Materiais nanoestruturados Araújo, Cid Bartolomeu (Orientador). II. Titulo.

535 CDD (22. ed.) UFPE-FQ 2016-58

**Universidade Federal de Pernambuco**
**Departamento de Física – CCEN**
**PROGRAMA DE PÓS-GRADUAÇÃO EM FÍSICA**
**Cidade Universitária - 50670-901 Recife PE Brasil**
**Fone (++ 55 81) 2126-7640/2126-8449 - Fax (++ 55 81) 3271-0359**
http://www.ufpe.br/ppgfisica/ e-mail: posgrad@df.ufpe.br

# Parecer da Banca Examinadora de Defesa de Tese de Doutorado

## Euclides César Lins Almeida

## ULTRAFAST DYNAMICS OF NANOSCALE SYSTEMS: $NaNbO_3$ NANOCRYSTALS, COLLOIDAL SILVER NANOPARTICLES AND DYE FUNCTIONALIZED $TiO_2$ NANOPARTICLES

A Banca Examinadora composta pelos Professores Cid Bartolomeu de Araújo (Presidente e Orientador), Leonardo de Souza Menezes (Co-Orientador), José Américo de Miranda Neto, Lúcio Hora Acioli, todos do Departamento de Física da Universidade Federal de Pernambuco, Cleber Renato Mendonça, do Instituto de Física de São Carlos da Universidade de São Paulo e Marcos Assunção Pimenta, do Departamento de Física da Universidade Federal de Minas Gerias, consideram o candidato:

( X ) Aprovado ( ) Reprovado ( ) Em exigência

Secretaria do Programa de Pós-Graduação em Física do Departamento de Física do Centro de Ciências Exatas e da Natureza da Universidade Federal de Pernambuco em trinta de julho de dois mil e doze.

Prof. Cid Bartolomeu de Araújo
Presidente e Orientador

Prof. Leonardo de Souza Menezes
Co-Orientador

Prof. José Américo de Miranda Neto

Prof. Lúcio Hora Acioli

Prof. Cleber Renato Mendonça

Prof. Marcos Assunção Pimenta

# Abstract

The main objective of this work was the investigation of ultrafast optical phenomena in selected nanostructured systems employing different nonlinear spectroscopic techniques, either in the time or the frequency domain. To provide an appropriate background to understand the performed experiments the principles of nonlinear optical spectroscopies are presented. Initially a description of the nonlinear optical response function in the time domain is given. The time evolution of the optical polarization, that gives rise to the spectroscopic signal, is described in detail using a diagrammatic perturbation theory. Nonlinear optical techniques are discussed such as photon echoes, pump-and-probe and hole-burning, as well as how the dynamical behavior of a material can be interpreted from the generated signals. The degenerate four-wave mixing technique with incoherent light was used to investigate for the first time the ultrafast dephasing of excitons in a glass-ceramic containing sodium niobate nanocrystals. The short dephasing time measured ($T_2$ = 20 fs) indicates that different dephasing channels contribute for the excitonic dephasing, namely: electron-electron scattering, electron-phonon coupling and fast trapping of electrons in defects on the nanocrystals interface. Low-temperature luminescence experiments were also performed to measure excitonic and trap states lifetimes. The persistent spectral hole-burning technique was applied to measure localized surface plasmons dephasing times in colloidal silver nanoparticles capped with different stabilizing molecules. The dependence of $T_2$ with three different stabilizers was demonstrated and theoretically analyzed. The results show that the dephasing times are shorter than the theoretically calculated $T_2$ using the bulk dielectric functions of the metal. This discrepancy is attributed to changes in the electronic density of states at the nanoparticles interface caused by the presence of the stabilizers. *Ab-initio* calculations based on the Density Functional Theory were performed to further understand the interaction between the nanoparticles and stabilizing agents. The femtosecond transient absorption technique was employed to study the ultrafast dynamics of in-gap states in a glass-ceramics containing sodium niobate nanocrystals. Two main temporal components were found for the excited state absorption signal: a fast component, with decay time of ≈ 1 ps, and a slower component which is attributed to deep trap states. This slower component is responsible for the excited state absorption contribution in optical limiting experiments previously reported in the literature. The dynamics of the optical limiting in this sample was also studied, in the millisecond range, exciting the sample with a train of femtosecond pulses. The optical limiting behavior reflects the dynamics of population in the excited and trap states and this dynamics was modeled using rate equations for the electronic states' populations. Finally, the pump-and-probe transient absorption technique was employed to investigate charge-transfer processes in colloids with rhodamine 6G and $TiO_2$ nanoparticles. The transient bleaching signal behavior is compared with the one observed for unlinked rhodamine 6G dissolved in ethanol. The analysis of the results allowed the attribution of the bleaching behavior to charge-transfer from thermalized excited states of the dye molecules to the semiconductor conduction band and to the back charge-transfer from the semiconductor to the molecules.

**Keywords**: Ultrafast phenomena, nonlinear optical spectroscopies, nanostructures, excitons, trap states, localized surface plasmons, charge transfer.

# Resumo

O principal objetivo deste trabalho foi investigar fenômenos ópticos ultrarrápidos em sistemas nanoestruturados empregando diferentes técnicas espectroscópicas não lineares, tanto no domínio do tempo quanto no domínio da frequência. Para fornecer uma base adequada que permita entender os experimentos feitos nessa tese, os princípios físicos das espectroscopias ópticas não lineares são apresentados. Inicialmente é apresentada uma descrição da função resposta não linear no domínio do tempo. A evolução temporal da polarização óptica, que gera o sinal espectroscópico, é descrita em detalhes usando uma teoria de perturbação diagramática. Técnicas ópticas não lineares são apresentadas, tais como eco de fótons, bombeamento-e-sonda e *hole burning*, assim como o comportamento dinâmico de um material pode ser interpretado a partir do sinal gerado. A técnica de mistura degenerada de quatro ondas com luz incoerente foi usada para investigar, pela primeira vez, o defasamento ultrarrápido de éxcitons em uma vitrocerâmica contendo nanocristais de niobato de sódio. O tempo de defasamento medido ($T_2$ = 20 fs) indica que diferentes canais contribuem para o defasamento excitônico, a saber: espalhamento elétron-elétron, acoplamento elétron-fônon e armadilhamento rápido de elétrons em defeitos na interface do nanocristal. Experimentos de luminescência a baixas temperaturas também foram realizados para medir os tempos de vida de éxcitons e estados de armadilha. A técnica de *hole burning* espectral persistente foi aplicada para medir os tempos de defasamento de plásmons de superfície localizados em nanopartículas de prata coloidais recobertas por diferentes moléculas estabilizantes. A dependência de $T_2$ com os diferentes estabilizantes foi demonstrada e analisada teoricamente. Os resultados mostram que os tempos de defasamento são mais curtos que os tempos calculados teoricamente usando as funções dielétricas do metal volumar. Essa discrepância é atribuída a mudanças na densidade de estados eletrônica causada pela presença dos estabilizantes. Cálculos de primeiros princípios baseados na teoria do funcional da densidade foram implementados para melhor entender a interação entre as nanopartículas e os agentes estabilizantes. A técnica de absorção transiente de fentossegundos foi empregada para estudar a dinâmica ultrarrápida de estados de energia dentro do *gap* em uma vitrocerâmica contendo nanocristais de niobato de sódio. Duas principais componentes temporais foram encontradas para o sinal de absorção do estado excitado: uma componente rápida, com tempo de decaimento de ≈ 1ps e uma componente mais lenta atribuída a estados de armadilha profunda. Essa componente mais lenta é responsável pela contribuição de absorção de estado excitado nos experimentos de limitação óptica reportados anteriormente na literatura. A dinâmica de limitação óptica nessa amostra também foi estudada, no regime de milissegundos, excitando a amostra com um trem de pulsos de fentossegundos. O comportamento de limitação óptica reflete a dinâmica de população em estados excitados e de armadilha e essa dinâmica foi modelada usando equações de taxa para a população de estados eletrônicos. Finalmente, a técnica de absorção transiente de bombeamento-e-sonda foi empregada para investigar processos de transferência de carga em colóides com nanopartículas de $TiO_2$ e rodamina 6G. O comportamento do sinal de depleção transiente é comparado com o observado para a rodamina livre suspensa em etanol. A análise dos resultados permitiu atribuir o comportamento de depleção à transferência de carga de estados excitados termalizados das moléculas de corante para a banda de condução do semicondutor e a transferência no sentido inverso do semicondutor para as moléculas.

**Palavras-chave:** Fenômenos ultrarrápidos. Espectroscopias ópticas não lineares.
Nanoestruturas. Éxcitons. Estados de armadilha. Plásmons de superfície localizados.
Transferência de carga.

# Resumo Estendido

Existe atualmente um grande interesse no estudo de sistemas nanoestruturados. Nestes sistemas, uma variedade de fenômenos ópticos interessantes, tais como defasamento de éxcitons e de plásmons localizados, separação e transporte de carga e vibrações acústicas coerentes, ocorrem na escala de tempo de fentossegundos.

O objetivo principal dessa tese é a investigação de alguns desses fenômenos ópticos ultrarrápidos em nanomateriais. Para tanto, são utilizadas técnicas espectroscópicas não lineares nos domínios de tempo e frequência.

## Capítulo 2 – Princípios de Espectroscopias Ópticas não Lineares

A base para o entendimento das técnicas experimentais empregadas nessa tese é apresentada no capítulo 2, que versa sobre os fundamentos de espectroscopias ópticas não lineares com ênfase no domínio do tempo. A análise é geral e pode ser estendida para outras técnicas que não estão descritas nessa tese. O princípio básico das técnicas ópticas não lineares é o controle de sucessivas interações luz-matéria que geram uma polarização macroscópica no meio que por sua vez, dá origem ao sinal de interesse. Esse sinal carrega informação das propriedades da luz e do meio. Em particular, informações sobre processos dinâmicos, que estão ocultas em espectroscopias lineares, podem ser extraídas através de técnicas ópticas não lineares. Para acompanhar a evolução temporal do operador densidade que descreve o meio, uma teoria de perturbação diagramática é apresentada. Por fim, espectroscopias não lineares coerentes são descritas em detalhes, tais como eco de fótons, bombeamento-e-sonda e *hole-burning* espectral, bem como se podem obter tempos de relaxação a partir dessas técnicas.

## Capítulo 3 – Dinâmica Ultrarrápida de Éxcitons em uma Vitrocerâmica Contendo Nanocristais de $NaNbO_3$

No capítulo 3, foi empregada a técnica de mistura degenerada de quatro ondas com luz incoerente (MDQOLI) para estudar, pela primeira vez, defasamento excitônico em uma vitrocerâmica contendo nanocristais de niobato de sódio (VC-NNS). A técnica de MDQOLI, que emprega pulsos longos, temporalmente incoerentes, é análoga ao eco de fótons de três pulsos que utiliza pulsos coerentes com duração de fentossegundos. Em vez da largura temporal

do pulso, é o tempo de coerência da luz que determina a resolução temporal em técnicas que empregam luz incoerente. Os aspectos básicos das técnicas espectroscópicas coerentes com luz incoerente são descritos nesse capítulo. A vitrocerâmica estudada contém nanocristais semiconductores de $NaNbO_3$ com um *band-gap* na região do ultravioleta próximo. Esse material tem sido estudado visando a aplicações como limitadores ópticos e chaves totalmente ópticas. O tempo de defasamento de éxcitons medido ($T_2$ = 20 fs) indica que vários canais de relaxação contribuem para o defasamento, a saber: espalhamento elétron-elétron, acoplamento fônon-elétron e rápido armadilhamento de elétrons em defeitos na superfície dos nanocristais. Experimentos de luminescência em baixa temperatura também foram feitos para estudar as propriedades ópticas de éxcitons e estados de armadilha nas VC-SNN. Os tempos de recombinação de éxcitons nos nanocristais de $NaNbO_3$ é da ordem de 25 ns, enquanto o tempo de vida dos estados de armadilha na superfície dos nanocristais é da ordem de 500 ns. Uma banda de luminescência centrada em torno de 690 nm foi observada na amostra sem nanocristais de $NaNbO_3$ sob excitação no ultravioleta abaixo do *band-gap* do material. Essa banda foi atribuída à emissão por centros não compensados por oxigênio frequentemente presentes em vidros com muitos componentes. Esses defeitos contribuem para absorção não linear desse material nos experimentos de limitação óptica reportados na literatura.

## Capítulo 4 – Dinâmica Ultrarrápida de Plásmons de Superfície em Nanopartículas de Prata

No capítulo 4, defasamento ultrarrápido de plásmons localizados de superfície (PLS) em coloides contendo nanopartículas (NPs) de prata é investigado pela técnica de *hole-burning* espectral persistente (HBEP). Para a compreensão dos resultados desse capítulo, é feita uma descrição clássica do efeito de ressonância de plásmons localizados em NPs de metais nobres e os mecanismos que contribuem para o defasamento de PLS são discutidos em detalhes. A técnica de HBEP, que permite eliminar efeitos de alargamento não homogêneo e medir tempos de defasamento de PLS em NPs de diferentes formas e tamanhos, é apresentada. A técnica foi empregada para estudar defasamento de PLS em coloides contendo NPs de prata de dimensões da ordem de 12 nm recobertas com três estabilizantes diferentes (citrato de trisódio – CTS, poli(vinil pirrolidona) – PVP e poli(vinil álcool) – PVA). Os tempos de defasamento foram obtidos com base no modelo da técnica de HBEP e dependem do estabilizante escolhido (3,0; 2,3 e 1,8 fs para CTS, PVP e PVA respectivamente). Além disso, os tempos de defasamento medidos experimentalmente são mais curtos que o tempo calculado teoricamente a partir das constantes dielétricas do metal volumar. Dois mecanismos distintos, que envolvem interação dos elétrons que oscilam coerentemente com a superfície das NPs, foram propostos para explicar essa discrepância do valor de $T_2$: 1) Amortecimento químico de interface (AQI), que é atribuído ao tunelamento de elétrons para as moléculas dos estabilizantes e 2) amortecimento de Landau aumentado, no qual os elétrons oscilantes decaem em pares elétrons-buracos próximos à interface. Em ambos os mecanismos, há uma mudança na densidade eletrônica de estados na superfície causada pela presença dos estabilizantes. Para melhor entender a interação entre as NPs metálicas e as moléculas de estabilizante, foram feitos cálculos de primeiros princípios baseados em teoria do funcional da densidade. Os resultados permitiram observar mudanças na densidade local de estados no metal e identificar transições eletrônicas relevantes que contribuem para AQI.

## Capítulo 5 – Espectroscopia de Bombeamento-e-Sonda em Nanopartículas de $TiO_2$ Funcionalizadas com Rodamina 590 e Vitrocerâmicas Contendo Nanocristais de $NaNbO_3$

No capítulo 5, foram estudados dois problemas distintos: 1) dinâmica de estados dentro do *gap* em VC-SNN e 2) transferência de carga em um coloide de partículas de $TiO_2$ amorfas funcionalizadas com rodamina 590. A dinâmica ultrarrápida de estados dentro do gap em VC-SNN foi estudada usando a técnica de absorção transiente de bombeamento-e-sonda. Pelo menos duas componentes temporais da absorção de estado excitado puderam ser discernidas: uma mais rápida, com tempo de decaimento da ordem de 1 ps, e uma mais lenta que é atribuída a estados de armadilha profunda.

Para se estudar transferência de carga em coloides com partículas amorfas de $TiO_2$ funcionalizadas com rodamina 590 se empregou a técnica de absorção transiente de bombeamento-e-sonda. O sinal de depleção transiente do corante é modificado na presença de nanopartículas de $TiO_2$. Essa mudança foi atribuída à transferência de carga de estados excitados termalizados do corante para a banda de condução do semicondutor e à transferência no sentido inverso do semicondutor para o corante.

O capítulo apresenta ainda um estudo de comportamento dinâmico de limitação óptica nas amostras de vitrocerâmicas contendo nanocristais de $NaNbO_3$ excitando com um trem de pulsos de femtosegundos. Nesse caso a dinâmica é mais lenta (da ordem de centenas de microssegundos) e reflete a dinâmica de população em estados excitados e de armadilha. Um modelo foi proposto para explicar a dinâmica de população usando equações de taxa.

## Capítulo 6 – Conclusões e Perspectivas

O capítulo 6 traz as principais conclusões dos trabalhos realizados nessa tese, que são:

– Medida de $T_2$ = 20 fs associado a éxcitons em nanocristais de $NaNbO_3$.

– Medida de $T_2 \leq 3$ fs associados a plásmons localizados em coloides com nanopartículas de prata e verificação que o estabilizante pode afetar $T_2$.

– Verificação de dinâmica ultrarrápida na absorção de estado excitado em vitrocerâmicas contendo nanocristais de $NaNbO_3$.

– Verificação de processos de transferência de carga de Rodamina 590 para partículas de $TiO_2$.

Por fim, o capítulo aponta sugestões para a eventual solução dos problemas que surgiram durante esse trabalho.

# Agradecimentos

O trabalho desenvolvido nesta tese não seria possível sem a colaboração de muitas pessoas que de alguma forma dedicaram parte dos seus tempos nessa longa jornada de aprendizado e descobrimento. Em particular, sou grato pela orientação do Prof. Cid de Araújo, sobretudo por suas ideias, paciência, incentivo e por ter me dado plena liberdade tanto para criar como para destruir. Uma de suas mais importantes qualidades é permitir (e confiar) que o estudante possa mexer em equipamentos sofisticados e caros sem se preocupar com eventuais erros do estudante. Essa etapa de aprendizado é fundamental na carreira de um físico experimental.

Não menos importante foi a ativa participação do co-orientador Prof. Leonardo Menezes, com quem aprendi boas técnicas de alinhamento óptico e pude discutir em detalhes os resultados. Em particular, faço menção à sua essencial contribuição no modelo de limitação óptica em vitrocerâmicas.

Gostaria de agradecer à contribuição da banca examinadora pelas correções e por apontar trechos que não estavam claros no manuscrito original. Gostaria de agradecer a participação de Prof. José Américo por ter dado sugestões a partir de uma diferente visão e Prof. Lúcio Acioli pelas dicas e por ter me cedido vários equipamentos durante o período desta tese (alguns deles inclusive chegaram a ser danificados, perdão!).

Um importante aspecto desta tese foi contribuição dos colaboradores com ideias e principalmente para a compreensão de fenômenos físicos e químicos: Professores Celso P. de Melo e André Galembeck, desta universidade, Dra. Giovanna Machado do CETENE e Prof. Andrei Lipovskii da St. Petersburg State Polytechnical University. Nesse ponto, devo salientar a contribuição de Dr. Antônio M. Brito-Silva na síntese de nanopartículas, ideias e longas discussões e com quem pude aprender um pouco de química. A motivação e competência de Dr. Augusto C. L. Moreira me manteve também estimulado durante as simulações de DFT. Gostaria também de agradecer a participação de Dr. Kelly Jorge nas simulações usando o método Runge-Kutta. Por último, gostaria de agradecer a colaboração de Andréa Ferreira na síntese de partículas e discussões químicas.

É um grande privilégio contar com um grupo qualificado e estimulante de professores com os quais se possa aprender física de alto nível, de onde destaco os Profs. Alexandre Ricaldi e Marco Sacilotti pelas discussões e pela ajuda no sistema de baixas temperaturas, e Profa. Rita Zorzenon pelo constante apoio. Agradeço também o estímulo do coordenador da pós-graduação, Prof. Ernesto Raposo, durante os momentos finais desta tese.

Sinceros agradecimentos devem ser feitos aos eternos amigos Nick, Regivaldo Filho e Renato Barbosa pela discussões sobre ciência, pelo suporte, pelos momentos de distração e pelos eternos companheirismo e amizade.

Em todo trabalho experimental, a participação do corpo técnico é de suma importância. O compromisso e profissionalismo de Maria Virgínia do laboratório de Química, Marcos Aurélio da Oficina Eletronica e dos funcionários da Criogenia e da Oficina Mecânica não devem ser esquecidos. Agradeço também ao corpo administrativo, em especial a Claudesio, Carlos e Alessandra e ao apoio de Sergio Santos do MEV.

Nos meus sete anos no Laboratório de Óptica Não-Linear, tive o privilégio de conviver com grandes colegas aos quais agradeço a amizade e a troca cientifica: Hans, Luis Arturo, Ernesto Valdes (¡Hasta la Victoria Siempre!), Ronaldo (e Paulinha), Diego Rativa, Denise, Milena, Tâmara, Gemima, Jamil, Murilo, Anderson. Pude também contar com a ajuda dos colegas do Laboratório de Fotônica do Prof. Anderson Gomes, que sempre me dispuseram equipamentos e componentes ópticos. Além do mencionado, esses colegas também me deram suporte durante o período em que fui presidente do Student Chapter da OSA, aos quais se juntam com especial destaque Natália Rodrigues e Douglas Vitoreti, Claudia Brainer, Thiago Lemos. Não posso esquecer também as frutíferas discussões de física com os colegas do Grupo de Óptica e do Departamento de Física: Marco Polo, Eroni, Bernardo Kyotoku, Gerson, Ramon, André e outros.

Durante o período final da minha tese, tive a honra de fazer parte do CETENE, onde fiz muitos amigos e guardarei boas lembranças daqueles que fazem do CETENE um agradável local de trabalho: Lygia Britto, Helissandra Montebello, Juliete Queiroz, Nininha, Flávia, Francisco Rangel, Janaína Viana, Maurício Paiva, Giovanna Machado, Jucimar Morais, Wilson Souza, Andréa Ferreira, Daniel Duarte, Raquel Milani, Adriana, Edwin e Magaly.

À família, minhas desculpas por passar a maior parte do tempo distante e especial agradecimentos às sobrinhas que conheci no final da tese e com quem tive divertidos momentos.

Finalmente, este trabalho não seria possível sem o auxilio financeiro do CNPQ através das bolsas de doutorado e do programa de capacitação institucional. De grande ajuda também cito o *grant* oferecido pela *Optical Society of America* para participação no *Frontiers in Optics* e IONS *conference* e os auxílios financeiros do INCT de fotônica para participação em conferências.

## Contents

# 1. Introduction

In Richard Feynman's visionary talk entitled "*There is plenty of room at the bottom"* delivered at the American Physical Society meeting at Caltech on December 29th, 1959, he spoke about a new field of science in which little had been done at that time, but had an enormous potential in principle [Fe59]. This new field would allow scientists to manipulate and construct systems and devices on a small scale. Perhaps more excitingly would be the possibility of constructing things atom by atom (the bottom-up approach). That talk is considered a landmark for the concepts of the nanoscience. Feynman´s proposals were based on the capabilities of the tools available at the time, such as the electron microscopes. With the advances in electron microscopy and the invention and development of characterization and fabrication tools such as the scanning tunneling [Bi82] and atomic force [Bi86] microscope, lithographic techniques (ion and electron beam) and the improvement of bottom-up methods for synthesis on nanoscale, allied with advances on computer science, nanoscience has been experiencing an enormous advance since the last decade, bringing together scientists from different fields and backgrounds with the ultimate goal to make nanotechnology applications a reality.

But there is still *plenty* of room at the bottom and a lot has to be done to understand basic physical phenomena in mesoscopic systems, where matter can behave differently compared to the large (*bulk*) or the molecular and atomic scale. In particular, there is an interest in investigating the relevant time scales of physical phenomena in nanostructures. In a 10 nm gold nanocube for example, considering the Fermi velocity for bulk Au, $v_f = 1.4\text{x}10^6$ m/s, the Fermi electrons travel from one extreme to the other in $t_{\mathrm{col}} \sim 7$ fs. Thus femtosecond is a relevant time scale when going to nano. Several phenomena at the nanoscale occur on the femto/picosecond temporal range, such as plasmon [Li03a] and exciton dephasing [Wo97], charge separation and transport [Kl00], and coherent acoustic vibrations [Ha06]. The interest in understanding and controlling such phenomena are justified by the potential applications of nanostructures in solar cells [Ga03], optimized biosensors [Wi07], plasmonic devices [Ma05], fast electronic transport and photocatalysis [Be00] among others. Fig 1.1 displays the evolution through the recent years of indexed articles which contains the terms ultrafast and different nanostructures in their topic. It is remarkable the growth of published articles in the subject within the last five years.

The optical and electronic properties of nanostructures are quite sensitive to the surface and hence to the chemical environment. For a 5 nm gold nanoparticle, for example, with bulk-like distance of 0.3 angstroms between the neighboring atoms, about 14 % of the atoms are on the nanoparticle surface. Most of the phenomena in the nanostructures investigated in this thesis are surface-related and occurs on fast time scale. To gain access to these time scales, we make use, throughout this thesis, of time- or frequency-resolved nonlinear optical techniques using, for the time domain, short pulses or broadband long pulses, and for the frequency domain, narrowband long pulses.

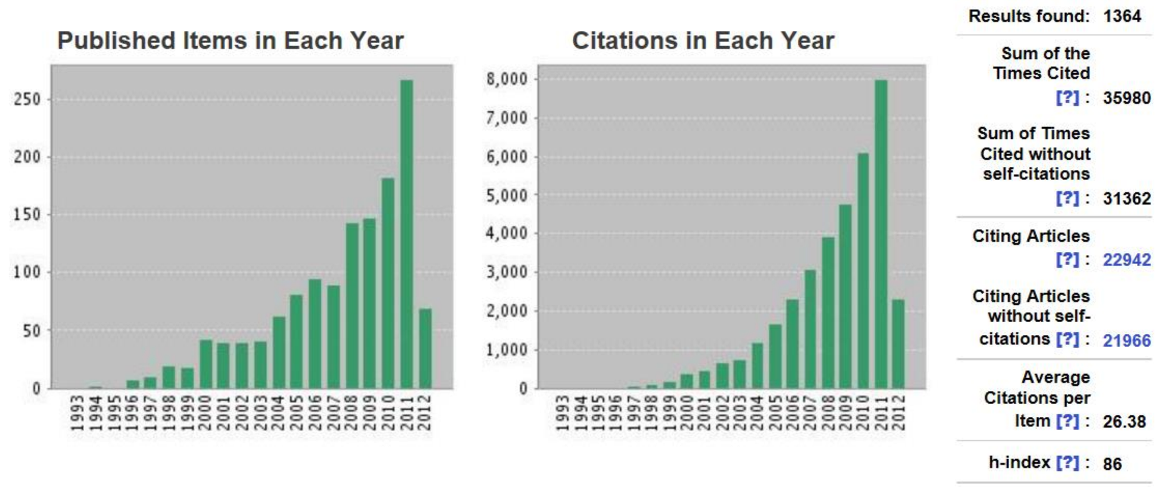

Results found: 1364

Sum of the Times Cited [?] : 35980

Sum of Times Cited without self-citations [?] : 31362

Citing Articles [?] : 22942

Citing Articles without self-citations [?] : 21966

Average Citations per Item [?] : 26.38

h-index [?] : 86

Fig. 1.1 – Web of Science citation report for the terms for the topics {(nanoparticles OR nanocrystals OR nanowires OR nanotubes OR graphene) AND ultrafast} up to April 2012.

In chapter 2, we present an overview of the nonlinear spectroscopic techniques. Emphasis is given to microscopic description through the semiclassical approach for the induced macroscopic polarization in an ensemble of chromophores investigated when the ensemble is subjected to several incoming light fields. The results for this semiclassical description are used to explain the techniques employed in the thesis (pump-probe, photon echoes and spectral hole-burning) and extract the parameters of interest.

Chapter 3 presents experimental results of exciton dephasing in a glass-ceramic containing wide band-gap sodium niobate nanocrystals and discusses the role of trap states for their optical properties. The ultrafast exciton dephasing time is measured via the degenerate four-wave mixing with incoherent light technique, which allows us to determine the dephasing time for an inhomogeneously broadened ensemble with good accuracy. Since for extracting the ultrafast dephasing time we have used broadband non-transform limited long pulses, the chapter also presents the theoretical tools of the coherent spectroscopy with incoherent light and compares that description with the approach presented in chapter 2 for coherent femtosecond pulses. The result for the dephasing time measured is complemented by low-temperature luminescence experiments that show that the presence of trap states on the nanocrystals surface contributes to the phase relaxation of the induced polarization. Also, we show that the host itself contains nonbridging oxygen hole centers that might be responsible for the glass-ceramics' optical properties investigated in the literature so far.

In chapter 4, we measure the localized surface plasmon dephasing time in silver colloidal nanoparticles stabilized with different capping agents. For that purpose, we use the persistent spectral hole-burning technique, which allow us to measure dephasing times faster than 3 fs. The chapter starts with an overview of the optical properties of metallic nanoparticles and discusses the dephasing mechanisms of the localized surface plasmons, which dominate the optical properties of noble metal nanoparticles in the visible region of the electromagnetic spectrum. Then, the technique employed is discussed in detail. The results measured for the dephasing times show that the stabilizers play a major role on the damping of the plasmon resonance in these small sized nanoparticles. The results are correlated to *ab initio* calculation for the interaction among capping agents and the nanoparticles.

In chapter 5, we investigate two different systems using the femtosecond differential absorption technique: 1) Rhodamine 590 linked to amorphous $TiO_2$ nanoparticles: We show that the rhodamine's excited state lifetime is altered due to electron injection from rhodamine into the $TiO_2$ nanoparticles' conduction band; 2) Excited and trap states lifetimes in the glass-ceramic containing $NaNbO_3$ nanocrystals investigated in chapter 1: The trap states' lifetimes in the host present two components, a fast ~ 1 ps and a slow component (longer than the temporal limit of our apparatus) that are responsible for excited state absorption observed in the femtosecond transient absorption signal. This chapter also presents results of the study of the dynamical optical limiting behavior of glass-ceramics containing $NaNbO_3$ nanocrystals. In this case, the dynamics is on the order of hundreds of microseconds and reflects the dynamics of electronic populations in excited levels.

Finally, chapter 6 brings the main conclusions of this work and points to possible solution to the open problems that have arisen during this work.

# 2. Principles of Nonlinear Optical Spectroscopies

This chapter reviews fundamentals of nonlinear optical spectroscopies in order to give the background necessary to understand the physical processes investigated through the techniques employed in this thesis. The approach adopted is discussed in details in Mukamel's book [Mu95]. Another excellent discussion can be found in [Ha11a]. We will see here how nonlinear spectroscopies can extract parameters that are hidden in linear spectroscopies. For that purpose, we will show how nonlinear spectroscopies can be used to control successive light-matter interactions in order to eliminate inhomogeneous broadening, for example, and obtain information about dynamical processes that otherwise would not be possible in ensemble measurements. The induced macroscopic polarization, that gives rise to the measured signals, will be treated pertubatively in the time domain by means of perturbation theory for the density matrix. By careful choice of the parameters (frequency, time ordering, wavevector direction) of the incoming light pulses, we will see how the analysis of the signals generated in nonlinear spectroscopies is somewhat simplified. A diagrammatic approach will be introduced to keep track of the possible pathways that the induced polarization may follow. The diagrams simplify the problem because analytical results can be given and one can select that diagrams that effectively contribute to a given signal and exclude the others. Finally, the theoretical background developed will be used to provide grounds for the main techniques (pump-probe, photon echoes and spectral hole-burning) used in this work.

## 2.1 The nonlinear optical polarization

Our starting point is the macroscopic Maxwell's equations in the absence of free currents and free charges for a non-magnetic homogeneous medium:

$$\nabla \cdot \boldsymbol{D} = 0\,, \tag{2.1}$$

$$\nabla \cdot \boldsymbol{B} = 0\,, \tag{2.2}$$

$$\nabla \times \boldsymbol{E} = -\frac{\partial \boldsymbol{B}}{\partial t}, \tag{2.3}$$

$$\nabla \times \boldsymbol{B} = \mu_0 \frac{\partial \boldsymbol{D}}{\partial t}, \tag{2.4}$$

along with the constitutive relation

$$\boldsymbol{D} = \varepsilon_0 \boldsymbol{E} + \boldsymbol{P}, \tag{2.5}$$

where $\boldsymbol{P}$ is the macroscopic polarization, $\varepsilon_0$ and $\mu_0$ are the electric permittivity and magnetic permeability of free space, respectively.

After taking the curl of eq. (2.3) and some mathematical evaluation, we find

$$\nabla^2 \boldsymbol{E} - \frac{1}{c^2}\frac{\partial^2 \boldsymbol{E}}{\partial t^2} = \mu_0 \frac{\partial^2 \boldsymbol{P}}{\partial t^2}, \tag{2.6}$$

where $c = 1/\sqrt{\mu_0 \varepsilon_0}$ is the speed of light in vacuum. Equation (2.6) is the cornerstone of light-matter interaction and states that the time-varying induced macroscopic polarization acts as a source term for the electromagnetic field. A familiar example of this phenomenon is the fact that accelerated charges emit electromagnetic radiation.

In a ($n$+1)-wave mixing process, the induced macroscopic polarization is a consequence of the interaction of $n$ incoming fields with the medium. The total incident field can be represented as the sum of the $n$ incoming fields considered as traveling plane waves:

$$\boldsymbol{E} = \boldsymbol{E}(\boldsymbol{r},t) = \sum_{j=1}^{n} \left\{ \boldsymbol{E}_j(\boldsymbol{r},t)\exp\left[i\left(\omega_j t - \boldsymbol{k}_j \boldsymbol{r}\right)\right] + \boldsymbol{E}_j^*(\boldsymbol{r},t)\exp\left[-i\left(\omega_j t - \boldsymbol{k}_j \boldsymbol{r}\right)\right]\right\}, \tag{2.7}$$

where $\boldsymbol{k}_j$ and $\omega_j$ are the wavevector and frequency of field $j$, respectively. The induced macroscopic polarization is connected to the total incident field via the optical susceptibility ($\boldsymbol{P} = \chi \boldsymbol{E}$, where $\chi$ is the optical susceptibility), and it can be expanded in power series of the total field:

$$\begin{aligned} \boldsymbol{P} &= \boldsymbol{P}^{(1)} + \boldsymbol{P}_{NL} = \boldsymbol{P}^{(1)} + \boldsymbol{P}^{(2)} + \boldsymbol{P}^{(3)} + \ldots + \boldsymbol{P}^{(n)} \\ &= \chi^{(1)}\boldsymbol{E} + \chi^{(2)}\boldsymbol{E}^2 + \chi^{(3)}\boldsymbol{E}^3 + \ldots + \chi^{(n)}\boldsymbol{E}^n \end{aligned} \tag{2.8}$$

where $\chi^{(1)}$ is the linear susceptibility and $\chi^{(n)}$ ($n$ = 2,3…) is the nth-order susceptibility. As $\boldsymbol{E}$ and $\boldsymbol{P}$ are vectors, the susceptibilities are tensors.

The first nonlinear susceptibility $\chi^{(2)}$, as well as the remaining even-order susceptibilities, vanish for centrosymmetric media. This happens because the electric field and polarization must reverse their signs under space inversion and the even power dependence of $\boldsymbol{P}$ on $\boldsymbol{E}$ does not allow the polarization to reverse its sign. Then, the even-order susceptibilities must be null for centrosymmetric media. However, they are nonzero for noncentrosymmetric media and interfaces. The phenomena related to the second-order polarization are sum- and difference-frequency generation and second harmonic generation, the latter being a particular case of the formers. Techniques based on sum-frequency generation are used, for example, to selectively analyze properties of surfaces and interfaces [Vi05].

The majority of coherent nonlinear spectroscopic techniques are related to the first nonzero term for isotropic media, $\boldsymbol{P}^{(3)}$. Examples are pump-probe transient absorption [Sh86], photon echoes [Ab66, Be84], transient gratings [Ph75], hole-burning [Vö89], coherent Stokes (CSRS) and anti-Stokes Raman scattering (CARS) [Ha87], two-dimensional femtosecond optical spectroscopies [Jo03], birefringence and dichroism [Ip75]. Each technique has it is own features and can be employed by careful selection of the parameters of the incoming pulses.

The macroscopic polarization can be expressed as [Mu95]

$$\boldsymbol{P} = \boldsymbol{P}(\boldsymbol{r},t) = \sum_{n=1}^{\infty}\sum_{s} P_s^{(n)}(t)\exp[i(\omega_s t - \boldsymbol{k}_s \cdot \boldsymbol{r})], \tag{2.9}$$

where the sum over $s$ is performed taking into account all possible combinations of the incident fields. As demanded by momentum and energy conservation, we have

$$\begin{aligned} \boldsymbol{k}_s &= \pm\boldsymbol{k}_1 \pm \boldsymbol{k}_2 \pm \boldsymbol{k}_3 \ldots \pm \boldsymbol{k}_n, \\ \omega_s &= \pm\omega_1 \pm \omega_2 \pm \omega_3 \ldots \pm \omega_n. \end{aligned} \tag{2.10}$$

For example, selecting only one single Fourier component of the third-order macroscopic polarization,

$$\boldsymbol{P}^{(3)}(\boldsymbol{r},t) = P_s(t)\exp[i(\omega_s t - \boldsymbol{k}_s \cdot \boldsymbol{r})], \tag{2.11}$$

the field emitted by the medium will have the form:

$$\boldsymbol{E}_s(\boldsymbol{r},t) = E_s(z,t)\exp[i(\omega_s t - \boldsymbol{k}'_s \cdot \boldsymbol{r})]. \tag{2.12}$$

The vectors $\boldsymbol{k}_s$ and $\boldsymbol{k}'_s$ do not have necessarily the same direction. Nevertheless, in coherent spectroscopies, the direction of $\boldsymbol{k}_s$ is close to the direction of $\boldsymbol{k}'_s$. If the sample of length $l$ is thin but larger than the wavelength of light ($k_s l >> 1$), $\boldsymbol{k}_s$ can be considered propagating along the $z$ axis in eqs. (2.11) and (2.12).

Substituting eqs. (2.11) and (2.12) into eq. (2.6) and taking the temporal envelope of both the polarization and emitted signal to be slow enough compared to the optical cycle (the slowly varying envelope approximation), we may consider $\left|\frac{\partial P_s(t)}{\partial t}\right| << |\omega_s P_s(t)|$ and $\left|\frac{\partial E_s(t)}{\partial t}\right| << |\omega_s E_s(t)|$. Furthermore, assuming that the longitudinal variation is slow enough such that the approximations $\left|\frac{\partial^2 E_s(z)}{\partial z^2}\right| << \left|k_s' \frac{\partial E_s(z)}{\partial z}\right|, \left|k_s'^2 E_s(z)\right|$ are valid, we have

$$\begin{aligned} &2ik_s' \frac{\partial E_s(z,t)}{\partial z} = -\mu_0 \omega_s^2 P_s(t) \exp(-i\Delta\boldsymbol{k}\cdot\boldsymbol{z}), \\ &\Delta\boldsymbol{k} = \boldsymbol{k}_s - \boldsymbol{k}_s'. \end{aligned} \tag{2.13}$$

Then integrating the generated signal along the sample length ($0 < z < l$), we finally obtain, at the end of the sample,

$$E_s(l,t) = \frac{i\mu_0\omega_s^2}{2k'_2} l P_s(t) \operatorname{sinc}\left(\frac{\Delta\boldsymbol{k}\cdot\boldsymbol{l}}{2}\right) \exp\left(i\frac{\Delta\boldsymbol{k}\cdot\boldsymbol{l}}{2}\right), \tag{2.14}$$

where the sinc function is defined as $\operatorname{sinc}(\mathrm{x}) = \frac{\sin(x)}{x}$. The intensity of the emitted signal is given by

$$I_s(t) \propto |E_s(l,t)|^2 = \left(\frac{\mu_0\omega_s^2}{2k'_2} l\right)^2 |P_s(t)|^2 \operatorname{sinc}^2\left(\frac{\Delta\boldsymbol{k}\cdot\boldsymbol{l}}{2}\right). \tag{2.15}$$

Two important features can be observed in the last two equations. The first is that the signal field is proportional to the polarization. However, there is a $\pi/2$ phase shift between them. Another important feature is the behavior of the emitted signal intensity with respect with the phase mismatch between $\boldsymbol{k}_s$ and $\boldsymbol{k}_s'$ due to the sinc function structure. Figure 2.1 shows the plot of the $\operatorname{sinc}^2(x)$ function. Notice that the intensity of the signal is maximum around $\Delta\boldsymbol{k}\cdot\boldsymbol{l} \sim 0$ and falls off rapidly for $\Delta\boldsymbol{k}\cdot\boldsymbol{l}/2 = \pi$. When $k_s l >> 1$ (thin sample), the condition is satisfied for $\Delta\boldsymbol{k} = \boldsymbol{k}_s - \boldsymbol{k}_s' \sim 0$. This is the *phase-matching* condition that is automatically fullfiled in four-wave mixing spectroscopies.

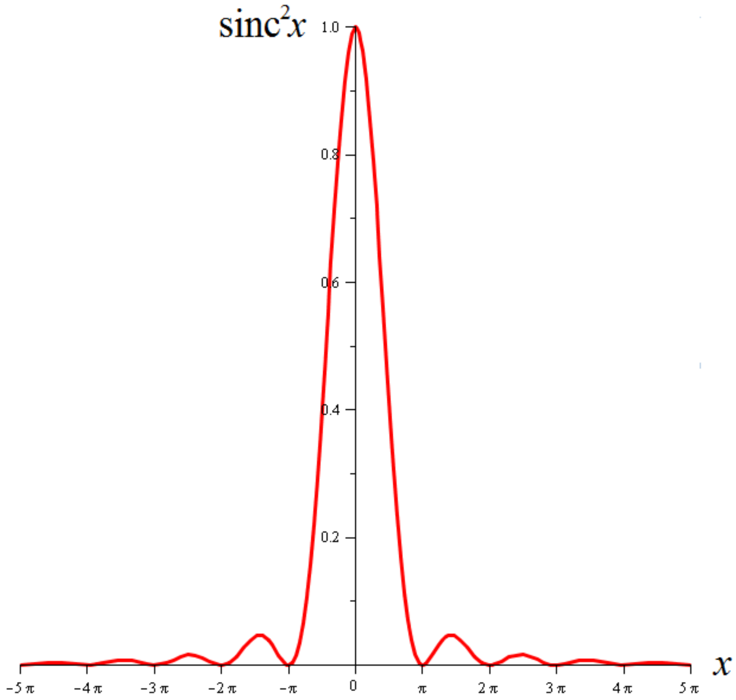

Fig 2.1. Plot of the $\mathrm{sinc}^2(x)$. The nonlinear signal generated is peaked around $x = 0$.

## 2.2 Quantum-mechanical formalism for the nonlinear optical polarization

The macroscopic polarization can be calculated quantum-mechanically through the ensemble average of the dipole moment operator $\mu$:

$$\boldsymbol{P}(t) = N\langle \boldsymbol{\mu}(t)\rangle = NTr[\boldsymbol{\mu}\rho(t)], \tag{2.16}$$

where $\rho$ is the density operator of the ensemble and $N$ is the density of atoms, molecules etc. For simplicity we will assume $N = 1$. For a two-level system, the matrix representation for both the dipole and density operators can be written as

$$\mu = \begin{bmatrix} 0 & \mu_{01} \\ \mu_{10} & 0 \end{bmatrix}, \text{ and } \rho = \begin{bmatrix} \rho_{00} & \rho_{01} \\ \rho_{10} & \rho_{11} \end{bmatrix}. \tag{2.17}$$

Therefore,

$$\boldsymbol{P}(t) = Tr[\boldsymbol{\mu}\rho(t)] = \mu_{01}\rho_{10}(t) + \mu_{10}\rho_{01}(t). \tag{2.18}$$

The induced macroscopic polarization depends on the off-diagonal elements of the density matrix. Therefore, the evolution of them is responsible for the emission of the electromagnetic field. The diagonal terms represent the levels' *populations*, while the off-diagonal are the states' *coherences*. $\rho_{ii}$ is the population of state $\left|i\right\rangle$ and $\rho_{ij}$ is the coherence between states $\left|i\right\rangle$ and $\left|j\right\rangle$.

The dynamics of the macroscopic polarization is governed by the dynamics of the density operator (the Liouville equation):

$$\frac{d}{dt}\rho(t) = -\frac{i}{\hbar}\left[H(t), \rho(t)\right], \tag{2.19}$$

where $2\pi\hbar$ is the Planck constant. It is instructive to find the temporal evolution for each term of the density matrix for a two-level system under interaction with an optical field $\boldsymbol{E}(t)$. The time-dependent Hamiltonian, in the electric dipole approximation, can be written as

$$H(t) = H_0 - \mu E(t). \tag{2.20}$$

where $H_0$ is the unperturbed Hamiltonian and the dipole moment was considered colinear with the electric field, for convenience. In the eigenstate basis of $H_0$,

$$H_0 = \begin{bmatrix} \varepsilon_0 & 0 \\ 0 & \varepsilon_1 \end{bmatrix}, \text{ and } H(t) = \begin{bmatrix} \varepsilon_0 & -\mu E(t) \\ -\mu E(t) & \varepsilon_1 \end{bmatrix}, \tag{2.21}$$

where $\varepsilon_0$ and $\varepsilon_1$ are the eigenenergies of eingenstates $\left|0\right\rangle$ and $\left|1\right\rangle$ respectively, and $\mu_{01} = \mu_{10} = \mu$. Substituting equations (2.21) and (2.17) into (2.19) and evaluating it, we find the following set of coupled differential equations:

$$\frac{d}{dt}\rho_{10}(t) = -i\omega_{10}\rho_{10}(t) + i\frac{\mu}{\hbar}E(t)\left[\rho_{00}(t) - \rho_{11}(t)\right], \tag{2.22}$$

$$\frac{d}{dt}\rho_{11}(t) = -i\frac{\mu}{\hbar}E(t)\left[\rho_{10}(t) - \rho_{10}^{*}(t)\right], \tag{2.23}$$

$$\frac{d}{dt}\left[\rho_{00}(t) - \rho_{11}(t)\right] = 2i\frac{\mu}{\hbar}E(t)\left[\rho_{10}(t) - \rho_{10}^{*}(t)\right]. \tag{2.24}$$

The Hermitian character of the density operator was used in the last two equations ($\rho_{01} = \rho_{10}^{*}$). In the absence of optical perturbation, the density matrix elements evolve as

$$\frac{d}{dt}\rho_{10}(t) = -i\omega_{10}\rho_{10}(t), \tag{2.25a}$$

$$\frac{d}{dt}\left(\rho_{00}(t)-\rho_{11}(t)\right)=0\,. \tag{2.25b}$$

The last two equations state that the difference in the populations of the two levels remains constant in time and the coherences oscillate with frequency $\hbar\omega_{10}=\varepsilon_1-\varepsilon_0$. Then the coherences evolve as $\rho_{10}(t)=\rho_{10}(0)\exp(-i\omega_{10}t)$ in the perturbation-free case.

When the optical field is turned off, it is expected that the phase coherence between the eingenstates is lost, as well as the populations reach their equilibrium value $(\rho_{00}-\rho_{11})_0$ due to interaction with the environment. The phenomenological parameters that accounts for these phase coherence and population decay processes can be added to the equations (2.22) and (2.24):

$$\frac{d}{dt}\rho_{10}(t)=-i\omega_{10}\rho_{10}(t)+i\frac{\mu}{\hbar}E(t)\left[\rho_{00}(t)-\rho_{11}(t)\right]-\frac{\rho_{10}(t)}{T_2}\,, \tag{2.26}$$

$$\frac{d}{dt}(\rho_{00}-\rho_{11})(t)=2i\frac{\mu}{\hbar}E(t)\left[\rho_{10}(t)-\rho_{10}^{*}(t)\right]-\frac{(\rho_{00}-\rho_{11})(t)-(\rho_{00}-\rho_{11})_0}{T_1}\,, \tag{2.27}$$

where $T_1$ is the population relaxation or longitudinal time, while $T_2$ is known as the dephasing or transverse time. These are important parameters investigated in this thesis. Specifically, our goal is to understand the mechanisms responsible for these relaxation times in different nanosystems. They will be discussed in details in the following chapters.

Again, when the external field is turned off, the coherences oscillate but now are damped according to $\rho_{10}(t)=\rho_{10}(0)\exp(-i\omega_{10}t)\exp(-t/T_2)$ (see fig. 2.2). We will mention the form of the off-diagonal density matrix elements evolution when dealing with multiwave mixing spectroscopies.

The density matrix and hence the macroscopic polarization, in the weak-field regime i.e., when the incident fields are much weaker than the inner atomic fields, can be treated perturbatively as

$$\rho(t)=\rho^{(0)}(-\infty)+\sum_{n=1}^{\infty}\rho^{(n)}(t)\,. \tag{2.28}$$

$\rho^{(0)}(-\infty)$ is the density matrix of the ensemble at thermal equilibrium. Then, the nth-order macroscopic polarization will be given by

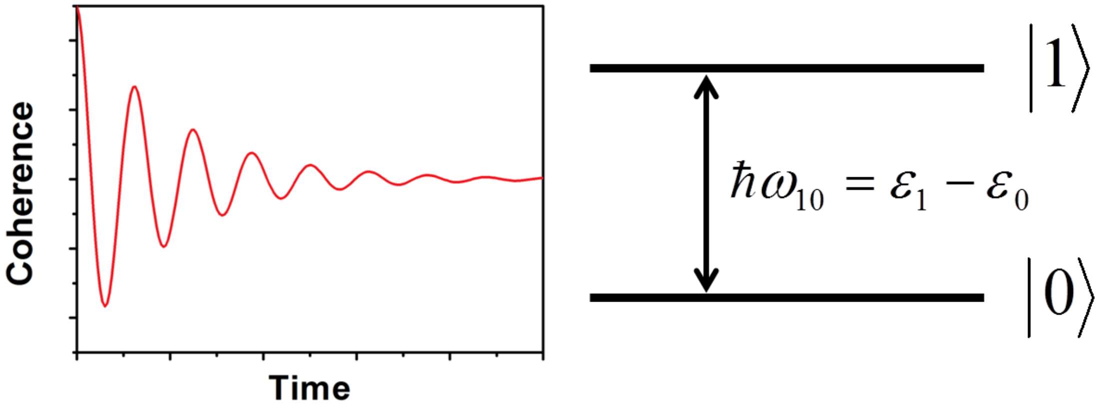

Fig. 2.2 – Temporal evolution (left) of the density matrix off-diagonal elements (coherences) for a two-level system (right). The coherences oscillate at a frequency given by the energy difference between the two-levels and are damped with a characteristic time equal to the dephasing time $T_2$.

$$P^{(n)}(t) = Tr\left[\mu\rho^{(n)}(t)\right]. \tag{2.29}$$

At this point, we simplify our calculations switching from the Schrödinger to the interaction picture. An operator in the interaction picture can be related to itself in the Schrödinger picture by

$$A_I(t) = U_0^{\dagger}(t,t_0)AU_0(t,t_0), \tag{2.30}$$

where the subscript $I$ stands for interaction picture and the temporal evolution operator $U(t,t_0)$ is related to the Hamiltonian in eq. (2.20) via its unperturbed term:

$$U_0(t,t_0) = \exp\left[-\frac{i}{\hbar}H_0(t-t_0)\right]. \tag{2.31}$$

Since the expectation value of an operator is independent of its representation (picture), we can evaluate the polarization representing the density and dipole operators in the interaction picture:

$$P^{(n)}(t) = Tr\left[\mu_I(t)\rho_I{}^{(n)}(t)\right]. \tag{2.32}$$

It can be shown that the temporal evolution of $\rho_I(t)$ is given by

$$\frac{d}{dt}\rho_I(t) = -\frac{i}{\hbar}\left[H'_I(t),\rho_I(t)\right] = \frac{i}{\hbar}\left[\mu_I(t)E(t),\rho_I(t)\right]. \tag{2.33}$$

The solution of eq. (2.33) can be found by integrating both sides:

$$\rho_I(t) = \rho_I(t_0) - \frac{i}{\hbar}\int_{t_0}^{t} dt_1 [H_I'(t_1), \rho_I(t_1)], \tag{2.34}$$

and solving eq. (2.34) iteratively, we obtain

$$\begin{aligned}\rho_I(t) = \rho_I(t_0) + \sum_{n=1}^{\infty}\left(-\frac{i}{\hbar}\right)^n \int_{t_0}^{t} dt_n \int_{t_0}^{t_n} dt_{n-1} \ldots \int_{t_0}^{t_2} dt_1 \\ [H_I'(t_n), [H_I'(t_{n-1}), \ldots [H_I'(t_1), \rho_I(t_0)] \ldots]]\end{aligned}. \tag{2.35}$$

Comparing eq. (2.35) with the series expansion of the density operator (eq. (2.28)), we can write, for the nth-order of the density operator,

$$\rho_I^{(n)}(t) = \left(-\frac{i}{\hbar}\right)^n \int_{t_0}^{t} dt_n \int_{t_0}^{t_n} dt_{n-1} \ldots \int_{t_0}^{t_2} dt_1 [H_I'(t_n), [H_I'(t_{n-1}), \ldots [H_I'(t_1), \rho_I(t_0)] \ldots]]. \tag{2.36}$$

To give a physical interpretation to the last expression, let's look at the commutator for the third-order expansion of the density matrix:

$$\begin{aligned}&\rho_I^{(3)} : \ [H_I'(t_3), [H_I'(t_2), [H_I'(t_1), \rho_I(t_0)]]] = \\ &E(t_3)E(t_2)E(t_1)\left[U_0^\dagger(t_3,t_0)\mu U_0(t_3,t_0), \left[U_0^\dagger(t_2,t_0)\mu U_0(t_2,t_0), \left[U_0^\dagger(t_1,t_0)\mu U_0(t_1,t_0), \rho_I(t_0)\right]\right]\right]\end{aligned}. \tag{2.37}$$

The commutator has eight terms. The first term is

$$\begin{aligned}&U_0^\dagger(t_3,t_0)\mu U_0(t_3,t_0) U_0^\dagger(t_2,t_0)\mu U_0(t_2,t_0) U_0^\dagger(t_1,t_0)\mu U_0(t_1,t_0)\rho_I(t_0) = \\ &U_0^\dagger(t_3,t_0)\mu U_0(t_3,t_2)\mu U_0(t_2,t_1)\mu U_0(t_1,t_0)\rho_I(t_0),\end{aligned} \tag{2.38}$$

where we have used $U_0(t_i,t_0)U_0^\dagger(t_{i-1},t_0) = U_0(t_i,t_0)U_0(t_0,t_{i-1}) = U_0(t_i,t_{i-1})$. This manipulation is represented in fig. 2.3. Starting from $t_0$, the system evolves freely up to $t_1$ under the propagator $U_0(t_1,t_0)$. At $t_1$, the system interacts with the field via the dipole operator $\mu$. After that interaction, the system evolves freely up to $t_2$ under the propagator $U_0(t_2,t_1)$ but interacts again at $t_2$, then evolving freely up to $t_3$ when the third interaction happens. The role of the last interaction will become clear when calculating the macroscopic polarization (eq. 2.32). The analysis for the remaining seven terms of the commutator in eq. (2.37) is straightforward. However, in some of these terms, the interaction can occur either at the left (ket) or right (bra) side of the density matrix.

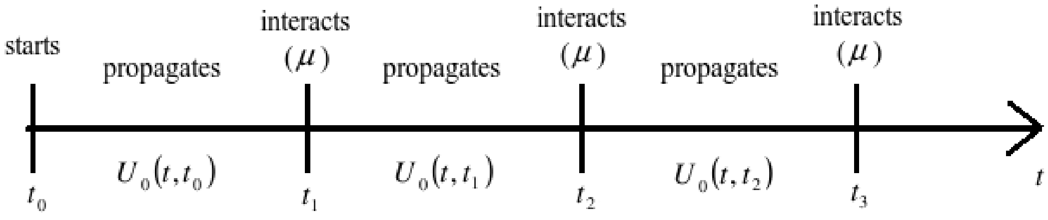

Fig. 2.3 – Representation of the temporal evolution of the density operator under the perturbative limit.

The nth-order polarization is then given by

$$P^{(n)}(t) = Tr\left\{\mu_I(t)\left(-\frac{i}{\hbar}\right)^n \int_{t_0}^{t} dt_n \int_{t_0}^{t_n} dt_{n-1}\ldots\int_{t_0}^{t_2} dt_1 \left[H_I'(t_n),\left[H_I'(t_{n-1}),\ldots\left[H_I'(t_1),\rho_I(t_0)\right]\ldots\right]\right]\right\}. \tag{2.39}$$

If we use a new set of variables (time intervals),

$$\begin{aligned} \tau_1 &= t_2 - t_1, \\ \tau_2 &= t_3 - t_2, \\ &\vdots \\ \tau_n &= t - t_n, \end{aligned} \tag{2.40}$$

arbitrarily choose the first interaction to happen at $t_1 = 0$, enforce time ordering ($t_n > t_{n-1}$) and take $t_0 \rightarrow -\infty$, we can rewrite equation (2.39) as

$$\begin{aligned} P^{(n)}(t) = \left(\frac{i}{\hbar}\right)^n \int_0^\infty d\tau_n \int_0^\infty d\tau_{n-1}\ldots\int_0^\infty d\tau_1 E(t-\tau_n)E(t-\tau_n-\tau_{n-1})\ldots E(t-\tau_n-\ldots-\tau_1) \\ Tr\{\mu_I(\tau_n+\tau_{n-1}+\ldots+\tau_1)[\mu_I(\tau_{n-1}+\tau_{n-2}+\ldots\tau_1),\ldots[\mu_I(0),\rho_I(-\infty)]\ldots]\} \end{aligned} . \tag{2.41}$$

The nth-order polarization is the convolution of *n* electric fields with the nth-order nonlinear response function $R^{(n)}(\tau_n, \tau_{n-1}, \ldots, \tau_1)$:

$$\begin{aligned} P^{(n)}(t) = \int_0^\infty d\tau_n \int_0^\infty d\tau_{n-1}\ldots\int_0^\infty d\tau_1 \\ E(t-\tau_n)E(t-\tau_n-\tau_{n-1})\ldots E(t-\tau_n-\ldots-\tau_1)R^{(n)}(\tau_n,\tau_{n-1},\ldots,\tau_1), \end{aligned} \tag{2.42}$$

where

$$R^{(n)}(\tau_n,\tau_{n-1},\ldots,\tau_1)=\left(\frac{i}{\hbar}\right)^n\theta(\tau_n)\theta(\tau_{n-1})\ldots\theta(\tau_1)$$
$$Tr\{\mu_I(\tau_n+\tau_{n-1}+\ldots+\tau_1)[\mu_I(\tau_{n-1}+\tau_{n-2}+\ldots\tau_1),\ldots[\mu_I(0),\rho_I(-\infty)]\ldots]\}. \tag{2.43}$$

The nonlinear response function is an intrinsic property of the system investigated. The macroscopic polarization is then the result of the interaction between light (through the electric fields) and matter (through the nonlinear response function). In general, the nth-order nonlinear response function has $2^n$ terms and is defined only for positive times due to the principle of causality i.e., the polarization must succeed the action of an electric field. The role of the last interaction in eq. 2.43, which is outside the commutator, is different from the preceding ones. It is responsible, after the trace operation, for the emission of the electric field, while the previous interactions are responsible for creating a non-equilibrium density matrix whose off-diagonal terms emit an electric field after the last interaction. Since the macroscopic polarization and the electric fields are physical observables, they must be real. Hence the nonlinear response function must likewise be real.

The mathematical evaluation of the polarization, in the form of eq. (2.42) can be painful if no other simplifying consideration is made in the experiment, because it can have many terms. Take the example of four-wave mixing spectroscopy, where three fields are mixed to generate a fourth. The total electric field is a sum of 6 terms because we can express each of the three incoming fields as sum of pairs of complex conjugate fields. Since there are three products of fields in the integrand of eq. (2.42), there are $6\text{x}6\text{x}6\text{x}2^3 = 1728$ terms in eq. (2.42). Fortunately, in some cases, we can manage the parameters of an experiment to give only 2 terms. This will become clear along the text.

When the temporal envelope of each interacting electric field *i* may be approximated by a delta function i.e., $E_i(t)=E(t)\delta(t-t_i)$, the nth-order nonlinear polarization is proportional to the respective nonlinear response function:

$$P^{(n)}(t)=E(t_1)E(t_2)\ldots E(t_n)R^{(n)}(\tau_n,\tau_{n-1},\ldots,\tau_1). \tag{2.44}$$

The mathematical evaluation of the signal generated in a nonlinear spectroscopy is much simpler when the temporal envelope of the pulses is much shorter than the relevant spectroscopic time scales of the material. This is called the semi-impulsive limit.

## 2.3 The nonlinear response functions and diagrammatic perturbation theory

As previously stated, the nth-order nonlinear has $2^n$ terms which may contain an action of the dipole operator either at the left (ket) or the right (bra) side of the density operator, each of which is responsible for a different pathway that the non-equilibrium density matrix can follow. For each pathway, we can construct an intuitive diagram for the evolution of the density matrix, which simplifies the problem when dealing with multiple electric fields and system eigenstates. Let's analyze first the simplest case, the linear response function for a two-level system:

### 2.3.1 Linear response function for a two level system

The linear response function for a two-level system is given by

$$R^{(1)}(\tau_1) = \frac{i}{\hbar} Tr\{\mu_I(\tau_1)[\mu_I(0), \rho_I(-\infty)]\} = \frac{i}{\hbar}(R_1 + R_2), \tag{2.45}$$

where we have dropped the Heaviside step functions for convenience and we will do it from now on. The linear response function has two terms which can be found by evaluating the commutator in eq. (2.45)

$$\begin{aligned} R_1 &= Tr\{\mu_I(\tau_1)\mu_I(0)\rho_I(-\infty)\}, \\ R_2 &= -Tr\{\mu_I(\tau_1)\rho_I(-\infty)\mu_I(0)\} = -Tr\{\rho_I(-\infty)\mu_I(0)\mu_I(\tau_1)\} = \\ &\quad - Tr\left\{\rho_I^\dagger(-\infty)\mu_I^\dagger(0)\mu_I^\dagger(\tau_1)\right\} = -Tr\left\{(\mu_I(0)\rho_I(-\infty))^\dagger \mu_I^\dagger(\tau_1)\right\} = \\ &\quad - Tr\{\mu_I(\tau_1)\mu_I(0)\rho_I(-\infty)\}^* = -R_1^*. \end{aligned} \tag{2.46}$$

During the evaluation of $R_2$, we have used the invariance of the trace under cyclic permutation ($Tr\{ABC\}= Tr\{BCA\}$) and the fact that the operators are Hermitian as they represent observables. Therefore, only the first term $R_1$ is necessary to describe the linear response, since $R_2$ is the negative of the complex conjugate of $R_1$. This is general for higher-order response functions and therefore only $2^{n-1}$ independent terms are necessary to describe the nth-order response function. Figure 2.4 shows the double-sided Feynman diagrams that describe the first-order response function. The rules for constructing the diagrams are the following:

1) Draw two vertical lines corresponding to the evolution of the elements of the density matrix $\rho_{ij} = |i\rangle\langle j|$. The left line is the ket, while the right line is the bra side of the density matrix. Time flows from bottom to top;

2) Identify the energy levels involved in the interactions. The density matrix starts in the equilibrium state. If the energy separation between the levels are higher than the energy necessary for a thermal excitation ($\varepsilon_{10} > k_B T$) then the equilibrium state is the ground state $\rho_{00} : |0\rangle\langle 0|$;

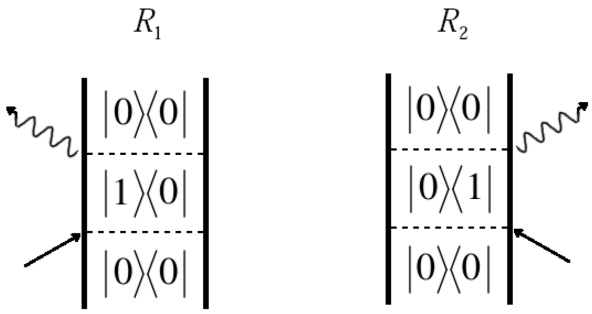

Fig. 2.4 – Double-sided Feynman diagrams for the first-order nonlinear response function. The diagram $R_2$ is the complex conjugate of $R_1$. By convention, it is not necessary to represent $R_2$.

3) An incoming straight arrow, acting either at the left or the right side, represents an excitation (absorption) of the corresponding side of the density matrix due to interaction with an electric field. An outgoing straight arrow represents a deexcitation (stimulated emission) of the corresponding side of the density operator;

4) An arrow pointing to the right (left) represents an interaction with a field $E_i$ ($E_i^*$) with wavevector $+\boldsymbol{k}_i$ ($-\boldsymbol{k}_i$), and contributes with a term $\omega_i$ ($-\omega_i$) for the frequency of the emitted field;

5) The sign of the diagram is given by $(-1)^n$, where $n$ is the number of interactions from the right (bra) side, since when evaluating the commutator, each interaction at the right side carries a minus sign;

6) Between consecutive interactions, the system evolves freely under the system free Hamiltonian $H_0$;

7) The last interaction, represented by a wavy arrow, is an emission. By convention, it is chosen to happen at the left side. The final state must be a population state.

We can construct an analytic form for the linear polarization of an electronic two-level system analyzing the term $R_1$. Before $t = 0$, the density matrix is its equilibrium state, namely the ground state $\rho_{00} = p_0$, where $p_0$ is the probability of finding the system in the ground state. From now on we will assume $p_0 = 1$. At $t = 0$, a field interacts with the system and creates a coherence $\rho_{10}$, proportional to the dipole operator $\mu_{10}$. As we have seen before, this coherence evolves freely in time under the Hamiltonian $H_0$ according to

$\rho_{10}(t)=\rho_{10}(0)\exp(-i\omega_{10}t)\exp(-\Gamma_{10}t)$, where $\Gamma_{10}=1/T_2$. At $t=\tau_1$, the dipole operator $\mu_{10}$ returns the system to the ground state $\rho_{00}$ and an electric field is emitted. Thus,

$$R_1=\rho_{00}\times\mu_{10}\times\exp(-i\omega_{10}\tau_1-\Gamma_{10}\tau_1)\times\mu_{10}=|\mu_{10}|^2\exp(-i\omega_{10}\tau_1-\Gamma_{10}\tau_1). \tag{2.47}$$

The linear polarization is then given by

$$P^{(1)}(t)=\frac{i}{\hbar}\int_0^\infty d\tau_1 E(t-\tau_1)\left[|\mu_{10}|^2\exp(-i\omega_{10}\tau_1-\Gamma_{10}\tau_1)-|\mu_{10}|^2\exp(i\omega_{10}\tau_1-\Gamma_{10}\tau_1)\right]. \tag{2.48}$$

Assuming that the field has the following form:

$$E(t)=2|E_0(t)|\cos(\omega t-\boldsymbol{k}\cdot\boldsymbol{r})=|E_0(t)|\cdot[\exp(-i\omega t+i\boldsymbol{k}\cdot\boldsymbol{r})+\exp(i\omega t-i\boldsymbol{k}\cdot\boldsymbol{r})], \tag{2.49}$$

we obtain

$$\begin{aligned}P^{(1)}(t)=\frac{i}{\hbar}\int_0^\infty d\tau_1|\mu_{10}|^2|E(t-\tau_1)|\exp(-\Gamma_{10}\tau_1)\{&\exp[-i\omega t-i(\omega_{10}-\omega)\tau_1+i\boldsymbol{k}\cdot\boldsymbol{r}]\\ &-\exp[-i\omega t+i(\omega_{10}+\omega)\tau_1+i\boldsymbol{k}\cdot\boldsymbol{r}]+\exp[+i\omega t-i(\omega_{10}+\omega)\tau_1-i\boldsymbol{k}\cdot\boldsymbol{r}]\\ &-\exp[+i\omega t+i(\omega_{10}-\omega)\tau_1-i\boldsymbol{k}\cdot\boldsymbol{r}]\}.\end{aligned} \tag{2.50}$$

For resonant excitation ($\omega_{10}-\omega=0$), the second and third terms that contain factors $\exp(\pm 2i\omega\tau_1)$ are highly oscillatory and average to zero after integration. Only the resonant terms contribute to the integral. This is known as the Rotating Wave Approximation (RWA). The macroscopic polarization for resonant excitation is thus given by

$$P^{(1)}(t)=\frac{i|\mu_{10}|^2}{\hbar}\exp(-i\omega t+i\boldsymbol{k}\cdot\boldsymbol{r})\int_0^\infty d\tau_1|E(t-\tau_1)|\exp(-\Gamma_{10}\tau_1)+c.c., \tag{2.51}$$

where *c.c.* stands for complex conjugate. The terms that do not survive under the RWA approximation correspond to deexcitation of a side of the density matrix that is not excited. This has no physical meaning and thus gives zero contribution to the signal, as we depicted in Fig. 2.5. The RWA approximation simplifies somewhat the analysis of higher-order nonlinear response functions. Under this approximation and the fact that only $2^{n-1}$ terms of the nth-order response function are independent, the number of terms for the third order polarization in eq. (2.42) decreases from 6x6x6x$2^3$ = 1728 to 3x3x3x$2^2$ = 108. Moreover, if the fields are in the

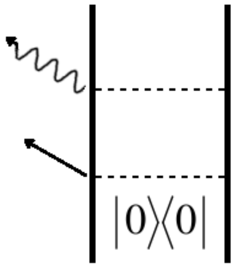

Fig. 2.5 – Example of a double-sided Feynman diagram that does not survive under the RWA approximation.

semi-impulsive limit and we manage the experiments to enforce temporal ordering of the incident fields such that the total electric field at the moment of interaction is composed by only one field, the number of terms decreases from 3x3x3x$2^2$ = 108 to 1x1x1x$2^2$ = 4. We will show in the next sections how the geometry of the experiment can further decrease that number.

### 2.3.2 Third-order response function for a two level system

Since the second-order nonlinear response function is zero for isotropic media, the third-order response function is the most relevant one in nonlinear optical spectroscopies. It has $2^3$ = 8 terms, but only 4 terms are independent (the remaining 4 terms are complex conjugates of these). Explicitly, for a two-level system, the third-order response function is given by

$$R^{(3)}(\tau_3,\tau_2,\tau_1)=\left(\frac{i}{\hbar}\right)^3 Tr\{\mu_I(\tau_3),[\mu_I(\tau_2),[\mu_I(\tau_1),[\mu_I(0),\rho_I(-\infty)]]]\}=\left(\frac{i}{\hbar}\right)^3\sum_{j=1}^{4}\left(R_i-R_i^*\right), \tag{2.52}$$

where

$$\begin{aligned} R_1 &= Tr\{\mu_I(\tau_3)\mu_I(\tau_2)\mu_I(\tau_1)\mu_I(0)\rho_I(-\infty)\} \\ R_2 &= Tr\{\mu_I(\tau_3)\mu_I(0)\rho_I(-\infty)\mu_I(\tau_1)\mu_I(\tau_2)\} \\ R_3 &= Tr\{\mu_I(\tau_3)\mu_I(\tau_1)\rho_I(-\infty)\mu_I(0)\mu_I(\tau_2)\}. \\ R_4 &= Tr\{\mu_I(\tau_3)\mu_I(\tau_2)\rho_I(-\infty)\mu_I(0)\mu_I(\tau_1)\} \end{aligned} \tag{2.53}$$

The corresponding double-sided Feynman diagrams are depicted in Fig. 2.6. To give a physical interpretation to each of the four terms in Eq. (2.53), it is useful to express them explicitly.

$$\begin{aligned} R_1 &= \mu_{10}\mu_{10}\exp(-i\omega_{10}\tau_3-\Gamma_{10}\tau_3)\mu_{10}\exp(-\Gamma_{00}\tau_2)\mu_{10}\exp(-i\omega_{10}\tau_1-\Gamma_{10}\tau_1)= \\ &|\mu_{10}|^4\exp\{-i\omega_{10}(\tau_1+\tau_3)-\Gamma_{10}(\tau_1+\tau_3)-\Gamma_{00}\tau_2\} \end{aligned}, \qquad (2.54)$$

$$\begin{aligned} R_2 &= \mu_{10}\mu_{01}^{*}\exp(-i\omega_{10}\tau_3-\Gamma_{10}\tau_3)\mu_{01}^{*}\exp(-\Gamma_{11}\tau_2)\mu_{10}\exp(-i\omega_{10}\tau_1-\Gamma_{10}\tau_1)= \\ &|\mu_{10}|^4\exp\{-i\omega_{10}(\tau_1+\tau_3)-\Gamma_{10}(\tau_1+\tau_3)-\Gamma_{11}\tau_2\} \end{aligned}, \qquad (2.55)$$

$$\begin{aligned} R_3 &= \mu_{10}\mu_{01}^{*}\exp(-i\omega_{10}\tau_3-\Gamma_{10}\tau_3)\mu_{10}\exp(-\Gamma_{11}\tau_2)\mu_{01}^{*}\exp(-i\omega_{01}\tau_1-\Gamma_{01}\tau_1)= \\ &|\mu_{10}|^4\exp\{-i\omega_{10}(-\tau_1+\tau_3)-\Gamma_{10}(\tau_1+\tau_3)-\Gamma_{11}\tau_2\} \end{aligned}, \qquad (2.56)$$

$$\begin{aligned} R_4 &= \mu_{10}\mu_{10}\exp(-i\omega_{10}\tau_3-\Gamma_{10}\tau_3)\mu_{01}^{*}\exp(-\Gamma_{00}\tau_2)\mu_{01}^{*}\exp(-i\omega_{01}\tau_1-\Gamma_{01}\tau_1)= \\ &|\mu_{10}|^4\exp\{-i\omega_{10}(-\tau_1+\tau_3)-\Gamma_{10}(\tau_1+\tau_3)-\Gamma_{00}\tau_2\} \end{aligned}. \qquad (2.57)$$

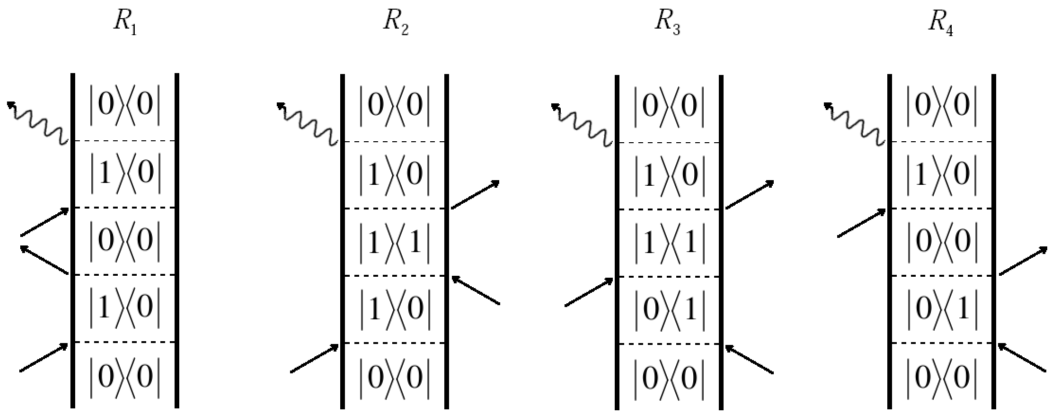

Fig. 2.6 – Double-sided Feynman diagrams for the third-order nonlinear response function.

These four terms give rise to signals with different features in a four-wave mixing experiment. Terms $R_1$ and $R_4$ evolve during $\tau_2$ in the same population state (the ground state $\rho_{00}$), while terms $R_2$ and $R_3$ evolve during $\tau_2$ in the excited state $\rho_{11}$. Another important aspect is the evolution during $\tau_1$ and $\tau_3$, where the system is in a coherence state. $R_1$ and $R_2$ evolve in the same coherences $\rho_{10}$ during $\tau_1$ and $\tau_3$, while $R_3$ and $R_4$ evolve in different coherences during $\tau_1$ and $\tau_3$. For this reason, $R_1$ and $R_2$ are called *nonrephasing* terms while $R_3$ and $R_4$ are called the *rephasing* terms. As we shall see, the rephasing terms give rise to an echo signal that eliminates the inhomogeneous broadening contribution to the spectral linewidth in photon echo experiments.

The features of each term of the third-order nonlinear response are summarized in table 2.1. If the incoming fields have different wavevectors and frequencies, the signals will be generated along different directions and with different frequencies. This is particularly useful to distinguish contributions to the third-order polarization. The following section will be devoted how one can manage each term in nonlinear spectroscopies to extract different spectroscopic parameters.

| Term | Wavevector | Frequency | State during $\tau_1$ | State during $\tau_2$ | State during $\tau_3$ |
|---|---|---|---|---|---|
| $R_1$ (Nonrephasing) | $\boldsymbol{k}_1-\boldsymbol{k}_2+\boldsymbol{k}_3$ | $\omega_1-\omega_2+\omega_3$ | $\|1\rangle\langle 0\|$ | $\|0\rangle\langle 0\|$ | $\|1\rangle\langle 0\|$ |
| $R_2$ (Nonrephasing) | $\boldsymbol{k}_1-\boldsymbol{k}_2+\boldsymbol{k}_3$ | $\omega_1-\omega_2+\omega_3$ | $\|1\rangle\langle 0\|$ | $\|1\rangle\langle 1\|$ | $\|1\rangle\langle 0\|$ |
| $R_3$ (Rephasing) | $-\boldsymbol{k}_1+\boldsymbol{k}_2+\boldsymbol{k}_3$ | $-\omega_1+\omega_2+\omega_3$ | $\|0\rangle\langle 1\|$ | $\|1\rangle\langle 1\|$ | $\|1\rangle\langle 0\|$ |
| $R_4$ (Rephasing) | $-\boldsymbol{k}_1+\boldsymbol{k}_2+\boldsymbol{k}_3$ | $-\omega_1+\omega_2+\omega_3$ | $\|0\rangle\langle 1\|$ | $\|0\rangle\langle 0\|$ | $\|1\rangle\langle 0\|$ |

Table 2.1 – Features of the terms of the third-order response function.

## 2.4 Coherent nonlinear optical spectroscopies

In this section, we will give an overview of selected coherent nonlinear spectroscopies, where we will make use of the previously developed formalism for the nonlinear response function. The description presented in this section will be useful to understand the results of the experiments performed throughout this thesis.

### 2.4.1 Linear absorption

The simplest case of coherent spectroscopy is the linear absorption. In a linear absorption experiment (fig. 2.7), one looks for the changes in the intensity of the incoming light beam due to interaction with matter. The dipoles of the sample are excited by the beam giving rise to a macroscopic polarization (first-order polarization), which is responsible for emitting a field, with a π/2 phase shift with respect to the incoming field (cf. eq. (2.13)), along the direction of the propagation of the incoming field. This is the *free-induction* decay. The first-order polarization is given by eq. (2.51) and the corresponding double-sided Feynman diagrams are depicted in Fig. 2.4. In the semi-impulsive limit, $E(t)=E_0\delta(t)$ and the first-order polarization is given by

$$P^{(1)}(t)=\frac{i|\mu_{10}|^2}{\hbar}E_0\exp(-i\omega t+i\boldsymbol{k}\cdot\boldsymbol{r})\exp(-\Gamma_{10}t)+c.c.. \tag{2.58}$$

The detection of the signal is another important aspect of coherent spectroscopies. Usually, the detection is performed with slow detectors, i.e., the detector risetime is slower than the pulses duration, such that the detector integrates the intensity of the field over the whole time. In linear absorption, the radiated signal and the incoming field are present at the detector at the same time. The signal detected will be

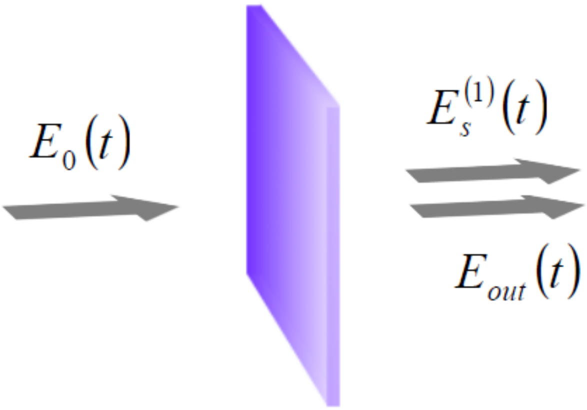

Fig. 2.7 – Representation of the linear absorption experiment. The signal and incoming fields are collinear.

$$I \propto \int_0^\infty \left|E_{out}(t) + E_s^{(1)}(t)\right|^2 dt = \int_0^\infty \left\{\left|E_{out}(t)\right|^2 + \left|E_s^{(1)}(t)\right|^2 + 2\,\mathrm{Re}\left[E_{out}(t)E_s^{(1)}(t)\right]\right\} dt\,. \qquad (2.59)$$

This kind of detection, in which the signal is superimposed to another field, is called *heterodyne detection*. In the present case, the radiated signal interferes with the part of the incoming field that is not absorbed and/or reflected by the sample. The field that is superimposed to the signal is called *local oscillator* (LO). It is possible to design experiments in such a way that the LO can be a field different from the excitation field. In this case, the phase difference between LO and the radiated signal can be controlled. If the signal is detected alone, i.e. without LO, the detection is called *homodyne detection*[1]. This is the case of the photon echo experiments that we will present in the following two sections. Heterodyne detection can be advantageous if the radiated signal is weak, because the integrated intensity will be linear rather than quadratic with the (weak) field.

---

[1] In fact, homodyne and heterodyne detection both use LO. In radio technology, the difference between them is that the LO is frequency-shifted in heterodyne detection. For some unknown reason, the nomenclature has been used in a confusing way by spectroscopists.

In linear absorption, one may be interested in measuring the spectrum of the signal and therefore, the total field $E_{out}(t)+E_s^{(1)}(t)$ is Fourier transformed by a spectrometer. The detected intensity will be

$$I(\omega)\propto\left|E_{out}(\omega)+E_s^{(1)}(\omega)\right|^2=\left|E_{out}(\omega)\right|^2+\left|E_s^{(1)}(\omega)\right|^2+2\,\mathrm{Re}\left[E_{out}(\omega)E_s^{(1)}(\omega)\right]\qquad(2.60)$$

In general, one is interested in the absorbance $A(\omega)=-\log\left(I(\omega)/I_0(\omega)\right)$ (or optical density), where $I_0(\omega)\propto\left|E_0(\omega)\right|^2$ is the transmitted intensity without the sample (the *blank*), such that the

eq. (2.60) needs to be normalized,

$$\frac{I(\omega)}{I_0(\omega)}=\frac{\left|E_{out}(\omega)+E_s^{(1)}(\omega)\right|^2}{\left|E_0(\omega)\right|^2}\,.\qquad(2.61)$$

We will assume that the incident field is only slightly absorbed by the sample, such that we can set $\left|E_{out}(\omega)\right|\approx\left|E_0(\omega)\right|$ and therefore the signal is small compared to the incoming field ($\left|E_s^{(1)}(\omega)\right|<<\left|E_0(\omega)\right|$). The absorbance is then given by

$$A(\omega)\propto-\frac{2\,\mathrm{Re}\left[E_{out}(\omega)E_s^{(1)}(\omega)\right]}{\left|E_0(\omega)\right|^2}\,.\qquad(2.62)$$

Since we have assumed the semi-impulsive limit for the temporal envelope of the incoming pulse, its Fourier transform implies that the incident field is constant in frequency. So we can consider

$$A(\omega)\propto-2\,\mathrm{Re}\left[E_s^{(1)}(\omega)\right]\propto 2\,\mathrm{Im}\left[P^{(1)}(\omega)\right],\qquad(2.63)$$

where we have used the relation between the signal and the induced polarization given by eq. (2.14). Evaluating eq. (2.63) we find,

$$\begin{aligned}A(\omega)&\propto 2\,\mathrm{Im}\left[P^{(1)}(\omega)\right]\propto 2\,\mathrm{Re}\left\{\int_0^\infty\exp\left[-i(\omega-\omega_0)t\right]\exp\left[-\Gamma_{10}t\right]dt\right\}\\&=2\,\mathrm{Re}\left\{\frac{1}{i(\omega-\omega_0)+\Gamma_{10}}\right\}=\frac{2\Gamma_{10}}{(\omega-\omega_0)^2+(\Gamma_{10})^2}\end{aligned}\;.\qquad(2.64)$$

The absorption spectrum is a Lorentzian curve whose the full-width at half maximum (FWHM) is given by the damping parameter $\Gamma_{10} = 1/T_2$ , where $T_2$ is the phase relaxation time.

### 2.4.2 Pump and probe

Perhaps the most widely used third-order nonlinear spectroscopy is the pump-and-probe technique (Fig. 2.8). In this setup, a strong pump beam prepares the system into a non-equilibrium state while a second (weak) beam probes the time evolution of the non-equilibrium state through changes on the probe intensity or polarization. The results are, in general, easy to interpret. Femtosecond transient absorption/stimulated emission [Sh86], pump and probe quantum beats [Jo97], birefrigence and dichroism [Ip75], and absorption anisotropy [Jo96] are third-order spectroscopies that belong to the class of pump and probe experiments. In this thesis, we are interested in femtosecond transient absorption. In this case, the probe and pump beam are ultrashort, the time delay between them can be controlled experimentally and the changes in the intensity (or the spectrum) of the probe due to the presence of the pump are monitored. Since in transient absorption the pump beam precedes the probe, the system interacts twice with the pump and once with the probe. The signal is radiated along the probe direction ($\boldsymbol{k}_{sig} = \pm\boldsymbol{k}_{pump} \mp \boldsymbol{k}_{pump} + \boldsymbol{k}_{probe} = \boldsymbol{k}_{probe}$) and, as in linear absorption spectroscopy, the detection is heterodyne, with the probe pulse acting as the local oscillator. All double-sided Feynman diagrams for the third-order response function contribute to signal (Fig. 2.9). In the

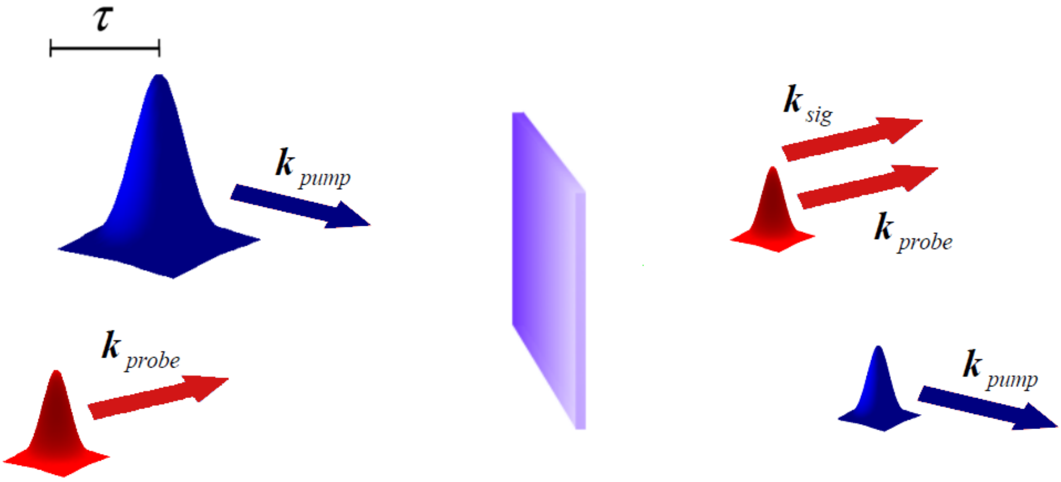

Fig. 2.8 – Scheme of a pump-probe experiment. The signal and probe fields are collinear.

semi-impulsive limit the third order polarization is proportional to the third-order response function:

$$
\begin{aligned}
P^{(3)}(t) = \left|E_{probe}\right|\left|E_{pump}\right|^{2} R^{(3)}(t, \tau_2, \tau_1 = 0) = \\
\left(\frac{i}{\hbar}\right)^{3} \left|E_{probe}\right|\left|E_{pump}\right|^{2} \sum_{j=1}^{4} \left\{R_i(t, \tau_2, \tau_1 = 0) - R_i^{*}(t, \tau_2, \tau_1 = 0)\right\}
\end{aligned}
\qquad (2.65)
$$

The first two pump interactions happen at the same time, hence the first time interval is null ($\tau_1 = 0$) and the first two interactions drive the system into a population state. Therefore, femtosecond transient absorption measures population relaxation times.

Since all four terms in eqs. (2.54) – (2.57) contribute to the radiated signal, it contains different damping parameters ($\Gamma_{00}$ and $\Gamma_{11}$), i.e. populations times, for the excited and ground state. If these times are different due to the presence of a third level for example, the signal profile will be multiexponencial. The time-integrated heterodyned signal is given by

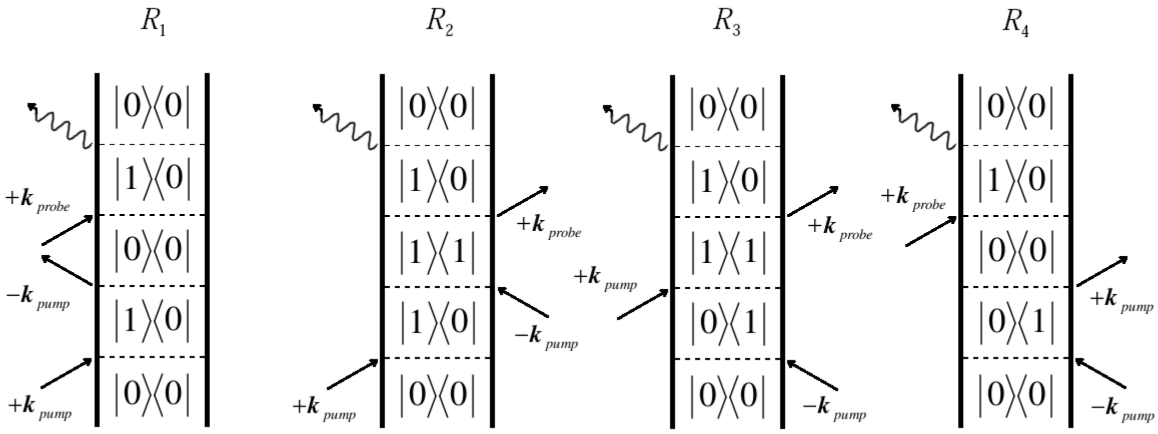

Fig. 2.9 – Double-sided Feynman diagrams for a third order nonlinear pump and probe experiment. The first two interactions come from the pump beam.

$$
I \propto \int_{0}^{\infty} \left|E'_{probe}(t) + E_s^{(3)}(t)\right|^{2} dt . \qquad (2.66)
$$

In general, the measured signal is the difference signal i.e., the signal with and without the presence of the pump beam:

$$\Delta I \propto \int_0^\infty \left| E'_{probe}(t) + E_s^{(3)}(t) \right|^2 dt - \int_0^\infty \left| E'_{probe}(t) \right|^2 dt = \\ \int_0^\infty \left\{ 2\,\mathrm{Re}\left[ E'_{probe}(t) E_s^{(3)}(t) \right] + \left| E_s^{(3)}(t) \right|^2 \right\} dt \sim 2\,\mathrm{Re} \int_0^\infty \left\{ E'_{probe}(t) E_s^{(3)}(t) \right\} dt \quad , \qquad (2.67)$$

where we have assumed that the intensity of the radiated signal is much weaker than the intensity of the probe beam ( $\left| E_s^{(3)}(t) \right| << \left| E'_{probe}(t) \right|$ ). The signal field has a π/2 phase shift with respect to the third-order polarization, and therefore, the detected signal in the pump-probe femtosecond differential absorption is given by:

$$\Delta I \propto \mathrm{Im} \int_0^\infty \left\{ E'_{probe}(t) P^{(3)}(t) \right\} dt \, . \qquad (2.68)$$

The third-order polarization contains a product involving two modula of the pump electric fields and one of the probe. Since there is another product involving modulus of electric field in the integrand of eq. (2.68), the measured pump-probe signal is linear with respect to the intensities of both pump and probe beams.

Since the signal is heterodyne detected, the intensity measured contains factors of the type $\exp(-\Gamma_{ii}\tau_2)$. The population lifetimes are extracted directly by fitting exponential curves and the multiple time constants in multiexponencial analysis correspond to different dynamics of population relaxation.

### 2.4.3 Two-pulse photon echo

Linear absorption spectroscopy measures the total absorption lineshape of an ensemble (fig 2.10). However, information about the absorption linewidth of a single absorbing entity (homogeneously broadened), which can be, for example, an atom, molecule or nanoparticle, is lost when the entities in an ensemble have different static transition frequencies (inhomogeneous broadening). Pump and probe transient absorption experiments measure population relaxation times. However, the coherence relaxation, and hence the homogeneous linewidth $\Gamma_{\mathrm{hom}}$, cannot be measured in this configuration. A beautiful time domain approach for measuring the dephasing times when inhomogeneous broadening is present are the photon echo experiments, in which the influence of inhomogeneous broadening can be completely eliminated.

The configuration for the two-pulse photon echo technique [Be88] is depicted in fig. 2.11. For

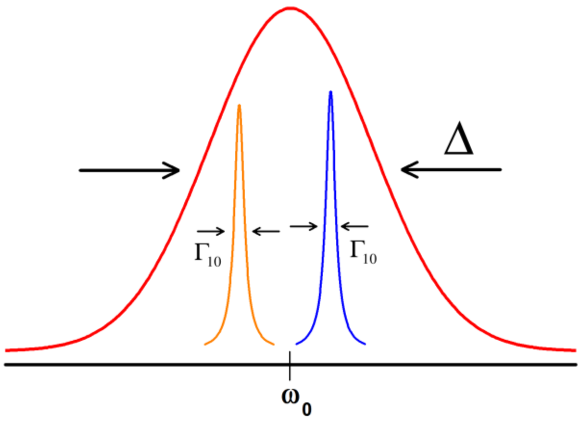

Fig. 2.10 – Representation of a linear absorption spectrum of a inhomogeneously broadened ensemble. $\Delta$ is the inhomogeneous linewidth whereas $\Gamma_{10}$ is the homogeneous linewidth of an element of the ensemble.

convenience, we will assume the semi-impulsive limit. Two pulses with wavevectors $\boldsymbol{k}_1$ and $\boldsymbol{k}_2$, respectively, propagating along different directions are crossed in the sample. The temporal delay between them can be experimentally controlled. The background-free signal in the phase-matched direction $\boldsymbol{k}_3 = 2\boldsymbol{k}_2 - \boldsymbol{k}_1$ will be detected directly (homodyne detection). In that direction, only the rephasing diagrams $R_3$ and $R_4$ contribute to the signal. The last two interactions are due to the $\boldsymbol{k}_2$ pulse and, as we are assuming the semi-impulsive limit, the last two interactions happen at the same time. Thus the $R_3$ and $R_4$ contributions, that evolve in different population states between the last two interactions, contribute equally to the nonlinear response (Fig. 2.12). We shall assume that the pulses are degenerate, i.e., they have the same carrier frequency ($\omega_1 = \omega_2 = \omega$).

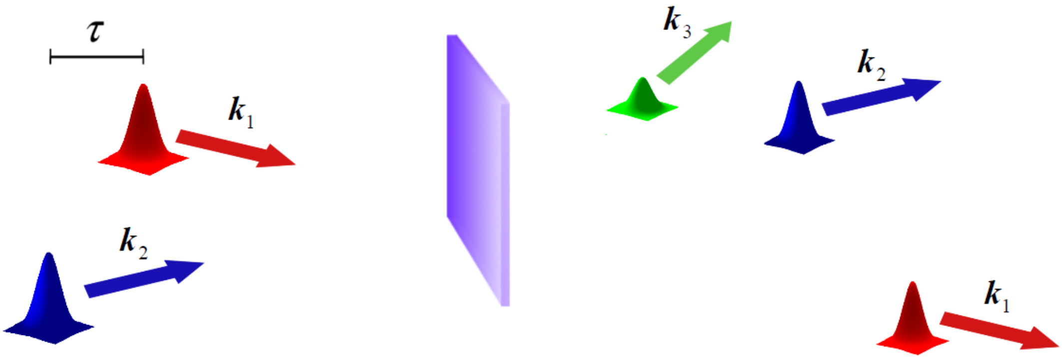

Fig. 2.11 – Scheme of the two-pulse photon echo technique. The signal is emitted along the $\boldsymbol{k}_3 = 2\boldsymbol{k}_2 - \boldsymbol{k}_1$ direction.

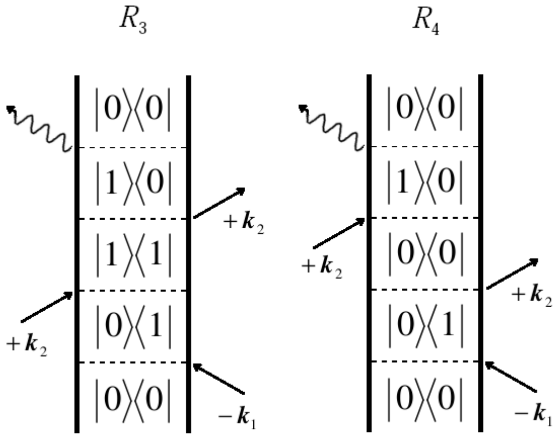

Fig. 2.12 – Double-sided Feynman diagrams for the two-pulse photon echo technique.

For an inhomogeneously broadened system, the nonlinear response function must be averaged over the inhomogeneous distribution

$$S_3' = \int d\omega_{10} g\left(\omega_{10} - \omega_{10}^{(0)}\right) S_3 , \tag{2.69}$$

where $\omega_{10}^{(0)}$ is the center frequency of the transition and $g\left(\omega_{10} - \omega_{10}^{(0)}\right)$ is the inhomogeneous lineshape. Assuming a Gaussian function for the inhomogenous lineshape, we have

$$g\left(\omega_{10} - \omega_{10}^{(0)}\right) = \frac{1}{\Delta\sqrt{2\pi}} \exp\left[ -\frac{\left(\omega_{10} - \omega_{10}^{(0)}\right)^2}{2\Delta^2} \right]. \tag{2.70}$$

Since a convolution in the frequency domain is a product in the time domain and taking the Fourier transform of (eq. 2.70), where the time variable is $(\tau_3 - \tau_1)$ as it appears multiplying the transition frequency $\omega_{10}$ in eq. (2.56), the macroscopic polarization along $2\boldsymbol{k}_2 - \boldsymbol{k}_1$ is, in the semi-impulsive limit, given by

$$P^{(3)}(\tau_3, \tau_1) \propto \exp\left[-i\omega_{10}^{(0)}(\tau_3 - \tau_1)\right] \times \exp\left[-\Gamma_{10}(\tau_1 + \tau_3)\right] \times \exp\left[ -\frac{\Delta^2 (\tau_3 - \tau_1)^2}{2} \right]. \tag{2.71}$$

For an extremely inhomogeneously broadened distribution ($\Delta >> \Gamma_{10}$), the factor $\exp\left[-\Delta^2(\tau_3 - \tau_1)^2/2\right] \sim \delta(\tau_3 - \tau_1)$, and the polarization is sharply peaked at $\tau_3 = \tau_1$. The situation is depicted in fig. 2.13. The first pulse creates a coherence between excited and ground state. During time $\tau_1$, the excited dipoles within the inhomogeneous distribution oscillate with different frequencies and phases depending on the detuning with respect to $\omega_{10}^{(0)}$. The induced macroscopic polarization is being lost due to dephasing of the excited dipoles and damped due to the homogeneous broadening. The second pulse drives the system into a population state (can be either excited or ground state) from where it is sent back again in a coherence state, due to the instantaneous action of the third field (pulse), now in a conjugated coherence with respect to the first excitation. Hence the phase of oscillation of the inhomogenous distribution is reversed with respect to the first evolution period. At $\tau_3 = \tau_1$, the oscillating dipoles rephase again and the system recovers its macroscopic polarization, emitting coherently an echo field along the $2\boldsymbol{k}_2 - \boldsymbol{k}_1$ direction.

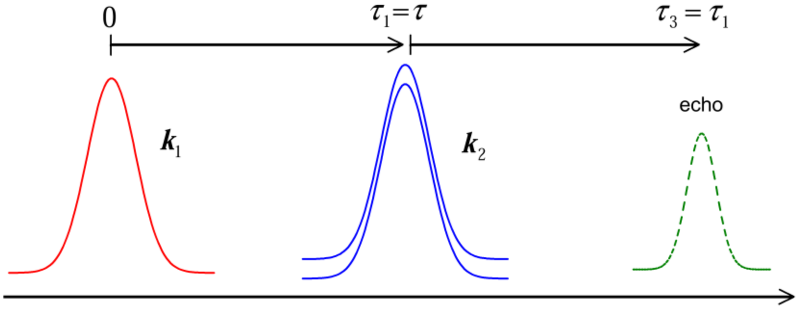

Fig. 2.13 – Pulse sequence in two-pulse photon echo. At $\tau_3 = \tau_1$, the inhomogeneously broadened dipoles rephase and an echo signal is emitted.

The detected signal will be

$$I(\tau) \propto \int_0^\infty d\tau_3 |P(\tau_3, \tau)|^2 \propto \int_0^\infty d\tau_3 |\exp[-\Gamma_{10}(\tau + \tau_3)] \times \delta(\tau_3 - \tau)|^2 = \exp(-4\Gamma_{10}\tau), \qquad (2.72)$$

where $\tau = \tau_1$ is the control parameter of the experiment i.e., the interval between pulses $\boldsymbol{k}_1$ and $\boldsymbol{k}_2$. In the inhomogeneously broadening limit, the signal profile decays with time constant equal to $4\Gamma_{10}$.

If the system is homogeneously broadened, Δ = 0 and the integrated detected signal will be

$$I(\tau) \propto \int_0^\infty d\tau_3 |P(\tau_3, \tau)|^2 \propto \int_0^\infty d\tau_3 |\exp\{-\Gamma_{10}(\tau + \tau_3)\}|^2 \propto \exp(-2\Gamma_{10}\tau). \qquad (2.73)$$

The signal profile decays with twice the homogeneous width in the homogeneous broadening limit. In both cases, the inhomogeneous broadening is removed and one obtains the homogeneous linewidth.

In the intermediate case, both homogeneous and inhomogeneous broadening factors in eq. (2.71) contribute to the signal. The integrated signal will be

$$\begin{aligned} I(\tau) &\propto \int_0^\infty d\tau_3 \left|P(\tau_3,\tau)\right|^2 \propto \int_0^\infty d\tau_3 \left|\exp\left\{-\Gamma_{10}(\tau+\tau_3) - \frac{\Delta^2(\tau_3-\tau)^2}{2}\right\}\right|^2 \\ &= \frac{\sqrt{\pi}}{2\Delta}\exp\left(-4\Gamma_{10}\tau + \frac{\Gamma_{10}^2}{\Delta^2}\right)\operatorname{erfc}\left(\frac{\Gamma_{10}}{\Delta} - \Delta\tau\right) \end{aligned}, \qquad (2.74)$$

where the complementary error function erfc is defined as

$$\operatorname{erfc}(x) \equiv 1 - \operatorname{erf}(x) \equiv 1 - \int_0^\infty \exp(-x^2)dx. \qquad (2.75)$$

The graphic representation of eq. (2.74) is shown in fig. 2.14 varying $\Gamma_{10}$ for a fixed $\Delta = 1$. The maximum of the signal is shifted by $\tau$* with respect to $\tau = 0$ when inhomogeneous broadening starts to contribute to the spectrum, and the peak shift is an indicative of the transition from homogeneous to inhomogeneous broadening. In fact, when the system is extremely inhomogeneously broadened, the signal is always shifted. However, the tail of the signal decays according to eq. (2.72). The peak shift results from a competition between homogeneous damping and inhomogeneous rephasing.

### 2.4.4 Three-pulse photon echo

In two-pulse photon echo, the population time $\tau_2$ is null, since the last two interactions happen at the same time. The population time can be controlled in three-pulse photon echo [We85], whose scheme is represented in Fig. 2.15. Three pulses, $\boldsymbol{k}_1$, $\boldsymbol{k}_2$ and $\boldsymbol{k}_3$, propagating along different directions, are crossed at the sample. The temporal delay ($\tau$) between $\boldsymbol{k}_1$ and $\boldsymbol{k}_2$, as well as the delay ($T$) between $\boldsymbol{k}_2$ and $\boldsymbol{k}_3$ can be experimentally controlled. Two-pulse photon echo is a particular case of three-pulse photon echo when $\boldsymbol{k}_2 = \boldsymbol{k}_3$ and $T = 0$. The double-sided Feynman diagrams for three-pulse photon echo are represented in Fig. 2.16. The signal is emitted in the

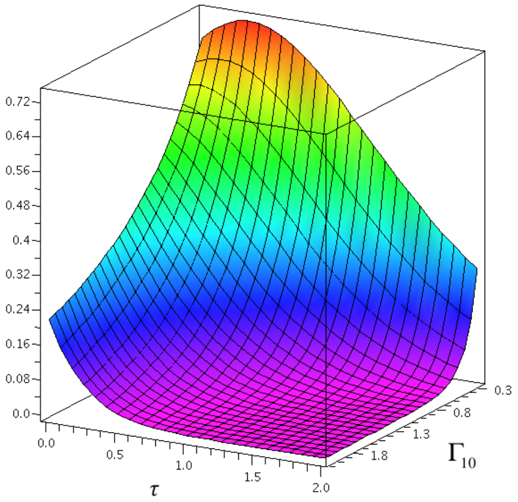

Fig. 2.14 – Plot of the peak shift of the two-pulse photon echo signal profile for various values of the homogeneous linewidth $\Gamma_{10}$. The peak shift represents a transition from homogeneous to inhomogenous broadening.

phase-matched direction $\boldsymbol{k}_4 = \boldsymbol{k}_3 + \boldsymbol{k}_2 - \boldsymbol{k}_1$. Likewise, the signal emitted in the $\boldsymbol{k}_5 = \boldsymbol{k}_1 - \boldsymbol{k}_2 - \boldsymbol{k}_3$ direction can be detected. At this moment, our focus is on the $\boldsymbol{k}_4$ signal in the semi-impulsive limit. Since the $\boldsymbol{k}_3$ pulse is the last interaction, exchanging the order of interaction between pulses $\boldsymbol{k}_1$ and $\boldsymbol{k}_2$ allows the nonrephasing diagrams to contribute to the signal in the $\boldsymbol{k}_4$ direction. In the diagrams $R_3$ and $R_4$, the first pulse $\boldsymbol{k}_1$ creates a coherence between excited and ground state. The second pulse $\boldsymbol{k}_2$, delayed by $\tau$ with respect to $\boldsymbol{k}_1$, drives the system into either ground or excited state where it can remain during the population time $T$, when the third pulse $\boldsymbol{k}_3$ sends the system back into a coherence state, with reversed phase with respect to first interaction. For diagrams $R_1$ and $R_2$, the analysis is the same as above except by the order of the first two interactions.

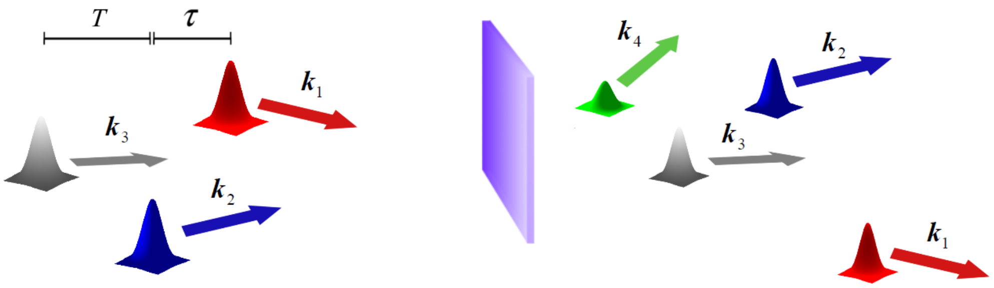

Fig. 2.15 – Representation of the three-pulse photon echo technique. The signal is launched along the $\boldsymbol{k}_4 = \boldsymbol{k}_3 + \boldsymbol{k}_2 - \boldsymbol{k}_1$ phase-matched direction.

An inhomogeneously broadened system tends to rephase after the third interaction. However, in addition to homogenous dephasing, the system can lose its ability of rephasing due to spectral diffusion, i.e. when the transition frequencies of the dipoles can migrate to other values within the inhomogeneous distribution. This happens because the inhomogeneous environment is not necessarily static, as the case of solvent reorganization, for example. As the system loses the rephasing capability, the peak shift $\tau^*$ tends to zero when increasing the population time $T$ (see for example fig. 2.17, reproduced from [Fe03]). The population time for which the system loses its rephasing capability is then connected to the spectral diffusion characteristic time $T_3$. It is important to mention that population decay during the population time may decrease the signal intensity. In this case, when investigating spectral diffusion, the condition $T_3 << T_1$ must be satisfied.

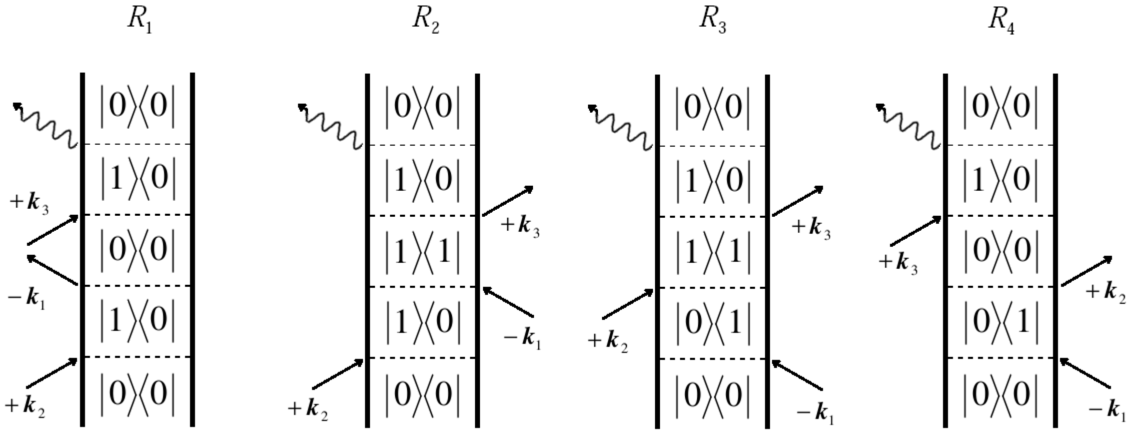

Fig. 2.16 – Double-sided Feynman diagrams of the three-pulse photon echo.

In the pioneering work of Weiner *et al.* [We85], the case of non-impulsive excitation has been treated assuming the temporal envelope of the pulses as Gaussian functions with pulsewidth $\tau_p$. It is very useful to describe this case here, since the results are quite similar to the technique we have employed in chapter 3 using incoherent pulses. Now, the strict temporal ordering of the interactions is no longer valid and the nonlinear polarization is not directly proportional to the response function. Thus, one has to deal with eq. (2.42) to calculate the third-order nonlinear polarization. The electric fields in that equation are a superposition of the incoming pulses with their respective time delays:

$$E(r,t') = a_1 e(t'+\tau)\exp(-i\boldsymbol{k}_1\cdot\boldsymbol{r}) + a_2 e(t')\exp(-i\boldsymbol{k}_2\cdot\boldsymbol{r}) + a_3 e(t'-T)\exp(-i\boldsymbol{k}_3\cdot\boldsymbol{r}) + c.c, \tag{2.76}$$

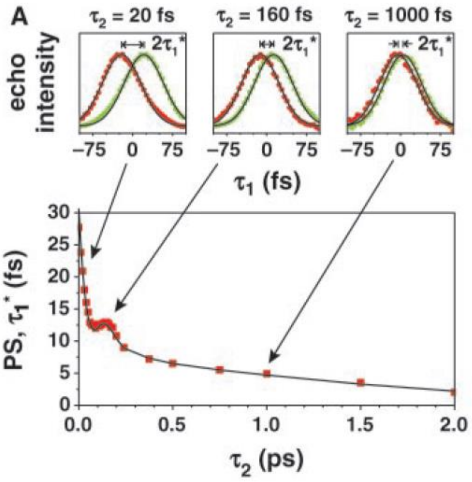

Fig. 2.17 – Three-pulse photon echo peak shift measurement of vibrational echoes in water (HOD) (Partially reproduced from Ref. [Fe03]).

where the pulses are considered to be derived from the same beam through the use of beam splitters. The $e(t)$ factors are the complex electric field envelope functions and the coefficients $a_i$ allow the possibility of different intensities of the three pulses. For simplicity, we will assume that the third pulse delay $T$ is much greater than the delay $\tau$ between the first and second pulses.

If the system is homogeneously broadened, all four diagrams contribute to the signal and its intensity profile is symmetric in $\tau$. Fig. 2.18 shows the calculated signal in the $\boldsymbol{k}_4$ direction (reproduced from [We85]) for various values of the normalized dephasing time $T_2/\tau_p$. The signal for $T_2/\tau_p = 0$ reflects the pulse autocorrelation $f(t) = \int e(t)e(t+\tau)dt$ and the dephasing time is extracted if the pulse autocorrelation is known.

For the case of extreme inhomogeneously broadening, only the rephasing diagrams $R_3$ and $R_4$ from fig. 2.16 contribute to the signal, since the non-rephasing diagrams $R_1$ and $R_2$ do not generate an echo field. This implies time-ordering: The system interacts first with $\boldsymbol{k}_1$ and then with $\boldsymbol{k}_2$. The signal is no longer symmetric in $\tau$. Fig 2.19 shows the calculated signal profile for different normalized coherence times assuming a Gaussian lineshape for inhomogeneous broadening. The signal is peaked at $\tau^* > 0$ and is not null for $\tau < 0$. This can be discerned as follows (fig. 2.20): the action of field $\boldsymbol{k}_1$ must precede that of $\boldsymbol{k}_2$. For $\tau < 0$ (fig 2.20a-c), the signal starts to be emitted only when there is a partial overlap between the pulses (fig 2.20b-c), since in this case, part of the $\boldsymbol{k}_1$ beam may excite the system first than part the $\boldsymbol{k}_2$ pulse. At $\tau = 0$ the pulses are completely overlapped; however the $\boldsymbol{k}_2$ pulse may excite the system first and,

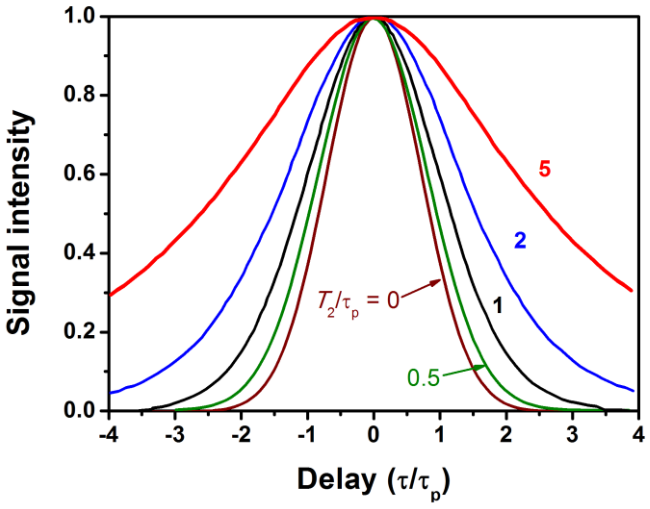

Fig. 2.18 – Profile of the signal generated in three-pulse photon echo for a homogeneously broadened ensemble (reproduced from [We85]).

when this happens, an echo is not emitted. For $\tau > 0$ (fig 2.20d-e), there is a competition between signal enhancement, due to the fulfillment of the temporal ordering condition, and homogeneous damping of the polarization during the coherence evolution. Hence the signal is peaked at $\tau^* > 0$ and the peak shift is a measurement of the contribution of homogeneous dephasing.

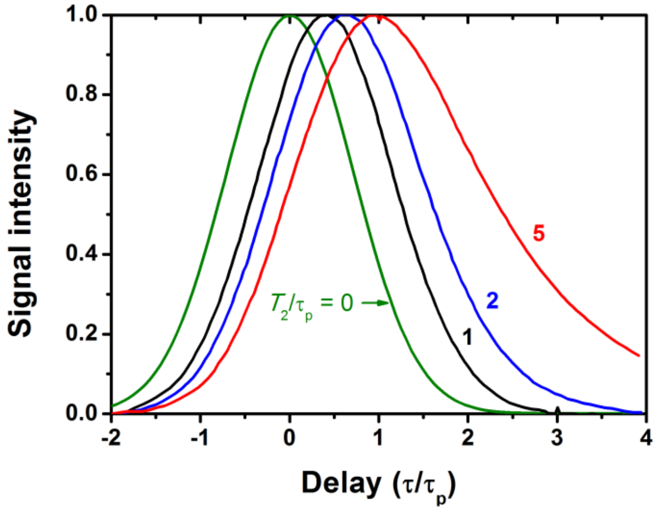

Fig. 2.19 – Profile of the signal generated in three-pulse photon echo of an inhomogeneously broadened ensemble (reproduced from [We85]).

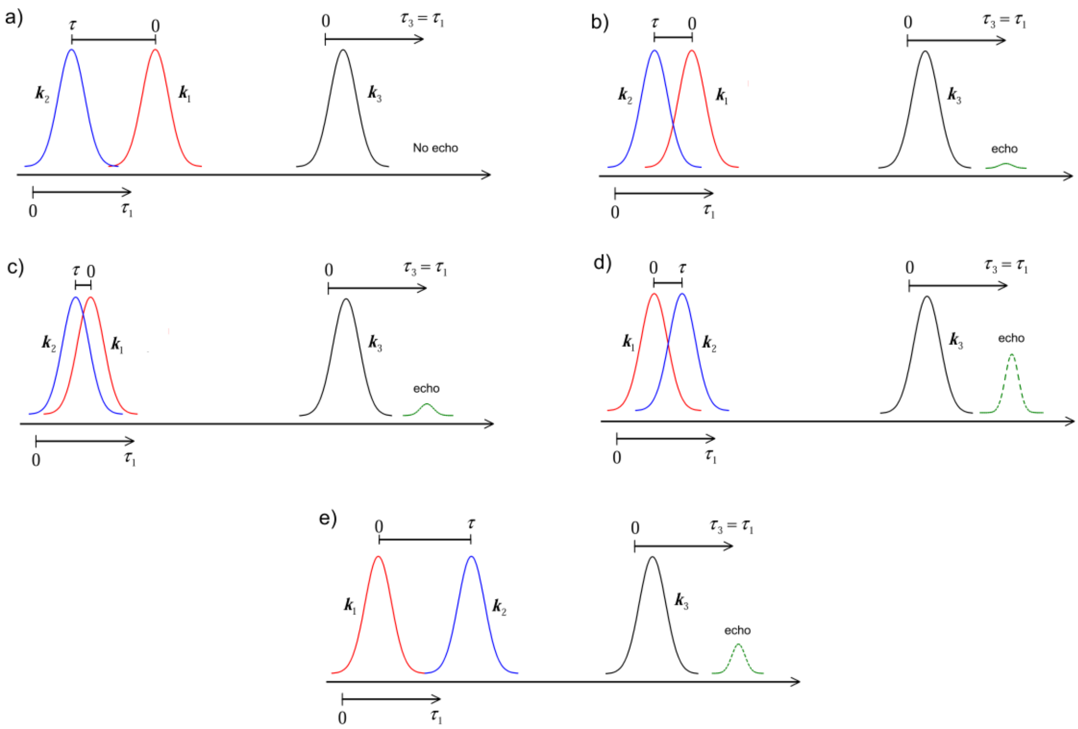

Fig. 2.20 – Pulse sequence of the three-pulse photon echo when the pulses can overlap in time.

The signal in the $\boldsymbol{k}_5 = \boldsymbol{k}_1 - \boldsymbol{k}_2 - \boldsymbol{k}_3$ direction can also be detected. In this case, the action of the $\boldsymbol{k}_1$ and $\boldsymbol{k}_2$ pulses is reversed in time compared to the $\boldsymbol{k}_4$ signal, and the signal profile in the $\boldsymbol{k}_5$ direction is identical to the $\boldsymbol{k}_4$ signal profile with $\tau \to -\tau$. Therefore, acquiring both $\boldsymbol{k}_4$ and $\boldsymbol{k}_5$ signals and measuring the peak shift $\tau_s$ between them, allows determining $T_2$ as shown in Fig. 2.21. When the normalized peak shift $\tau_s / \tau_p < 0.3$, the coherence time is equal to the peak shift $\tau_s$.

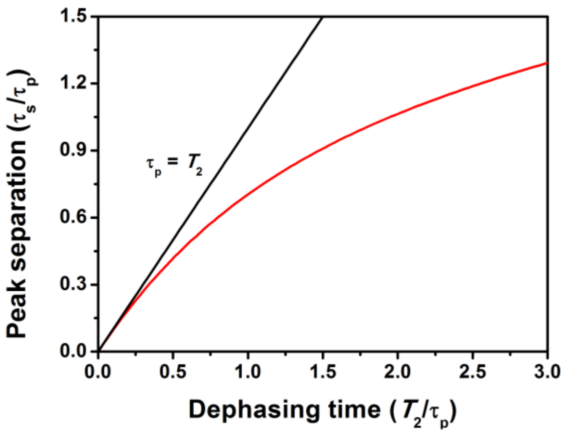

Fig. 2.21 – Calculated peak separation between the $\boldsymbol{k}_4$ and $\boldsymbol{k}_5$ pulses in three-pulse photon echo as a function of the dephasing time (reproduced from [We85]).

### 2.4.5 Spectral hole-burning

Photon echoes is a versatile time-domain technique that allows eliminating inhomogeneous broadening. By carefully controlling the temporal ordering of the incoming pulses, the analysis of the third-order nonlinear signals is somewhat simplified, separating the time scales of the contributions of homogeneous and inhomogeneous broadening and spectral diffusion. However, since the beams are broadband, photon echoes do not offer spectral resolution. Selective elimination of inhomogeneous broadening can be achieved in the frequency domain by the spectral hole burning technique [Vö89]. The scheme of a classical spectral hole burning experiment (Fig. 2.22) is as follows. A strong narrowband, and hence long, pump beam with frequency $\Omega_L$ selective excites a class of homogeneously broadened chromophores, with resonance frequency equal to $\Omega_L$, within the inhomogeneous distribution. A second tunable weak narrowband probe beam sweeps the whole inhomogeneous distribution of the ensemble. Since the strong pump beam can saturate the absorption close to $\Omega_L$, a hole is burned in that part of the spectrum. The width of the *hole-burning* dip is related to the homogeneous linewidth $\Gamma_{\text{hom}}$ and, therefore, to the coherence time via the relation

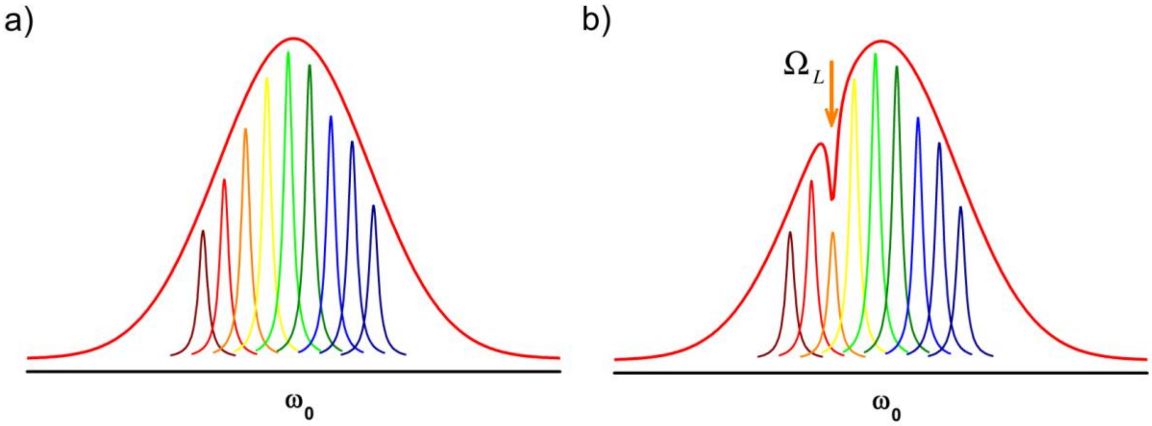

Fig. 2-22 – Representation of the spectral hole burning technique. The inhomogeneously broadened system a) is irradiated by a strong pump pulse in b). The laser saturates the probe absorption near the laser frequency $\Omega_L$.

$$T_2 = \frac{2\hbar}{\Gamma_{\text{hom}}} \tag{2.77}$$

The analysis of the hole width and its connection to $\Gamma_{\text{hom}}$ may require modeling and previous knowledge about the optical properties of the probed chromophores. That class of excited chomophores can absorb in another frequency, which can lie within or outside the inhomogeneous distribution. The excited subensemble can recover to its initial resonance frequency after some relatively short time (up to millisecond) after the pump beam is turned off. When this happens the technique is referred as transient hole burning. However the excitation can last longer (typically from seconds to minutes) or the subensemble can undergo a permanent modification. In this case, the technique is called *persistent spectral hole burning* (PSHB). In chapter 4, we will use PSHB to measure the dephasing time of localized surface plasmon resonance in colloidal silver nanoparticles.

The scheme of the hole burning technique is similar to the pump and probe using temporally long pulses. The connection of the hole burning technique with the nonlinear response function [Mu95] is unnecessary for the interpretation of most of the experiments and will not be made here.

## 2.5 Conclusions

In this chapter, we developed the formalism of the nonlinear response function for the interpretation of coherent nonlinear optical techniques. We have presented a class of nonlinear optical techniques related to the experiments performed in this thesis. Emphasis was given to the microscopic origin of the signal generated in four-wave mixing spectroscopies. The diagrammatic approach presented is very useful to that purpose because it tracks the evolution of the density operator that gives rise to the signal generated. The femtosecond transient absorption pump and probe technique allows us to extract population lifetimes, while in photon echoes and spectral hole burning we can measure the coherence times. The next chapters will be devoted to the microscopic interpretation of these parameters in a variety of nanoscale systems.

# 3. Ultrafast Exciton Dynamics in Glass-Ceramic Containing $NaNbO_3$ Nanocrystals

This chapter presents results of ultrafast dephasing dynamics of excitons in $NaNbO_3$ nanocrystals, embedded in a silica-niobia glass, investigated by degenerate four-wave mixing (DFWM) with incoherent light. The results are complemented by low-temperature luminescence experiments in order to understand the role of trap states to the optical properties of this composite. The chapter begins discussing in details the DFWM technique using spectrally broad and temporally long pulses. In this part, we make use of the quantum-mechanical formalism developed in chapter 2 for the nonlinear optical polarization. In spite of the long pulse duration, the stochastic nature of incoherent pulses allows to investigate dynamical processes in a time scale on the order of the noisy light correlation time, which is much shorter than the pulse duration. The incoherent version of the technique is compared to the results presented in chapter 2 using femtosecond pulses. After that, a brief review of the results already found in the literature for the nonlinear optical properties of this composite is made. Finally we present original results of this thesis and discuss them with basis on the theory presented earlier and the general optical properties of solids.

## 3.1 Coherent Spectroscopy with Incoherent Light

### 3.1.1 Historical

In the 1980's, it was reported that broadband incoherent light could be used to achieve femtosecond temporal resolution regardless of the the pulse duration. The parameter that determines the temporal resolution is the pulse correlation time $\tau_c$, which is inversely proportional to the pulse bandwidth. At that time, developing ultrafast lasers was a challenging task and that discovery motivated a rapid advance in the field of ultrafast spectroscopy with incoherent light. If the linear interferograms of incoherent pulses behave similarly to femtosecond pulses, i.e. show a high interferometric contrast for time delays smaller than the correlation time, it is natural to expect that they can behave like short pulses in time-resolved nonlinear spectroscopies. The initial experiments were made mostly by several Japanese groups.

In [As84], Asaka *et al.* performed a two-pulse photon echo-like experiment in $Nd^{3+}$-doped silicate glass using two different incoherent light sources, an imperfectly mode-locked dye-laser and a broadband CW dye laser, for which they could obtain subpicosecond resolution in the photon echoes decay profile: 0.22 ps and 0.70 ps for the imperfectly mode-locked and the CW laser, respectively. In [Mo84], Morita and Yajima developed the theoretical basis for nonlinear time-resolved spectroscopy with broadband long pulses. Using the same semiclassical approach presented in chapter 2 for the nonlinear polarization, they derived the expression for the signals in a two-pulse photon echo-like experiment. The signal field generated in this kind of experiments carries the same statistical properties of the input fields. Since the signal is stochastic, a statistical average of the signal must be performed under homodyne detection with slow detectors. They considered the incoherent light as a stationary complex Gaussian random process and performed the calculation assuming delta functions for the autocorrelation between the pulses. We will discuss in more details these results in the next subsection.

Incoherent light also have been applied in other time-resolved techniques, such as coherent Stokes (CSRS) and anti-Stokes Raman (CARS) scattering [Ha87], Kerr relaxation [Ku87], pump-probe for population relaxation [To86] and forced-light scattering [Ku94] among others. For almost every femtosecond technique, there is a noisy light counterpart.

One interesting aspect of incoherent light is that, contrary to coherent ultrashort pulses, the phase relationship between different spectral components of the noisy pulse is a random function. One of the consequences of this fact is that high spectral resolution of transition frequencies can be obtained in coherent spectroscopies with noisy light, since the different frequencies are in principle uncorrelated and each transition frequency can be probed independently, rather than coherently as for coherent broadband pulses. CARS with incoherent pulses generally employ one narrowband and two noisy beams with monochromatic detection. The spectral resolution of the Raman frequencies is limited by the bandwidths of the narrowband beam and the spectral filter of the monochromator. Spectral resolution up to 0.5 $cm^{-1}$ in this scheme can be achieved [Mi96]. On the other hand, CARS with femtosecond broadband pulses is limited, in principle, by the bandwidth of the pulses (typically ca. 150 $cm^{-1}$ for a 100 fs laser pulse in the near-infrared), giving rise to a large undesirable nonresonant background in CARS microscopy, for example. Several different schemes have been proposed using pulse shaping techniques to improve this spectral resolution [Or02] [Du02] [Po08] [Xu08] and this is indeed a hot topic of research.

Coherent control of nonlinear processes also can be achieved with incoherent light. Dayan *et al.* [Da04] performed a coherent control experiment of two-photon absorption (TPA) in Rb vapor using, as incoherent light source, the broadband light generated (both signal and idler) in an optical parametric oscillator (OPO) by down-conversion of a narrowband nanosecond pulse. The signal and idler beams, which are correlated, were mixed in the Rb vapor cell and the up-converted light emitted by the Rb vapor was detected. The spectral phase of the signal beam could be controlled, using a spatial light modulator, as well its temporal delay relative to the idler beam. The results obtained were similar to what is expected using femtosecond pulses having the same bandwidth. Later, Ferraz *et al*. [Fe05] performed coherent control of four-wave mixing in a Rb cell vapor using a broadband dye laser as incoherent light source and a narrowband beam. The dye laser beam was split in a Michelson interferometer and the splitted beams were mixed in the cell. The narrowband beam was used to stimulate the emission of the population excited by the noisy beams. By controlling the relative polarization between the dye laser beams, it was possible to select the quantum pathways that generate the signal and suppress the optical interferences, leaving only quantum interferences.

In the following section, we will discuss in more detail the aspects of the degenerate four-wave mixing with incoherent light technique and compare with the ultrashort pulse version of the technique.

### 3.1.2 Degenerate four-wave mixing with incoherent light

In this section, we will develop analytic results for degenerate four-wave mixing with incoherent light (DFWMIL) in the self-diffraction configuration for a two-level system. The scheme of this technique is similar to the two pulse photon-echo; however, we will use another name for the noisy version to avoid further misunderstanding in the microscopic origin of the signals, which differ one from another. The section will partially follow the lines discussed in details in refs. [Mo84] and [Ko88] and use the results developed in chapter 2.

In DFWMIL, a laser beam with center frequency $\omega$ generated by an incoherent light source is split into two twin beams with wavevectors $\boldsymbol{k}_1$ and $\boldsymbol{k}_2$. The $\boldsymbol{k}_2$ beam is delayed by $\tau$ with respect to the $\boldsymbol{k}_1$ beam. We assume $\tau > 0$ when $\boldsymbol{k}_1$ precedes $\boldsymbol{k}_2$. The degenerate beams are crossed in the sample of interest and the phase-matched signals in the directions $\boldsymbol{k}_3 = 2\boldsymbol{k}_2 - \boldsymbol{k}_1$ and $\boldsymbol{k}_4 = 2\boldsymbol{k}_1 - \boldsymbol{k}_2$ are detected. Our focus now is on the $\boldsymbol{k}_3$ signal, since the results for $\boldsymbol{k}_4$ are the obtained making $\tau \to -\tau$. The total electric field in the sample is given by

$$E(\boldsymbol{r},t) = \tilde{E}(t+\tau)\exp\{-i[\omega(t+\tau)+i\boldsymbol{k}_1\cdot\boldsymbol{r}]\} + \tilde{E}(t)\exp\{-i[\omega t + i\boldsymbol{k}_2\cdot\boldsymbol{r}]\} + c.c.. \quad (3.1)$$

Now the semi-impulsive limit cannot be assumed, because nanosecond pulses are typically used in this technique. The double-sided Feynman diagrams that survive under RWA approximation for the signal in the $\boldsymbol{k}_3$ direction are shown in Fig. 3.1.

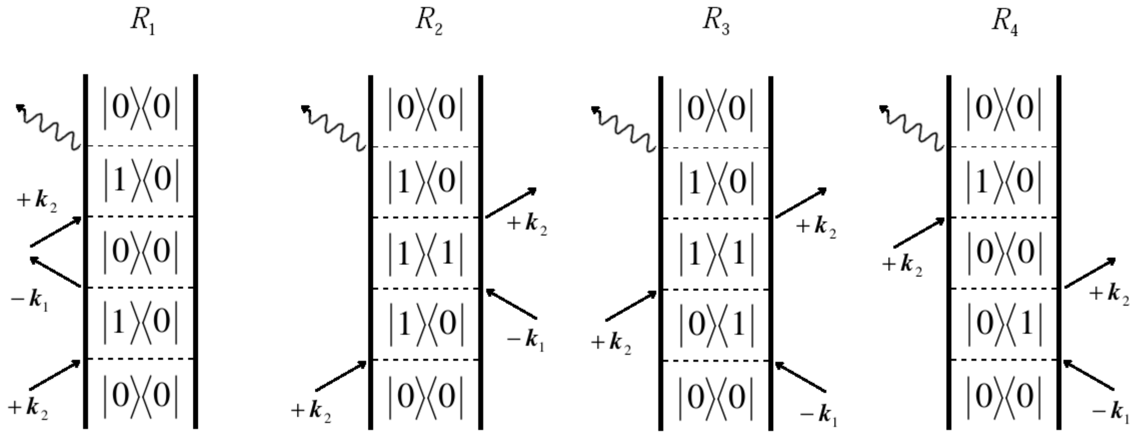

Fig. 3.1 – Double-sided Feynman diagrams for the DFWMIL technique.

The macroscopic polarization induced by the noisy beams, which is responsible for the signal generated in the four-wave mixing, can be found through the perturbative expansion for the density operator. For the $\boldsymbol{k}_3$ direction, it is given by [Ko88]

$$P(t,\tau) \propto \exp\{i[\boldsymbol{k}_3 \cdot \boldsymbol{r} - \omega t]\} \int d\omega_{10}\, g\left(\omega_{10} - \omega_{10}^{(0)}\right) \int_{-\infty}^{\infty} dt_3 \int_{-\infty}^{t_3} dt_2 \int_{-\infty}^{t_2} dt_1 \exp[-(t_3 - t_2)/T_1]$$
$$\exp[-(t - t_3 + t_2 - t_1)/T_2] \left\{ \begin{aligned} &\tilde{E}(t_3)\tilde{E}(t_2)\tilde{E}^*(t_1+\tau)\exp\left[-i\left(\omega_{10}^{(0)} - \omega\right)(t - t_3 + t_2 + t_1)\right] \\ &+ \tilde{E}(t_3)\tilde{E}^*(t_2+\tau)\tilde{E}(t_1)\exp\left[-i\left(\omega_{10}^{(0)} - \omega\right)(t - t_3 - t_2 - t_1)\right] \end{aligned} \right\} \tag{3.2}$$

where $T_1$ and $T_2$ are the population relaxation and dephasing times respectively, and $g\left(\omega_{10} - \omega_{10}^{(0)}\right)$ is the inhomogeneous lineshape. The signal intensity is given by

$$I(\tau) \propto \int_0^{\infty} dt \left\langle |P(t,\tau)|^2 \right\rangle, \tag{3.3}$$

where $\langle\ \rangle$ denotes statistical average. This is another aspect of the difference between the techniques that employ coherent or incoherent light. Since the polarization is a stochastic function when the incoming fields are noisy, it needs to be stochastically averaged. To evaluate (3.3), it is necessary to make the product of the polarization $P(t,\tau)$ in Eq. (3.2) with its complex conjugate

$$P^*(t,\tau) \propto \exp\{-i[\boldsymbol{k}_3 \cdot \boldsymbol{r} - \omega t]\}\int d\omega_{10}\, g\left(\omega_{10}-\omega_{10}^{(0)}\right)\int_{-\infty}^{\infty} ds_3 \int_{-\infty}^{s_3} ds_2 \int_{-\infty}^{s_2} ds_1 \exp[-(s_3-s_2)/T_1]$$
$$\exp[-(t-s_3+s_2-s_1)/T_2]\begin{Bmatrix} \tilde{E}^*(s_3)\tilde{E}^*(s_2)\tilde{E}(s_1+\tau)\exp\left[i\left(\omega_{10}^{(0)}-\omega\right)(t-s_3-s_2+s_1)\right] \\ +\tilde{E}^*(s_3)\tilde{E}(s_2+\tau)\tilde{E}^*(s_1)\exp\left[i\left(\omega_{10}^{(0)}-\omega\right)(t-s_3+s_2-s_1)\right] \end{Bmatrix} \tag{3.4}$$

The intensity of the signal is the stochastic average of the product of complex conjugated polarizations evolving into two distinct timelines (*t* and *s*). This product contains the sum of four terms involving the stochastic average of the product of six electric fields, namely:

1) $\left\langle \tilde{E}(t_3)\tilde{E}(t_2)\tilde{E}^*(t_1+\tau)\tilde{E}^*(s_3)\tilde{E}^*(s_2)\tilde{E}(s_1+\tau)\right\rangle$

`(3.5a)

2) $\left\langle \tilde{E}(t_3)\tilde{E}(t_2)\tilde{E}^*(t_1+\tau)\tilde{E}^*(s_3)\tilde{E}(s_2+\tau)\tilde{E}^*(s_1)\right\rangle$ (3.5b)

3) $\left\langle \tilde{E}(t_3)\tilde{E}^*(t_2+\tau)\tilde{E}(t_1)\tilde{E}^*(s_3)\tilde{E}^*(s_2)\tilde{E}(s_1+\tau)\right\rangle$ (3.5c)

4) $\left\langle \tilde{E}(t_3)\tilde{E}^*(t_2+\tau)\tilde{E}(t_1)\tilde{E}^*(s_3)\tilde{E}(s_2+\tau)\tilde{E}^*(s_1)\right\rangle$ (3.5d)

To evaluate the expression, it is necessary that we assume certain characteristics of the stochastic fields. The electric fields can be broken into the product of two terms:

$$\tilde{E}(t) = \varepsilon(t)p(t), \tag{3.6}$$

where $\varepsilon(t)$, the temporal envelope of the long pulse, is a slowly varying function (deterministic) and $p(t)$ is a complex random function. Assuming that the field of incoherent light is a superposition of random independent fields, the Central Limit Theorem assures that the sum of these random fields (variables) is a random variable which obeys a complex Gaussian statistics, for which [Ma95] [Me01]

$$\left\langle p^*(t)p(t-\tau)\right\rangle = G(\tau), \tag{3.7a}$$

$$\left\langle p(t)p(t+\tau)\right\rangle = \left\langle p^*(t)p^*(t+\tau)\right\rangle = 0, \tag{3.7b}$$

$$\left\langle p(t)\right\rangle = \left\langle p^*(t)\right\rangle = 0, \tag{3.7.c}$$

where $G(\tau)$ is the autocorrelation function of the stochastic fields assuming a stationary process. Equations (3.5a)-(3.5d) represent the sixth-order moment of the random process $p(t)$. An nth-order moment of a complex Gaussian stochastic process can be factorized into *n* products of second-order momenta. Hence, the four terms in eqs. (3.5a)-(3.5d) give rise to 24 terms each of which is the product of three two-point correlation functions. It is instructive to perform this operation for eq. (3.5a):

$$\begin{aligned}
&\left\langle \tilde{E}(t_3)\tilde{E}(t_2)\tilde{E}^*(t_1+\tau)\tilde{E}^*(s_3)\tilde{E}^*(s_2)\tilde{E}(s_1+\tau)\right\rangle = |\varepsilon(t)|^6 \times \{ \\
&\left\langle p(s_1+\tau)p^*(s_2)\right\rangle\left\langle p(t_2)p^*(t_1+\tau)\right\rangle\left\langle p(t_3)p^*(s_3)\right\rangle \\
&+\left\langle p(s_1+\tau)p^*(s_3)\right\rangle\left\langle p(t_2)p^*(t_1+\tau)\right\rangle\left\langle p(t_3)p^*(s_3)\right\rangle \\
&+\left\langle p(s_1+\tau)p^*(s_2)\right\rangle\left\langle p(t_3)p^*(t_1+\tau)\right\rangle\left\langle p(t_2)p^*(s_3)\right\rangle \\
&+\left\langle p(s_1+\tau)p^*(s_3)\right\rangle\left\langle p(t_3)p^*(t_1+\tau)\right\rangle\left\langle p(t_2)p^*(s_2)\right\rangle \\
&+\left\langle p(s_1+\tau)p^*(t_1+\tau)\right\rangle\left\langle p(t_2)p^*(s_3)\right\rangle\left\langle p(t_3)p^*(s_2)\right\rangle \\
&+\left\langle p(s_1+\tau)p^*(t_1+\tau)\right\rangle\left\langle p(t_2)p^*(s_2)\right\rangle\left\langle p(t_3)p^*(s_3)\right\rangle\}
\end{aligned} \tag{3.8}$$

Since for a stationary process, the autocorrelation function depends only on time intervals, the factors $\left\langle p(s_1+\tau)p^*(t_1+\tau)\right\rangle$ are independent of the delay time $\tau$.

The analytic expression of the total signal is rather cumbersome and will not be presented here (see [Mo84] for the total expression); only the calculated intensity profile will be. In [Mo84], the authors assumed a delta correlation function for both homogeneous and extremely inhomogeneous broadening case. Figure 3.2 shows the typical intensity profiles for the two cases and compares with the results of two-pulse photon echo with coherent femtosecond pulses. In both cases the signal profile reflects the influence of the dephasing rate $1/T_2$. Three main conclusions emerge from the comparison of the profiles:

1) The signal profiles are not necessarily exponential curves. For a homogeneously broadened system, the decay of the signal can be approximated by an exponential function with a decay rate equal to $2/vT_2$, where $v$ is a parameter that depends on the ratio between $T_2$ and $T_1$. For an extremely inhomogeneously broadened system, the signal decays approximately exponentially at a rate equal to $4/vT_2$;

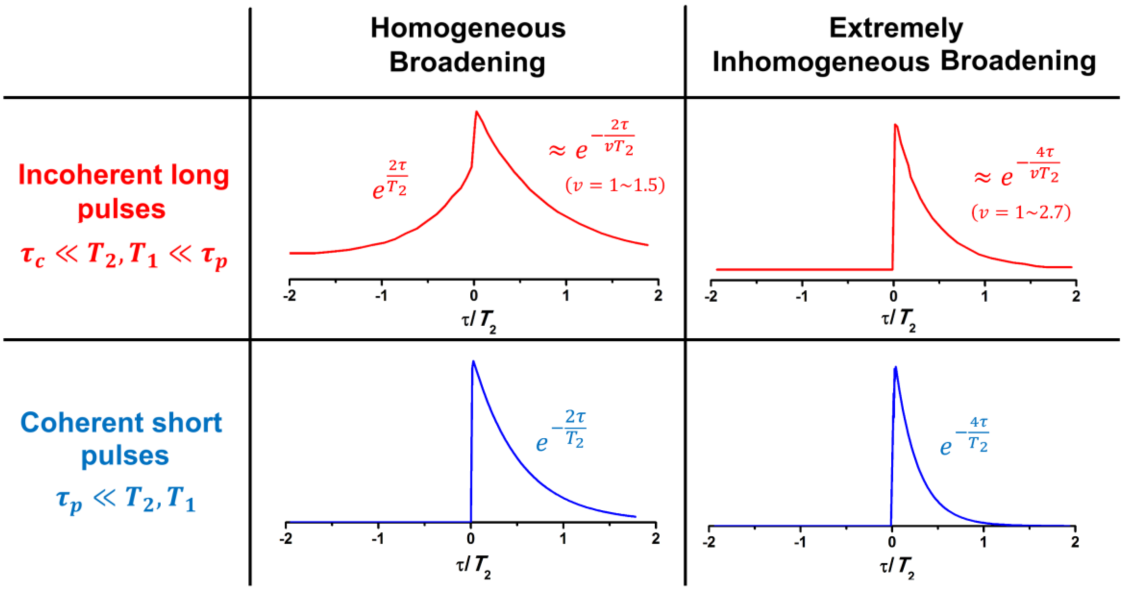

Fig. 3.2 – Typical signal profiles for the DFWMIL technique assuming delta functions for the autocorrelation of the noisy light (data taken from [Mo84]).

2) For homogeneous broadening, the signal increases exponentially with the delay at negative delays $\tau < 0$;

3) There is a constant background in both cases. This is the contribution of the $\tau$-independent terms when breaking up the sixth-order moment into a sum of products of second-order moment.

The authors considered the incoherent light as a train of uncorrelated random pulses and therefore, the signal in DFWMIL is an accumulation of individual signals generated by multiple combinations of three of these pulses i.e., the total signal is an accumulation of multiple three-pulse photon echo signals.

When the autocorrelation function of the stochastic processes is finite, and assuming that the population lifetime is much larger than the dephasing time and the correlation time of the light ($\tau_c$), the integrated intensity of the signal in the $\boldsymbol{k}_3 = 2\boldsymbol{k}_2 - \boldsymbol{k}_1$ direction is given, for an extremely inhomogeneous broadened system, by [Ko88] (see appendix A)

$$I(\tau) \propto \int_0^\infty d\tau_3 \int_0^\infty d\sigma_3 G(\sigma_3 - \tau_3) G(\tau_3 - \tau) G^*(\sigma_3 - \tau) \exp\left[-\frac{2(\tau_3 + \sigma_3)}{T_2}\right]. \qquad (3.9)$$

This result is exactly the expression for three-pulse photon echo with coherent femtosecond pulses, analyzed in detail in chapter 2. When the dephasing time is very short compared to the correlation time of the light, the signal does not have a pronounced tail. For $T_2$ long compared to τ$_c$, the signal decays exponentially at a rate $4/T_2$. The signal in the $\boldsymbol{k}_3 = 2\boldsymbol{k}_2 - \boldsymbol{k}_1$ direction (fig. 2.19) is peaked at $\tau > 0$. Likewise, the $\boldsymbol{k}_4 = 2\boldsymbol{k}_1 - \boldsymbol{k}_2$ signal, which is found by making $\tau \to -\tau$, is peaked in the opposite direction. The separation between their peaks $\tau_s$ furnishes the value of $T_2$ (Fig. 2.21). If $T_2$ is short compared to τ$_c$, the separation between the peaks is equal to the dephasing time. As in three-pulse photon echo, DFWMIL allows measurement of dephasing times shorter than the correlation time of the light.

In fact, inhomogeneous broadening in real systems is always finite. Therefore, the value of the dephasing time estimated by the peak separation may be a lower bound to its real value: if inhomogeneous and homogeneous broadening are comparable, the two mechanisms cannot be completely distinguished and the peak separation tends to decrease, approaching to zero in the homogeneous limit. The dependence of the ratio (peak separation)/(dephasing time) with the ratio homogenous/inhomogeneous linewidth can be calculated in the region where the peak separation is equal to the dephasing time assuming a Gaussian function for the inhomogeneous lineshape distribution (eq. 2.70). Then we have [Ko88]

$$\frac{\tau_s}{T_2} = \frac{u\left\{(2u + 1/u) - \left(4u^2 + 4 - 1/u^2\right)\exp\left(u^2\right)\mathrm{erfc}(u)\right\}}{1 - (2u - 1/u)\exp\left(u^2\right)\mathrm{erfc}(u)}, \tag{3.10}$$

where $u \equiv 1/T_2\Delta$ is the ratio between homogeneous and inhomogeneous linewidth. Equation (3.10) is depicted in fig. 3.3.

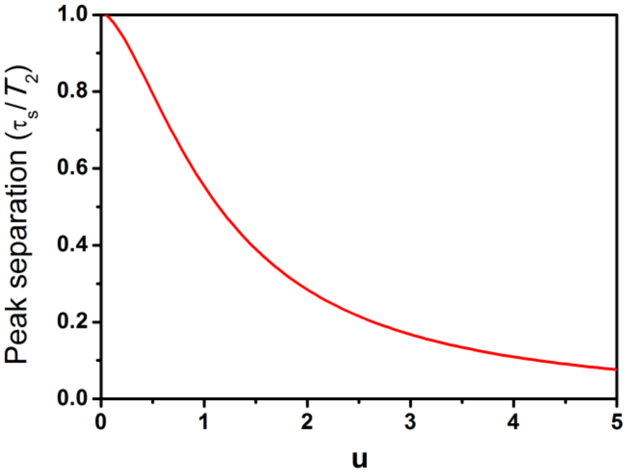

Fig. 3.3 – Relationship between the ratio peak separation/dephasing time and the ratio homogeneous/inhomogeneous broadening (u) for the linear region in Fig. 2.21 (data taken from Ref. [Ko88]).

It is instructive now further comparison between the techniques which employ ultrashort coherent pulses with those which employ noisy light. One important advantage of using incoherent light techniques is that the autocorrelation traces of incoherent light are not broadened when the beams travel through compensated paths that contain dispersive media such as lenses [Go89]. On the other hand, femtosecond pulses are easily dispersed and care has to be taken to avoid using long-path optical components (for example, beam-splitters, lenses, half and quarter waveplates) in an experiment. In the ultraviolet, as the case of the experiment in this chapter, this is critical since the dispersion of the refractive index increases with the frequency.

Another advantage, perhaps the principal, is the fact that incoherent light can be employed to study ultrafast processes and yet achieve a high spectral resolution. This can be discerned with basis on the Wiener-Khinchin theorem [Ma95], which states that the autocorrelation function of a random variable *p* is the Fourier transform of its spectral density $J(q)$:

$$G(\tau) = \left\langle p(\tau)p^*(0)\right\rangle = \int_{-\infty}^{\infty} dqJ(q)\exp(-iq\tau). \tag{3.11}$$

Expressing the correlation function in the frequency space, we have:

$$\begin{aligned}\left\langle \tilde{p}(q)\tilde{p}^*(q')\right\rangle &= \left\langle \int_{-\infty}^{\infty} dtp(t)\exp(iqt)\int_{-\infty}^{\infty} dt'p^*(t')\exp(-iq't')\right\rangle = \\ &\int_{-\infty}^{\infty} dt\int_{-\infty}^{\infty} dt'\left\langle p(t)p^*(t')\right\rangle \exp[iq(t-t')]\exp[i(q-q')t'] = \\ &\int_{-\infty}^{\infty} dt'\int_{-\infty}^{\infty} d\tau' G(\tau')\exp[iq\tau']\exp[i(q-q')t'] = \\ &\int_{-\infty}^{\infty} dt'J(q)\exp[i(q-q')t'] = J(q)\delta(q-q')\end{aligned}, \tag{3.12}$$

where in the third step we defined a new variable $\tau' = t - t'$. Equation (3.12) states that a given frequency in the noisy light spectrum is infinitely correlated with itself and has no correlation with the others. This is why incoherent light is regarded sometimes to be *color-locked* [Ul03] [Ta05]. According to this point of view, incoherent light can be considered to be an incoherent superposition of coherent monochromatic beams. Therefore, incoherent light can achieve the spectral resolution of monochromatic beams and the temporal resolution of femtosecond pulses. This is particularly useful in coherent Raman spectroscopies as discussed earlier in this chapter.

One of the main disadvantages of incoherent light are possible accumulative thermal effects when long pulses are used because more energy is deposited in the sample compared to femtosecond pulses of the same intensity. In DFWMIL, the thermal grating can be avoided by using perpendicular polarizations. However, in some cases, this can not be avoided. Furthermore, other accumulative effects may arise due to the long pulse duration. In [Ko99], the authors reported light-induced inhomogeneous broadening in DFWMIL in an ethanol solution of rhodamine. When increasing the beam intensities, a set of vibronic levels of the excited states become populated, increasing the separation between the peaks of the self-diffracted $\boldsymbol{k}_3$ and $\boldsymbol{k}_4$ beams. To avoid these accumulative effects, generation of ultrashort incoherent pulses would be helpful. One interesting approach for the generation of ultrashort noisy pulses was given in [Xu08] (for application in CARS). The authors generated femtosecond noisy pulses by positioning a spatial light modulator in the Fourier plane of a 4*f* system and applying a random phase shift between the previously phase-locked spectral components of the pulse.

Another disadvantage of coherent spectroscopy with noisy light is the constant signal background present in most of the techniques, which reduces the signal-to-noise ratio.

The analysis of the results of noisy light nonlinear spectroscopies requires more sophisticated modeling compared to ultrashort pulses. The stochastic average of the integrated signal increases the number of terms of the nonlinear polarization in such a way that in some cases the calculations are impractical. A very important advance in the interpretation of noisy light was achieved by Dugan and Albrecht [Du91] and later by Ulness [Ul97]. In [Du91] the authors, in a fully quantum-mechanical formalism for coherent nonlinear spectroscopy, introduced the bichromophoric model, which states that the homodyne detected signal is the sum of contributions of signals generated by at least two-spatially distinct chomophores evolving into distinct timelines. This can be discerned as follows. The signal generated by the sample is the sum of the fields emitted by several distinct chomophores. When homodyne detected, it is necessary to multiply the signal field by its complex conjugated. Therefore the integrated signal is dominated by a sum of cross-terms which are contributions of two distinct chromophores in conjugated actions of the field. Later in [Ul96], a set of diagrams based on the bichromophoric model, called factorized time correlation (FTC) diagrams, were introduced to rationalize the terms involved in the statistical average of the signal at the intensity level. For each term (see eq. 3.6) that contains products of second-order correlation functions, it is possible to construct a FTC diagram that represents conjugated action of the incoming field in the two-chromophores in distinct timelines (*t* and *s* in Eq. 3.6). Also, the analytic results can be extracted from these diagrams. The bichromophoric model is general for other spectroscopies using coherent ultrashort pulses. However, in this case, the double-sided Feynman diagrams are sufficient to describe the nonlinear polarization.

## 3.2 Luminescence and Excitonic Dephasing in a Glass-ceramics Containing Sodium Niobate Nanocrystals

### 3.2.1 Introduction

After discussing in some detail the technique employed to study optical dephasing in $NaNbO_3$ nanocrystals, we now discuss the optical properties of a glass-ceramics embedding these nanocrystals.

Glass-ceramics (GCs) are glasses containing crystals with nano/micrometric dimensions and are prepared through controlled crystallization of a starting glass [Mc79]. They have many applications as thermal and mechanically stable devices, bioactive and photonic materials [Za10]. In particular, the photonic applications and prospects of GCs include displays, optical waveguides/fibers, up-conversion and amplification devices, photothermal refractive materials and color filters [Be99] [Al10a] [Sa02].

Glass-ceramics share the physical properties of glasses and ceramics. However, they may present entirely new physical properties compared to the glasses or ceramics which constitute the GCs. They can, for example, depending on the size of the nanocrystals, exhibit quantum confinement effects [Pr04]. This allows flexibility in the tunability of the optical band-gap and this capability is employed in color filters, for example. Furthermore, the mismatch between the dielectric constants of the nanocrystals and the host can enhance linear and nonlinear optical properties of the GCs due to increased electromagnetic field inside and at the vicinities of the nanocrystals.

When designing GCs for photonic applications, care must be taken to avoid undesirable light scattering due to the refractive index mismatch among the crystals and the host. To achieve that, the dimensions of the nanocrystallites must be smaller than the light wavelength [Ti00].

Glass-ceramics containing ferroelectric nanocrystals of the $ABO_3$ group (for example, $LiNbO_3$, $BaTiO_3$ and $NaNbO_3$) are attractive materials because these crystals are widely used in electro/nonlinear optical applications [Li01a]. The nonlinear optical properties of GCs containing sodium niobate ($NaNbO_3$) nanocrystals (GC-SNN) have been investigated recently aiming to applications in all-optical switching and optical limiting. In [Fa04], the authors investigated the nonlinear optical response of GC-SNN at visible and near infrared in the picosecond and femtosecond regime. They found that the crystalline phase enhances the modulus of its nonlinear refractive index $n_2$ and its two-photon absorption (TPA) coefficient $\alpha_2$. The optical Kerr relaxation at 800 nm was also investigated and a temporal response limited to the pulse duration (100 fs) was revealed, indicating that the contribution to the optical nonlinearity is essentially nonresonant. Figures-of-merit were calculated and indicated that the material is suitable for all-optical switching applications.

The optical limiting behavior of the GC-SNN was probed by nanosecond pulses in the visible and near infrared [Ol07]. The nonlinear absorption behavior in the nanosecond regime is different from the picosecond regime investigated earlier [Fa04]. This discrepancy was explained by contribution of excited state absorption (ESA) to the nonlinear absorption. A theoretical model including ESA besides TPA was applied to the nonlinear absorption data to extract the values of ESA cross-sections.

In this thesis, we have investigated the contribution of states with energies smaller than the band-gap of the material to the linear/nonlinear optical properties of the GC-SNN. The techniques we employed were low-temperature photoluminescence and DFWMIL.

### 3.2.2 Experimental details

The samples were prepared by Prof. Andrey Lipovskii's group of the St. Petersburg State Polytechnical University, St. Petersburg, Russia. A detailed description of the synthesis is given in [Li03b]. The glass with molar % composition of $35SiO_2$-$31Nb_2O_5$-$19Na_2O$-$11K_2O$-2CdO-$2B_2O_3$ was annealed at 610ºC during different time intervals. The nucleation of $NaNbO_3$ nanocrystals was confirmed by X-ray diffraction (XRD), as shown by the X-ray diffractograms in Fig. 3.4 for samples heat-treated during 2 h and 206 h. The filling fraction *f* i.e., the volumetric fraction of the crystalline phase, increases during the annealing process. However, after 69 h, a saturation of *f* is observed. The size of the nanocrystals is independent of the annealing time as confirmed previously by small angle X-ray scattering [Zh04]. The presence of $NaNbO_3$ nanocrystals was also verified by transmission electron microscopy (TEM) as shown in Fig. 3.5 along with the histogram of the size distribution of the nanocrystals. Their average size, found by fitting a log-normal curve to the histogram, is ≈ 12 nm.

The photoluminescence (PL) experiments were performed in samples heat-treated for 2 h ($f = 0.00$)

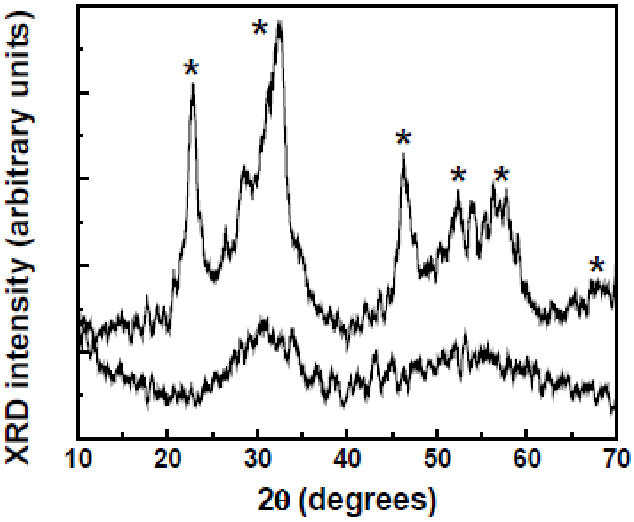

Fig. 3.4 – X-ray diffractogram of the GC-SNN with *f* = 0 (bottom curve) and *f* = 0.37 (upper curve). The asterisks indicate the peaks corresponding to quasicubic crystalline $NaNbO_3$.

and 206 h (*f* = 0.37). These two samples were chosen to distinguish among the optical properties of the bare glass i.e., sample annealed during 2 h, with those of the nanocrystals. The excitation source was the third-harmonic (λ = 355 nm) of a Nd-YAG laser (Continuum, Surelite II) operating at 5 Hz and with 5 ns of pulse duration generated by mixing the fundamental radiation (1064 nm) with its second harmonic (532 nm) in a KDP nonlinear crystal. The samples were mounted in a closed-cycle helium cryostat and the temperature could be varied from room temperature down to 17 K. The laser beam was focused in the samples with intensity ≈ 50 $MW/cm^2$. The luminescence, collected

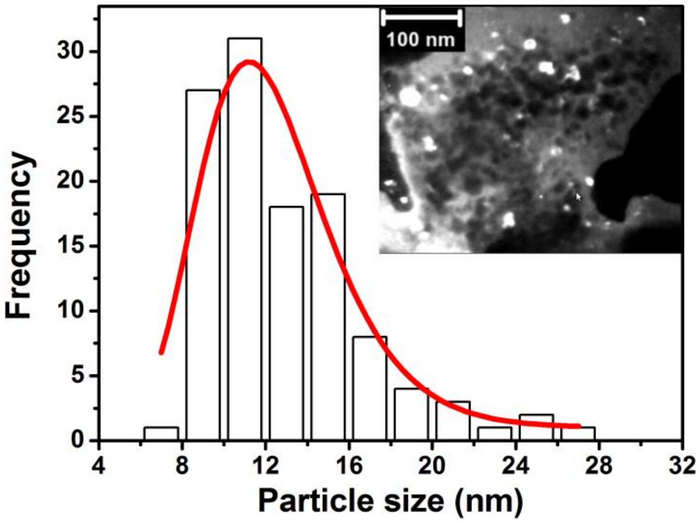

Fig. 3.5 – Representative size distribution of the $NaNbO_3$ nanocrystals in the glass-ceramic. Inset: Dark-field TEM image of the sample with *f* = 0.37.

perpendicular to the excitation, was analyzed by a 0.25 m (SPEX Minimate) spectrometer (spectral resolution: 25 Å) attached to a 1P28A photomultipler (PMT).

The PL signals were integrated by a boxcar and processed by a personal computer which, in turn, controlled the spectrometer through a stepper motor connected to its parallel port. A Tektronix TDS1012 oscilloscope was used to acquire the decay kinetics of the PL. To improve the oscilloscope temporal resolution, a potentiometer, with resistance varying from 10 kΩ down to 50 Ω, was connected in parallel to the oscilloscope channel.

To measure the dephasing time of excitons in the GC-SNN, we used the DFWMIL technique described in details in the preceding section. Figure 3.6 shows a schematic representation of the experimental apparatus. The sample chosen was the one heat-treated for 206 h because it has the highest nonlinear susceptibility [Fa04]. As incoherent excitation source, we used a home-made dye laser (BBQ dye, concentration $2\text{x}10^{-3}$ M in a 1:1 toluene/ethanol solution) operating in the broadband mode i.e., without intracavity dispersive elements (such as diffraction gratings or prisms), transversally pumped by the third-harmonic (355 nm, 5 ns, 2 Hz) of the same Nd:YAG laser used in the PL experiments. The dye solution was continuously refluxed by a magnetic stirrer and the repetition rate of the laser was decreased to 2 Hz in order to avoid thermal degradation of the dye, since toluene slightly absorbs in 355 nm. Operating in this mode, amplified spontaneous emission (ASE) is generated and the light can be regarded as a complex Gaussian stochastic stationary process [Me01]. The laser radiation (ASE) was further amplified in two stages using dye solutions of the same concentration as the oscillator. The dye solution and its concentration were chosen to deliver ultraviolet light centered at $\lambda = 386$ nm (3.21 eV), near the band-gap of the $NaNbO_3$ nanocrystals (3.18 eV). The dye laser had pulse duration of 5 ns and spectral bandwidth $\Delta\lambda \approx 2.6$ nm, which corresponds to a coherence time $\tau_c \approx 170$ fs, calculated according to $\tau_c = 4\lambda^2 \ln 2 / c\pi\Delta\lambda$ [We09] [Ac89].

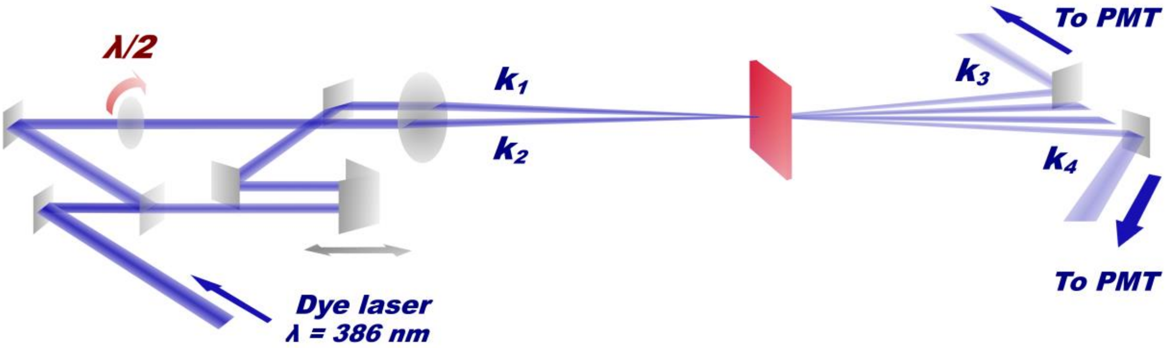

Fig. 3.6 – Schematic representation of the experimental apparatus used to measure $T_2$ in the GC-SNN.

The linearly polarized dye laser beam was then split, by a 50:50 beamsplitter, into two beams with wavevectors $\boldsymbol{k}_1$ and $\boldsymbol{k}_2$ respectively. These two beams follow the distinct arms of an interferometer-like setup, and the optical path of $\boldsymbol{k}_1$ beam could be changed by a computer-controlled delay line. The delay between the beams is $\tau > 0$ when $\boldsymbol{k}_1$ precedes $\boldsymbol{k}_2$ at the sample. The relative polarization between the $\boldsymbol{k}_1$ and $\boldsymbol{k}_2$ beams could be controlled by a $\lambda/2$ plate, positioned in the optical path of the $\boldsymbol{k}_2$ beam, to avoid the formation of a thermal grating. The beams are then focused by 20 cm focal length lens crossing in a small angle ≈ 0.6º. The phase-matched beams generated in the $\boldsymbol{k}_3 = 2\boldsymbol{k}_2 - \boldsymbol{k}_1$ and $\boldsymbol{k}_4 = 2\boldsymbol{k}_1 - \boldsymbol{k}_2$ directions were then collected by multimode optical fibers and guided to 1P28A PMTs. The electric signals were sent to the different channels of a boxcar averager and then processed by a personal computer.

### 3.2.3 Results and discussion

The linear absorption spectra of the samples with $f = 0.00$ and $f = 0.37$ are shown in Fig. 3.7 at different temperatures (the linear absorption spectra for other samples with differents $f$ can be found in chapter 5, fig. 5.3). The samples present a large transparency window extending from the blue to the near infrared, which indicates that the amount of in-gap states is small as well the scattering due to the nanocrystals is negligible. The energy band-gap $E_g$ of the samples were calculated according to the Tauc formula for a direct transition [Fo01]

$$\alpha_0^2(\omega) \propto (\hbar\omega - E_g), \tag{3.13}$$

where $\alpha_0$ is the linear absorption coefficient, $2\pi\hbar$ is the Planck's constant and $\hbar\omega$ is the photon energy. The calculated band-gaps at several temperatures for the samples with $f = 0.00$

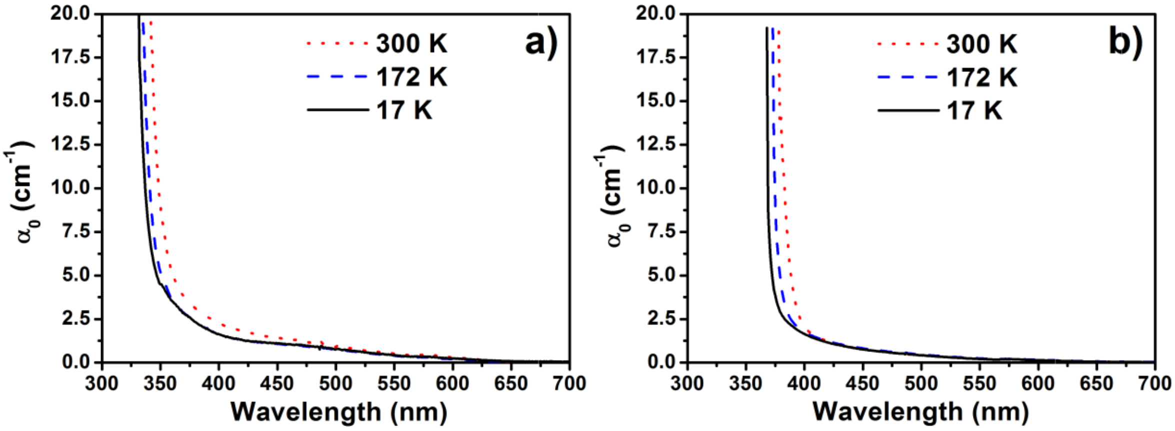

Fig. 3.7 – Absorption spectra at different temperatures of the GC-SNN with $f = 0.00$ (a) and $f = 0.37$ (b).

and *f* = 0.37 are shown in Fig. 3.8. The energy band-gap increases at lower temperatures, probably due to temperature-induced compression of the sample.

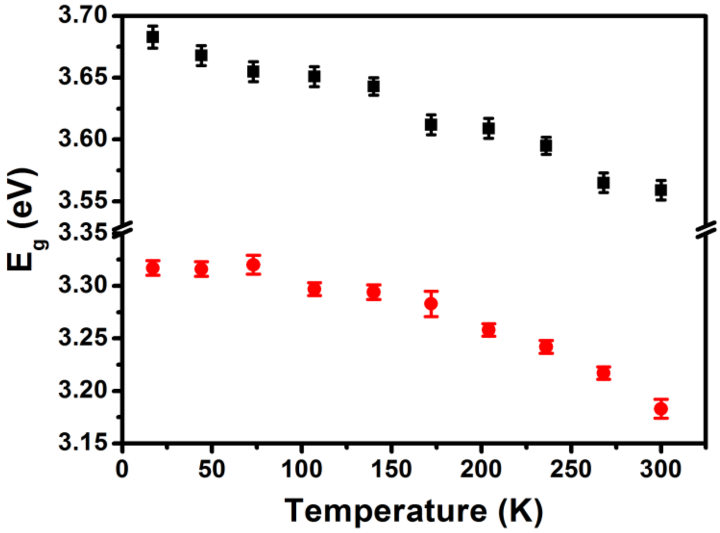

Fig 3.8 – Calculated band-gap at different temperatures of the GC-SNN with *f* = 0 (black squares) and *f* = 0.37 (red circles).

The PL spectra of the samples are shown in Fig. 3.9. The two PL bands centered at ≈ 430 nm and ≈ 540 nm are attributed to emissions originated from the $NaNbO_3$ nanocrystals, because these bands are not present in the PL spectra of the bare glass (*f* = 0.00). The band at ≈ 430 nm (2.87 eV) is attributed to direct exciton recombination, while the PL band at ≈ 540 nm (2.29 eV) is attributed to trap-states (due to dangling bonds or defects) emission at the nanocrystals' surface, since this emission is broadband and has low quantum efficiency. Note that this band is

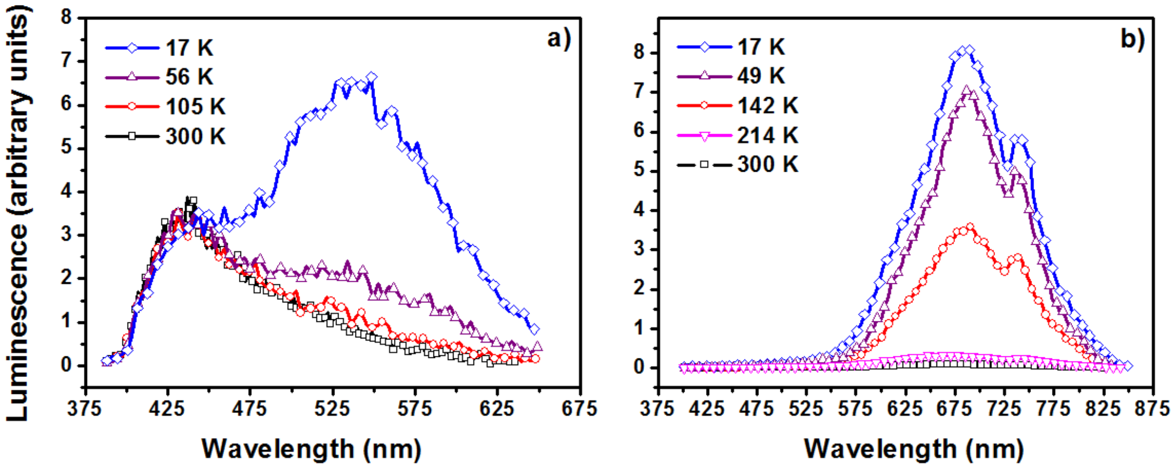

Fig. 3.9 – Photoluminescence spectra (excitation at 355 nm) at different temperatures of the GC-SNN with *f* = 0.37 (a) and *f* = 0.00 (b).

more intense at low temperatures, indicating that nonradiative relaxation is suppressed when the temperature is lowered, which is characteristic from trap-states emission.

The PL band centered at ≈ 680 nm (1.82 eV) (Fig. 3.9b), which is present only in the sample with *f* = 0.00, is attributed mainly to the presence of nonbridging oxygen hole centers (NBOHC) [Sk92] [Va08] [Va07]. This defect is represented by ≡SiO*, where ≡ stands for three bonded oxygens and the symbol (*) stands for an unpaired electron. The NBOHC are often present in multicomponent glasses [Sk05] and is reported to have a weak absorption band in the visible at 2.0 eV and strong absorption bands in the ultraviolet at 4.8 eV (with FWHM 1.05 eV) and 6.1 eV [Va08]. The PL band is centered at 1.9 eV for the NBOHC induced by neutron, gamma, X-ray or UV radiation in silica [Sk92]. As observed for the band originated from the trap states emission at the nanocrystals' surface, the nonradiative relaxation processes dominate the decay kinetics of the NBOHC emission [Sk92] [Va07]. However, we cannot exclude possible emission of amorphous CdO clusters, whose band gap is 2.07 eV. This possibility was further investigated in an independent experiment, in which we excited the samples at 575 nm (2.15 eV), off-resonance with the nanocrystals' transitions. The PL spectrum is shown in Fig. 3.10. At this excitation wavelength, the CdO and NBOHC absorption bands overlap and it is not possible to separate both contributions. Nevertheless, the PL spectrum resembles the one presented in [Zo99], in which the PL of CdO is investigated.

The decay kinetics of the PL band centered at 540 nm, excited at 355 nm, for the sample with *f* = 0.37 is shown in Fig. 3.11. The PL present a relatively fast decay < 25 ns followed by a slower

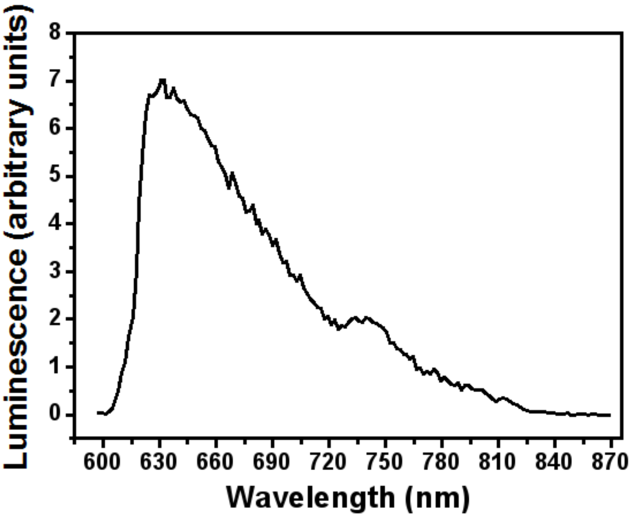

Fig. 3.10 – Photoluminescence (at T = 300 K) of the GC-SNN with *f* = 0 excited at 575 nm.

decay ≈ 500 ns for temperatures smaller than 60 K. This slow decay is attributed to long-living in-gap states (at the nanocrystals' surface), while the fast decay is attributed to excitonic recombination. The temporal resolution of the experiment is limited by the impulsive response of the detection system and is given by the excitation pulse plotted in Fig. 3.11 (green circles).

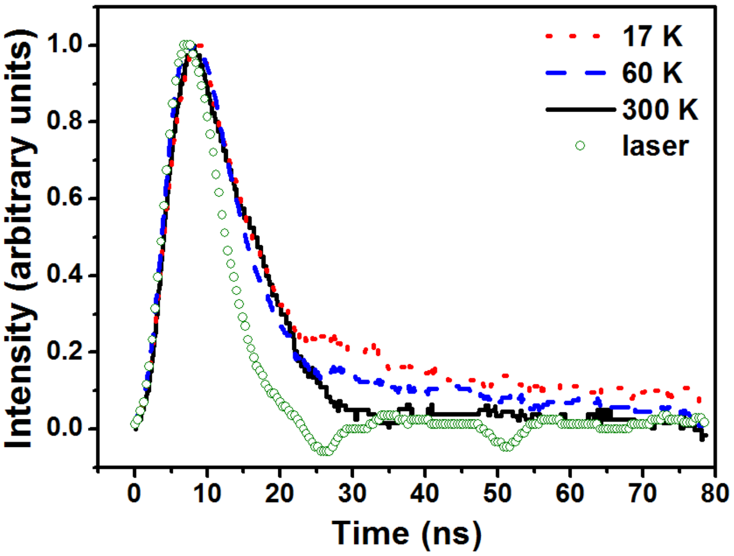

Fig. 3.11 – Decay kinetics of the luminescence at 525 nm (excitation at 355 nm) at different temperatures of the GC-SNN with $f = 0.37$. The curve represented by green circles is the response of the detection system to elastically scattered laser light.

The result for the intensity profile of the $\boldsymbol{k}_3 = 2\boldsymbol{k}_2 - \boldsymbol{k}_1$ and $\boldsymbol{k}_4 = 2\boldsymbol{k}_1 - \boldsymbol{k}_2$ beams generated in the DFWMIL experiment in the sample with $f = 0.37$ are shown in Fig. 3.12. Five laser shots were averaged for each point in the graph. The sample with $f = 0$ does not generate self-diffracted beams under the present intensity conditions since the photon energy of the laser (3.21 eV) is smaller than energy band-gap of the matrix (3.57 eV). As the signals profile were independent of the relative polarization between the exciting beams, indicating that thermal effects were negligible, the measurements were made using parallel polarization to obtain a better signal-to-noise ratio. The absence of pronounced tails in the signals' profile indicate that the dephasing time $T_2$ is smaller than the correlation time of the light $\tau_c \approx 170$ fs. To extract $T_2$, we fitted the signals' profile using Gaussian functions and calculated the separation $\tau_s = 20$ fs between their centers. Although the width of the signals is related to the correlation time $\tau_c$ of the light, it is the peak separation $\tau_s$ that determines $T_2$. Therefore subpulse width dephasing times can be extracted. The relation between $\tau_s$ and $T_2$ is given by eq. (3.10) and depends on the ratio between homogeneous and inhomogeneous broadening. We assume that inhomogeneous broadening is the dominating mechanism justified by the broad size and shape distribution of the $NaNbO_3$ nanocrystals. Therefore, $T_2$ is related to $\tau_s$ as one sees in Fig. 2.21 for which we obtain $T_2$ = (20 ± 6) fs, since we are in the linear region of Fig. 2.21 ($\tau_s/\tau_c \approx 0.12$). This dephasing time corresponds to a homogeneous linewidth $\Gamma = 2\hbar/T_2$ = (66 ± 20) meV. The error in the measurement of $T_2$ was estimated in another experiment by splitting one of the self-diffracted beams into two beams that were sent to the two different detection channels of the apparatus. The experiment was runned repeatedly and the maximum value of the peak separation under this condition was 3 fs, furnishing a error equal to 6 fs.

The homogeneous relaxation time can be expressed by

$$\frac{1}{T_2} = \frac{1}{2T_1} + \sum_i \frac{1}{T_2^i} \tag{3.14}$$

where $T_1$ is the population relaxation time and $T_2^i$ takes into account the contribution of all dephasing mechanisms, which at first approximation can be assumed to contribute independently to the homogeneous linewidth. In what follows we will make a brief description of the main dephasing mechanisms in semiconductor nanostructures [Wo97]:

1) *carrier-carrier scattering* happens when the excitation intensities are high enough to create a density of excited carriers ≈ $10^{18}$/cm$^3$ or conversely, more than one electron-hole pair per nanocrystal with diameter larger than 12 nm [Be88] [Bi91] [Wo95]. It can be shown that, for optical density OD << 1, the density of excited carriers $\eta$ is given by:

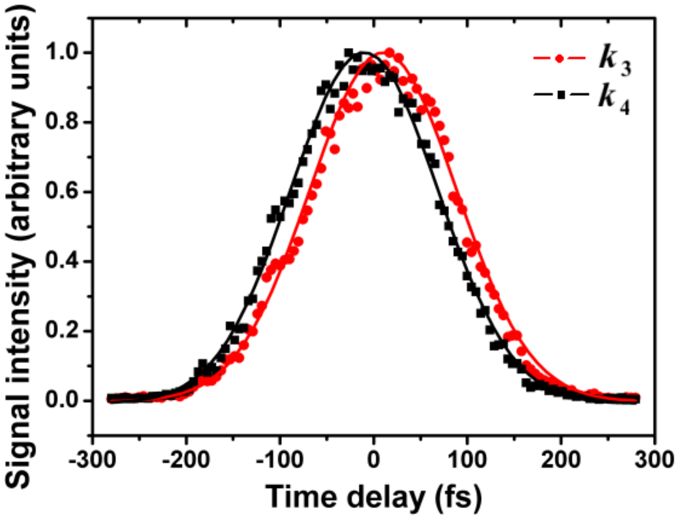

Fig. 3.12 – Phase-matched signals in the $\boldsymbol{k}_3 = 2\boldsymbol{k}_2 - \boldsymbol{k}_1$ (red circles) and $\boldsymbol{k}_4 = 2\boldsymbol{k}_1 - \boldsymbol{k}_2$ (black squares) directions. The Gaussian curves are the best fits to the experimental points. The separation between the peaks is $\tau_s$ = (20 ± 6) fs.

$$\eta = \frac{\alpha_0 \tau_p I_0}{\hbar\omega} \tag{3.15}$$

Using $\alpha_0$ = 10 $cm^{-1}$, $\tau_p$ = 5 ns, $\hbar\omega$ = 3.21 eV and $I_0$ = 11 $MW/cm^2$, the density of excited carriers in the sample with $f = 0.37$ is $\eta \approx 1.1 \times 10^{18}/cm^3$. Thus carrier-carrier scattering may be an important factor for the excitonic dephasing in the present measurement;

2) *carrier-phonon coupling* is a thermally-dependent process. When the thermal population is significant, as in the present case, the dephasing rate is increased due to interaction with a variety of acoustic phonons [Wo95]. We have tried to perform the measurements at lower temperatures. However, as the temperature decreases, the band-gap increases and we could not tune the central wavelength of the laser to the band-gap.

3) *carrier trapping on the nanocrystals' surface* is another factor that increases the dephasing rates and is a size-dependent mechanism [Mi94]. As it depends on the surface-to-volume ratio, the size dependence of the dephasing rate is expressed by $1/R$, where $R$ is the radius of the particle [Mi94]. An important parameter of this dephasing mechanism is the exciton Bohr radius $a_B$. When the size of the nanocrystals is smaller or comparable to $a_B$, the exctions' wavefunctions extend to the nanocrystals' surface, increasing the rate of electron trapping. Typically, the exciton Bohr radii of II-VI and III-V quantum dots are on the order of ≈ 10 nm, and decrease when the band-gap is larger. We have no information of this parameter for $NaNbO_3$, however for other oxides (as $LiNbO_3$) it has been estimated to be in the range from ~ 1 nm up to 20 nm [Yi04] [Mu01]. Therefore, we conclude that, in this case, the dephasing rate of these nanocrystals is enhanced due to fast capture of carriers in trap states at the nanocrystals' surface, whose presence was verified by the PL experiments.

Separating the individual contributions for the homogeneous dephasing is challenging and under the conditions of our experiments that was not possible. As the dephasing time is very short, we expect that all these mechanisms contribute altogether to the homogeneous linewidth.

## 3.3 Conclusions

In this chapter, we first presented the theoretical formalism of the DFWMIL technique and then applied to the investigation of exciton dephasing in a glass-ceramics containing sodium niobate nanocrystals. The goal of the experiments (including photoluminescence and DFWMIL) was to understand the contribution of trap states to the linear/nonlinear optical properties of the GC-SNN. Two important conclusions have emerged from the experiments reported in this chapter. First, the nonlinear optical experiments in this material in the visible range were affected by in-gap states associated with NBOHC and trap-states at the nanoparticles' boundaries. For instance, the TPA coefficients measured in [Ol07] using nanosecond pulses might be enhanced by one-photon resonance with in-gap states. Second, the fast relaxation time of the induced nonlinear polarization ($T_2$ = 20 ± 6 fs) indicated that the nonlinear process exploited is essentially nonresonant and therefore demonstrated the possibility of ultrafast optical switching of this material in the blue region.

# 4. Ultrafast Surface Plasmons Dynamics in Colloidal Silver Nanoparticles

This chapter reports measurement of localized surface plasmons dephasing times in colloidal silver nanoparticles stabilized with different capping agents using the persistent spectral hole-burning (PSHB) technique. The results are complemented by *ab initio* calculations for the interaction between the silver nanoparticles and the capping agents. The chapter starts with a review of the optical properties of noble metal nanoparticles and the localized surface plasmon resonance, which dominates the optical properties of noble metal nanoparticles in the visible spectrum. After that, the dephasing mechanisms of the localized surface plasmons are reviewed and the techniques for measuring the dephasing times are described, with emphasis on the PSHB technique. Finally, we present some of the original results of this thesis, which demonstrate that the stabilizer influence the localized surface plasmons dephasing dynamics in colloidal nanoparticles.

## 4.1 Optical properties of noble metal nanoparticles

The optical properties of noble metal nanoparticles in the visible are dominated by the localized surface plasmon (LSP) excitation, which is a collective oscillation of the electrons in the conduction band (the sp-band in noble metal nanoparticles) in response to an electromagnetic field. LSPs are the quanta of this collective oscillation. Not only the beautiful colors of metallic nanoparticles are consequence of the LSP excitation, but several interesting phenomena are consequence of this collective motion. These metallic nanoparticles have attracted the interest of researchers from several fields, specially in the last two decades, due to the inumerous applications, such as sensing [Wi07], photothermal cancer therapy [Lo05] [Di08], optical data storage [Zi09], photocatalysis [Ka02], light harvesting [Au10], plasmonic circuitry [Ma03] among others [Ma05]. Figure 4.1 shows a classical picture of the LSPs resonance, which can be represented as a displacement of the conduction electrons against the positive fixed core. The effect is a net negative surface charge that oscillates back and forth accompanying the electric field of light.

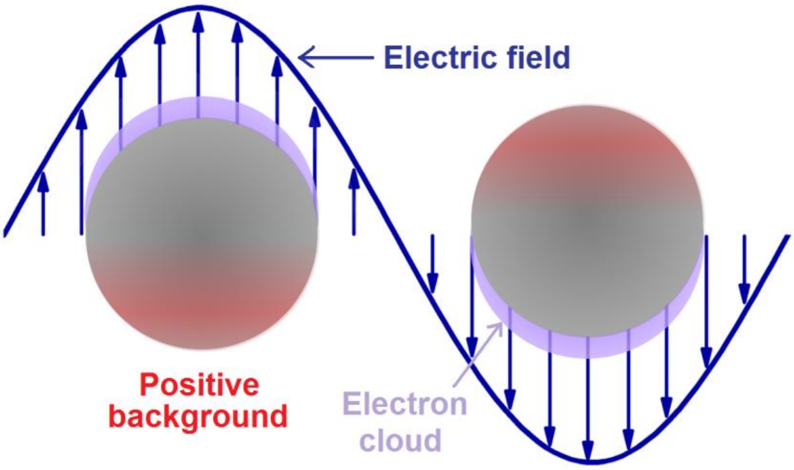

Fig. 4.1 – Classical representation of the localized surface plasmon resonance.

### 4.1.1 The Drude model

The optical properties of metals in response to an applied external field can be derived by the Drude model, which was originally applied to describe DC conductivity in metals. In this model, the conduction electrons of a bulk metal can be treated as point-like particles moving independently in a positive background. The equation of motion for one of these electrons in the presence of an electromagnetic field is given by

$$m_e \frac{d^2 x}{dt^2} + m_e \Gamma_d \frac{dx}{dt} - e\boldsymbol{E}_0 \exp(-i\omega t) = 0\,, \tag{4.1}$$

where $m_e$ is the mass of the conduction electrons, $\Gamma_d$ is the damping constant, $e$ is the elementary charge and $\boldsymbol{E}_0 \exp(-i\omega t)$ is the applied external field which oscillates at a frequency $\omega$. The damping constant accounts for collision processes (such as scattering by phonons, impurities etc) and can be assumed to be $\Gamma_d = v_f / l_{free}$, where $v_f$ is the Fermi velocity and $l_{free}$ is the electron mean free path i.e., the mean distance traveled by an electron between consecutive collisions. The polarization can be derived by solving eq. (4.1) and multiplying by the density of electrons $\eta$. Therefore,

$$\boldsymbol{P} = -\frac{\eta e^2}{m_e} \frac{1}{\omega(\omega + i\Gamma_d)} \boldsymbol{E}\,. \tag{4.2}$$

Using the constitutive relation [eq. (2.5)], the frequency-dependent dielectric function is given by

$$\varepsilon(\omega) = 1 - \frac{\eta e^2 / m_e \varepsilon_0}{\omega(\omega + i\Gamma_d)} = 1 - \frac{\omega_p^2}{\omega^2 + \Gamma_d^2} + i\frac{\omega_p^2 \Gamma_d}{\omega(\omega^2 + \Gamma_d^2)}, \tag{4.3}$$

where $\varepsilon_0$ is the (vacuum) electrical permittivity and $\omega_p = \sqrt{\eta e^2 / m_e \varepsilon_0}$ is the plasma frequency. For noble metals such as gold and silver, the plasma frequency lies in the ultraviolet $\omega_p \approx 9$ eV [Kr95]. Figure 4.2 shows the dielectric constant of silver extracted from [Ed85] and the theoretical fits using eq. (4.3). The Drude model successfully describes the dielectric function in the near infrared and in part of the visible. However, it fails in the remaining part of the visible and ultraviolet, where interband transitions have to be taken into account. They can be added phenomenologically to eq. (4.3) through a frequency-dependent dielectric term $\varepsilon^{ib}(\omega)$:

$$\varepsilon(\omega) = \varepsilon^{ib}(\omega) + 1 - \frac{\omega_p^2}{\omega^2 + \Gamma_d^2} + i\frac{\omega_p^2 \Gamma_d}{\omega(\omega^2 + \Gamma_d^2)}. \tag{4.4}$$

The onset of interband transition is ≈ 2.4 eV and ≈ 3.9 eV for gold and silver, respectively [Kr95]. The dielectric function is complex, with real and imaginary components. Roughly speaking, the real part determines the position of the LSP resonance, while the imaginary part determines its width. When the electrons are confined in a structure smaller than $l_{free}$, such as a nanoparticle, surface collisions have to be considered and the dielectric function has to be modified via the damping constant $\Gamma_d(R)$, which for a spherical particle is given by

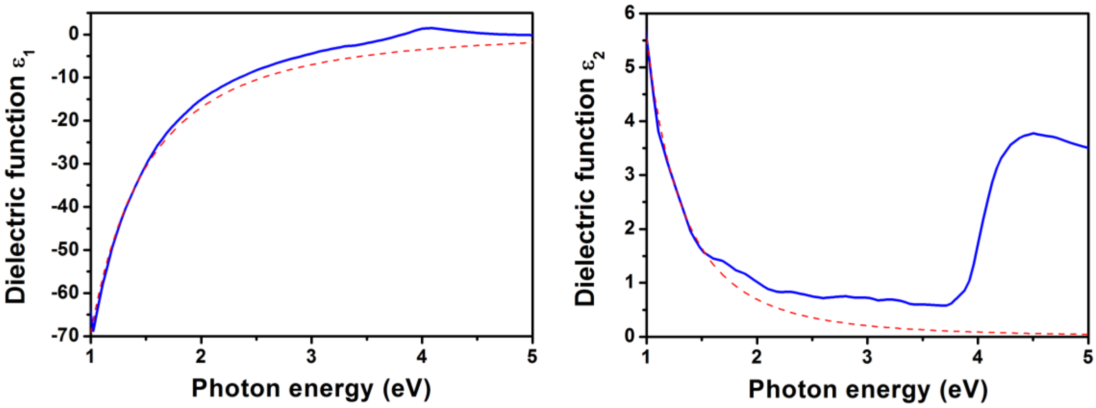

Fig. 4.2 – Real (left) and imaginary (right) components of the dielectric function of bulk silver extracted from Palik [Ed85]. The dashed lines represent the theoretical fits based on the Drude model.

$$\Gamma_d(R)=\Gamma_d+\frac{A}{2R}, \tag{4.5}$$

where $A$ is the damping parameter that depends on details of electron-surface interaction and $R$ is the radius of a spherical particle. The $1/R$ dependence of the damping constant is a consequence of the surface scattering probability dependence on the surface-to-volume ratio. Several studies have been addressed to investigate the damping parameter $A$, by changing the environment conditions to investigate how the optical properties of nanoparticles differ from those expected from bulk. We will describe the processes that determine this parameter in detail in the following sections.

### 4.1.2 The Mie theory

The first theoretical work intended to study the optical properties of metallic nanoparticles dates from 1908 by Gustav Mie. In a long article [Mi08], he applied the Maxwell's equations to a small homogenous (dielectric or metallic) sphere with radius $R$ embedded in a homogeneous environment. Due to the symmetry of the problem, he worked in spherical coordinates. The dielectric functions of the embedding medium and of the sphere enter as input parameters in his theory. The calculated extinction $\sigma_{ext}(\omega)$ and scattering $\sigma_{sca}(\omega)$ cross sections are expressed as [Bo83]

$$\sigma_{ext}(\omega)=\frac{2\pi}{|k|^2}\sum_{L=1}^{\infty}(2L+1)\mathrm{Re}\{a_L+b_L\}, \tag{4.6}$$

$$\sigma_{sca}(\omega)=\frac{2\pi}{|k|^2}\sum_{L=1}^{\infty}(2L+1)\left(|a_L|^2+|b_L|^2\right), \tag{4.7}$$

and the absorption cross section is given by

$$\sigma_{abs}(\omega)=\sigma_{ext}(\omega)-\sigma_{sca}(\omega), \tag{4.8}$$

where $|\boldsymbol{k}|=c/n_h\omega$ is the modulus of the wavevector of light propagating in a medium with refractive index $n_h$, $c$ is the speed of light in vacuum and $\omega$ is the frequency of light. The Mie coefficients $a_L$ and $b_L$ are given by

$$a_L=\frac{m\psi_L(mx)\psi_L'(x)-\psi_L'(mx)\psi_L(x)}{m\psi_L(mx)\xi_L'(x)-\psi_L'(mx)\xi_L(x)}, \tag{4.8}$$

$$b_L = \frac{\psi_L(mx)\psi'_L(x) - m\psi'_L(mx)\psi_L(x)}{\psi_L(mx)\xi'_L(x) - m\psi'_L(mx)\xi_L(x)}, \tag{4.9}$$

where $x = |\boldsymbol{k}|R$, $m = n_h / n_p$ ($n_p$ is the refractive index of the material of the particle), $\psi_L$ and $\xi_L$ are Bessel-Ricatti functions, while $\psi'_L$ and $\xi'_L$ are their derivatives with respect to $x$. The subscript *L* describes the order of the excitation in the particle. *L* = 1 is the dipolar contribution, *L* = 2 is the quadrupolar, *L* = 3 is the hexapolar and so on. The order of excitation depends on the size of the nanoparticle and, for small particles, eqs. (4.6)-(4.7) can be evaluated retaining only a few terms.

### 4.1.3 The quasi-static approximation and the electric field enhancement

The simplest approximation for the Mie scattering parameters is the quasi-static approximation, where only the first (dipolar) term is retained. The situation is depicted in Fig. 4.3. For nanoparticles much smaller than the wavelength of light, the electric field of the light can be assumed to be spatially homogeneous over the sphere. The dipolar terms are given by [Bo83]

$$\sigma_{abs} = 12\pi \frac{\omega}{c} \varepsilon_h^{3/2}(\omega) R^3 \frac{\varepsilon_2(\omega)}{[\varepsilon_1(\omega) + 2\varepsilon_h(\omega)]^2 + \varepsilon_2(\omega)^2}, \tag{4.10}$$

$$\sigma_{sca} = \frac{8}{3}\pi \left(\frac{\omega}{c}\right)^4 \varepsilon_h^2 R^6 \frac{[\varepsilon_1(\omega) - \varepsilon_h(\omega)]^2 + \varepsilon_2(\omega)^2}{[\varepsilon_1(\omega) + 2\varepsilon_h(\omega)]^2 + \varepsilon_2(\omega)^2}, \tag{4.11}$$

where $\varepsilon_h(\omega)$ is the dielectric function of the embedding medium and $\varepsilon_1(\omega)$ [$\varepsilon_2(\omega)$] is the real [imaginary] part of the dielectric function of the metal ($\varepsilon = \varepsilon_1 + i\varepsilon_2$). The extinction cross-section shows a resonance when $\varepsilon_1(\omega) = -2\varepsilon_h(\omega)$. As stated previously, the real part is related to the resonance frequency of the LSPs while the imaginary part is related to the resonance width. In the quasi-static approximation, the absorptive term dominates the extinction spectrum, since the absorption cross section depends on $R^3$, while the scattering scales with $R^6$. Scattering only starts to contribute to the extinction when the size of the nanoparticles is larger than 20 nm. Equations (4.10)-(4.11) can be found in a simpler manner solving the Laplace equation for the electric potential of a sphere, embedded in a dielectric medium, subjected to an uniform electric field [Bo83] [Ma07]. The electric fields calculated in this classical problem are given by [Ma07]

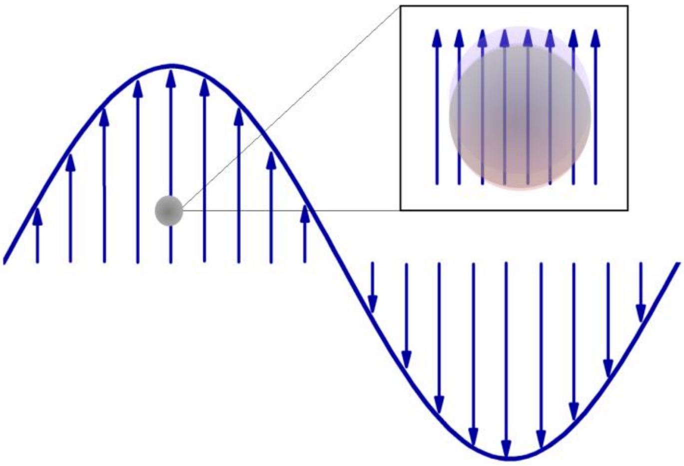

Fig. 4.3 – LSP resonance in the quasi-static approximation. The electric field (zoomed region) can be assumed uniform over the spherical particle.

$$\boldsymbol{E}_{in} = \frac{3\varepsilon_h}{\varepsilon + 2\varepsilon_h}\boldsymbol{E}_0, \tag{4.12}$$

$$\boldsymbol{E}_{ext} = \boldsymbol{E}_0 + \frac{3\boldsymbol{n}(\boldsymbol{n}\cdot\boldsymbol{p}) - \boldsymbol{p}}{4\pi\varepsilon_0\varepsilon_h}\frac{1}{r^3}, \tag{4.13}$$

where $\boldsymbol{E}_0$ is the applied external field, $\boldsymbol{E}_{in}$ and $\boldsymbol{E}_{ext}$ are the electric fields inside and outside the sphere, respectively; $r$ is the distance between the point of observation and the center of the sphere, $\boldsymbol{n}$ is the unit vector pointing from the center of the sphere to the point of observation, and

$$\boldsymbol{p} = 4\pi\varepsilon_0\varepsilon_m R^3 \frac{\varepsilon - \varepsilon_h}{\varepsilon + 2\varepsilon_h}\boldsymbol{E}_0 \tag{4.14}$$

is the dipole moment induced inside the of sphere. The inner electrical field in a metallic sphere is nonzero and uniform (eq. 4.12) provided the dimensions of the particle are smaller than the *skin depth* of the metal, which is typically on the order of tens of nanometers at optical frequencies. Equations (4.12)-(4.14) show that the electric field is enhanced at the LSP resonance i.e., when $\varepsilon_1(\omega) = -2\varepsilon_h(\omega)$. This electric field enhancement is the basis of several applications such as fluorescence enhancement and surface enhance Raman spectroscopy

(SERS) [Wi07] where the single-molecule SERS signal can be increased up to 14 orders of magnitude [Kn97].[2]

### 4.1.4 The Gans theory – LSP resonance of an ellipsoid

Mie theory is the exact solution of Maxwell's equations for a homogeneous sphere. For an ellipsoid, the spherical symmetry is broken and the polarizability becomes anisotropic. The simplest example of an ellipsoid is a prolate rotational ellipsoid, which is generated by a revolution of an ellipse around its major axis (fig.4.4). The prolate rotational ellipsoid is characterized by the semiminor axis *a*, semimajor axis *b* and aspect ratio *a*/*b*. In the quasi-static approximation, the polarizabilities calculated for the different axis are given by [Bo83]

$$\alpha_{\perp} = \frac{4}{3}\pi a^2 b \frac{\varepsilon_1(\omega) - \varepsilon_h}{\varepsilon_h + L_a[\varepsilon_1(\omega) - \varepsilon_h]}, \tag{4.15}$$

$$\alpha_{\parallel} = \frac{4}{3}\pi a^2 b \frac{\varepsilon_1(\omega) - \varepsilon_h}{\varepsilon_h + L_b[\varepsilon_1(\omega) - \varepsilon_h]}, \tag{4.16}$$

where $\alpha_{\perp}$ and $\alpha_{\parallel}$ are the polarizabilities along *a* and *b* respectively, and the depolarization factors $L_i$ ($i$ = a, b) are defined as

$$L_b = \frac{1-e^2}{e^2}\left[\frac{1}{2e}\ln\left(\frac{1+e}{1-e}\right) - 1\right], \tag{4.17}$$

$$2L_a + L_b = 1, \tag{4.18}$$

where the eccentricity *e* is defined as

$$e^2 = 1 - \frac{a^2}{b^2}. \tag{4.19}$$

---

[2] From these 14 orders of magnitude of signal enhancement in the single-molecule SERS, two to three are believed to be originated from charge transfer between the metal and the molecule (chemical effect) [Do02].

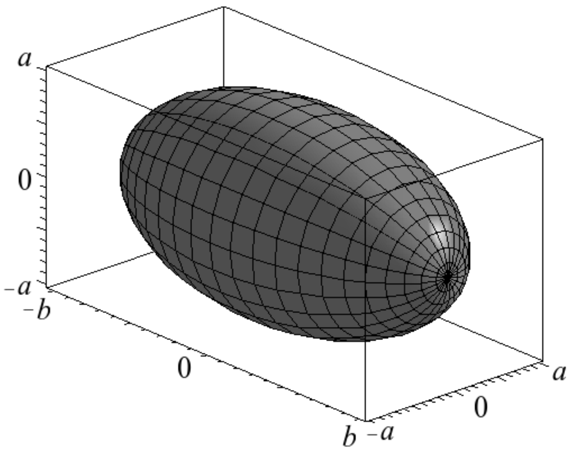

Fig. 4.4 – Prolate rotational ellipsoid with minor axis 2*a* and major axis 2*b*.

The LSP resonance splits into two modes, a longitudinal mode (with lower energy) oscillating along the major axis and a transversal mode oscillating along de minor axis (with higher energy). The resonance for the longitudinal mode occurs when $\varepsilon_h + L_b\left[\varepsilon_1(\omega) - \varepsilon_h\right] = 0$, which implies that the real part of the metal dielectric function must satisfy

$$\varepsilon_1(\Omega) = \varepsilon_h\left(1 - \frac{1}{L_b}\right) \tag{4.20}$$

If we assume that the dielectric constant of water is $\varepsilon_h = 1.78$ in the visible, and taking the dielectric function of silver from [Ed85], we obtain the LSP resonance energy as a function of the aspect ratio as shown in Fig. 4.5 for the lower-energy (longitudinal) mode. Therefore, the LSP resonance frequency depends on the aspect ratio and can extend up to the near-infrared for noble metal nanoellipsoids. For other shapes, different numerical methods have been developed, such as discrete dipole approximation (DDA) [Dr94], finite difference time domain (FDTD) [Ye66] and finite elements [Vo94]. The description of these methods is beyond the scope of this thesis and good references can be found in [Ke03] [No07] [Zh08] [Am11].

### 4.1.5 Dynamics of the LSPs excitation

The dynamics following the excitation of LSPs in metallic nanoparticles is very complex and its investigation is challenging for both experimentalists and theoreticians [Ha11b] [Li03a]. The sequence of events is represented in Fig. 4.6. The fastest event is the LSPs dephasing and occurs on a temporal scale faster than 20 fs. During this time, the coherently oscillating electrons lose their phase coherence and the memory of excitation is scrambled away. The time in which they

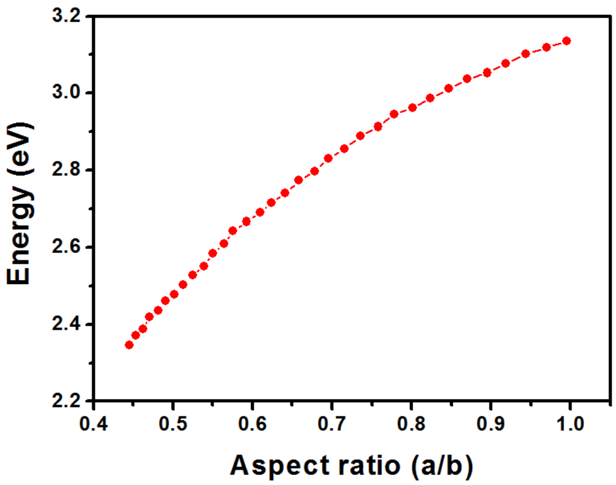

Fig. 4.5 – LSPR energy as a function of the aspect ratio of a prolate rotational ellipsoid.

lose their phase coherence i.e., the dephasing time $T_2$, is the subject of investigation in this chapter and the mechanisms of dephasing will be discussed in details in the next section.

The LSPs dephasing is accompanied by excitation of a non-thermal electron distribution where the empty levels in the conduction band now become populated. The electrons can be excited via either interband trasitions i.e., excitation of electrons from the d-band to the sp-band of the metal, or intraband trasitions, in which conduction electrons are excited. In this period, the electronic distribution is out of equilibrium and cools down via electron-electron scattering in ca. 100 fs [Fa92a] [Su94] [Fa92b]. The electron-electron scattering rate for larger nanoparticles is essentially the same as in bulk. However, for nanoparticles smaller than 5 nm, the scattering rate can be enhanced due to the reduction, induced by the surface, of Coulomb screening between conduction band and core electrons [Vo00] [Vo04].

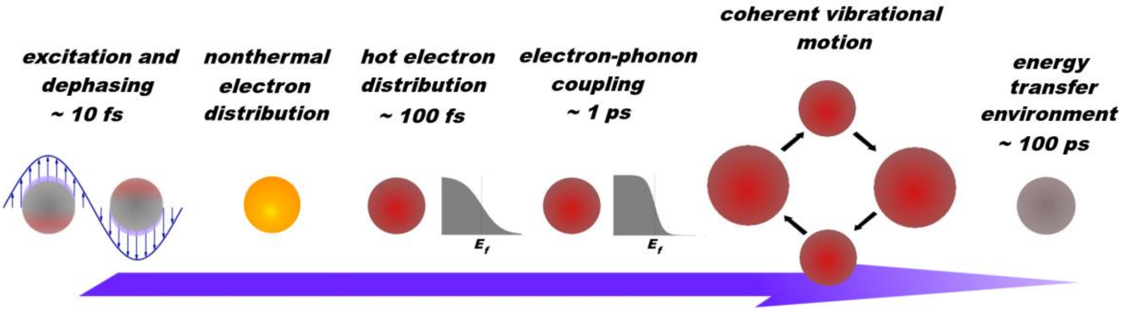

Fig. 4.6 Sequence of events following LSPs excitation.

The hot electron distribution then further cools down in a few picoseconds by exciting phonon modes in the particle. The coupling between the electrons and phonons can be described by the two-temperature model, for which the electronic and lattice temperature are treated separately and the rate of energy exchange between them depends on their temperature difference [Su94] [Ma04]. As the electronic specific heat is much smaller than the lattice one, a higher temperature of the electronic distribution gives rise to a much lower final equilibrated (electron-phonon) temperature. Electron-phonon energy redistribution has been studied by femtosecond pump-probe spectroscopy in bulk and small particles [Su94] [Ar03] [Li00]. As the case of electron-electron scattering, the particles behave similarly to the bulk except when they are smaller than 5 nm, when the electron-phonon scattering rate is changed [Ar03].

Under some conditions, because of the increase in the lattice temperature, some vibrational modes can be coherently excited, giving rise to characteristic mechanical oscillations [Vo01] [Ha06] [Ho98]. The period of the breathing modes is typically on the order of tens of picoseconds and depends on the nanoparticles' material, size, shape and environment. These oscillations are damped within tens to hundreds of picoseconds [Pe09]. As a consequence of lattice expansion, the electronic density at the particle is changed as well the LSP resonance frequency, making it suitable to be studied by femtosecond differential absorption spectroscopy. Recently, besides ensemble measurements of mechanical oscillation, single-particle measurements have been performed [St08] [Ha10]. In this case, the absorption changes are on the order of $10^{-5}$ and very stable lasers and precision electronics must be employed.

The final process is the energy transfer to the environment, which occurs in tens to hundreds of picoseconds and depends on the thermal conductivity of the environment as well as on the interface conductance which, in turn, depends on the surface passivation [Pl03] [Pl04] [Sc08]. Several experiments have been performed controlling the surface passivation through changes for examples, of stabilizing molecules [Al10b].

### 4.1.6 Dephasing mechanisms of LSPs

The fastest phenomena following the LSPs excitation is the plasmon dephasing, which occurs faster than 20 fs. The dephasing can occur via energy decay, expressed by the plasmon lifetime $T_{1,}$ or elastic collisions i.e., processes that change the electron momentum but conserve the energy, expressed by the *pure dephasing time* $T_2^*$. The contribution of the two processes implies

$$\frac{1}{T_2} = \frac{1}{2T_1} + \frac{1}{T_2^*} . \tag{4.21}$$

In the measurements reported up to now, the pure dephasing process is negligible compared to the energy decay of the LSPs, so that $T_2 = 2T_1$. The dephasing time is related to the width of the resonance by [Ma07]

$$\Gamma_{\text{hom}} = \frac{2\hbar}{T_2} , \tag{4.22}$$

and therefore measuring the homogeneous linewidth furnishes directly the dephasing time. In analogy with a resonator, the resonance quality factor is inversely proportional to the resonance linewidth and hence, directly proportional to the dephasing time. The measurement of $T_2$ is important for applications that demands local field enhancement since, according to this point of view, it is expected that the local field enhancement is proportional to $T_2$.

The homogenous linewidth can be computed directly from the bulk dielectric functions by [Kr95] [Kr76]

$$\Gamma_{\text{hom}}(\Omega) \approx \frac{2\hbar\varepsilon_2(\Omega)}{\sqrt{\left(\frac{d\varepsilon_1}{d\omega}\Big|_{\omega=\Omega}\right)^2 + \left(\frac{d\varepsilon_2}{d\omega}\Big|_{\omega=\Omega}\right)^2}} . \tag{4.23}$$

For particles with dimensions smaller than 20 nm, the dielectric functions deviate from the bulk values due to the electron collisions with the surface and eq. (4.19) must be properly corrected. The size dependence of the dephasing time for a spherical particle with radius $R$ is expressed as

$$\frac{1}{T_2} = \frac{1}{T_2^\infty} + \frac{A}{R} , \tag{4.24}$$

where $T_2^\infty$ is the dephasing time calculated via eq. (4.23) using the bulk dielectric functions; the damping parameter $A$ accounts for surface collisions and depends on the metal, shape and the environment [Kr95].

In principle, several mechanisms contribute altogether to the LSPs dephasing and, at first approximation, these processes can be considered independent of each other. The total dephasing rate of obeys the Mathiessen’s rule:

$$\frac{1}{T_2} = \sum_i \frac{1}{T_2^i} , \tag{4.25}$$

where each different dephasing mechanism contributes with a rate $1/T_2^i$ . The main mechanisms of LSPs dephasing are the following:

1) *Radiation damping* is the decay of the LSPs into photons. It is interpreted as the scattering of the incoming field. As the scattering cross section scales with the nanoparticle dimensions as $R^6$, this mechanism is observable only for particles larger than 20 nm [Sö01].

2) *Direct emission of electrons* happens at high intensities, when multiplasmons are excited and occurs on a femtosecond time scale [Ul98]. The plasmon can decay ionizing a non-thermal electron [Le00].

3) *Landau damping* is the decay of the LSPs into electron-hole pairs [Ya92]. The decay may occur via either intraband damping, when the electrons and holes are located in the same sp-band, or via interband damping i.e., the electrons and holes are located in different bands (Fig. 4.7). Landau damping has been ascribed as the dominating LSPs dephasing mechanism. Interband damping occurs when the LSPs energy is above the onset of interband transitions (≈ 2.3 eV for gold and ≈ 3.9 eV for silver). Sönnichsen *et al.* performed an interesting experiment measuring the linewidth of the LSP resonance of a gold nanorod via dark-field microscopy [Sö02a]. The plasmon resonance of a small gold nanosphere is ca. 2.3 eV.  If the nanorod aspect ratio is decreased, the plasmon resonance of the longitudinal mode is shifted to a lower energy. When the longitudinal mode resonance energy is below the onset of interband transitions, the linewidth is narrowed due to suppression of interband transitions and dephasing times up to 18 fs were measured [Sö02]. Landau damping can also be increased due to broadening of the electron-hole eigenstates induced by the surface.

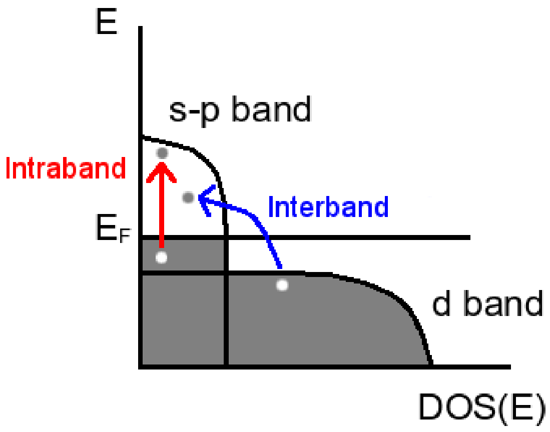

Fig. 4.7 – Representation of inter and intraband contributions to Landau damping of the LSPs. DOS(E) is the density of states with energy E and $E_F$ is the Fermi energy of the metal.

4) *Pure surface scattering* is the mechanism in which the oscillating electrons collide inelastically with the nanoparticles' surface [Pe93]. The rate of pure surface scattering depends on the surface-to-volume ratio.

5) *Chemical Interface Damping (CID)* is a surface-induced dephasing channel and it is defined as a dynamical electron tunneling from the nanoparticles to empty energy levels of the adsorbates and vice versa (Fig. 4.8) [Pe93] [Hö93] [Pi03]. It was modeled by Persson [Pe03] to describe the LSP resonance broadening of noble metal nanoparticles in different matrices due to adsorbed molecules: the adsorbate energy states strongly couple with the metal states, causing a broadening and shift of the adsorbate states to lower energy (the Newns-Anderson model [Ne69]). If the energy difference between the adsorbate induced resonance states and the Fermi level of the metal is smaller than the LSPs energy, the plasmon excitation can drive an electron transfer to empty levels associated to the adsorbates. The excited electron then returns back after some residence time (estimated to be typically tens of femtoseconds), returning out-of-phase compared to the remaining oscillating electrons. The CID rate depends on the coupling between the metal and the adsorbate: The closer the energy levels are, the shorter the dephasing time is. Not only electron transfer to adsorbate molecules is explained by CID, but also electron transfer in bulk substrates, such as quartz [Bo02].

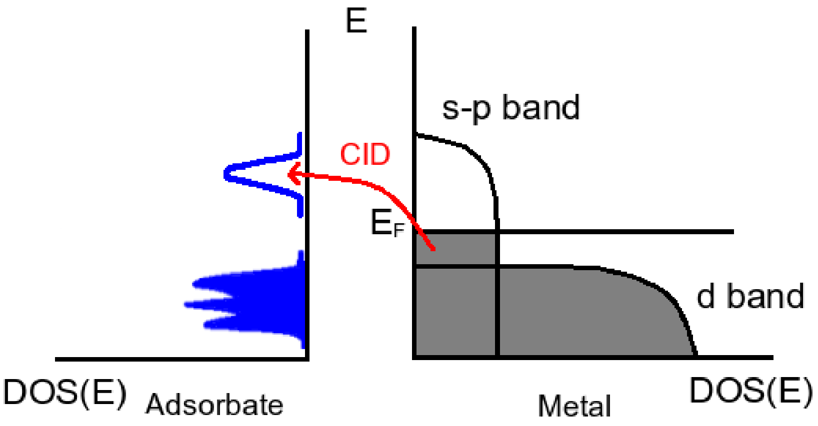

Fig. 4.8 – Representation of chemical interface damping in noble metal nanoparticles.

### 4.1.7 Techniques for measuring the dephasing of LSPs

Since the LSPs dephasing times in metallic clusters are faster than 20 fs, time-resolved techniques to measure $T_2$ require the use of few-cycle femtosecond pulses and photon-echo like experiments are not expected to be successful due to the low lifetime of the LSPs. The first experiments employed second harmonic generation (SHG) in the interferometric autocorrelation configuration in films of noncentrosymmetric metallic nanostructures [La97] [La99]. As the plasmon excitations (plasmon fields) in the particles generate second harmonic radiation, the measurement of this radiation via the autocorrelation of a pair of time-delayed pulses is a measurement of the autocorrelation of the plasmon fields created by these two pulses. This autocorrelation is broader than that of the incoming pulses in a nonlinear crystal, since the plasmon fields last longer than the driving fields. Dephasing times of 6 fs were measured using this technique. A drawback of this technique is that the autocorrelation traces are narrowed in an inhomogeneous ensemble [Va99]. To circumvent that, the technique was employed in single (large) particle measurement [Li01b]. Recently, a new version of the technique was applied using the interferometric frequency-resolved optical gating (IFROG) configuration, with the advantage of retrieval of the plasmon field phase and amplitude from the IFROG interferograms [An10].

The dephasing times can be extracted via frequency-domain techniques by measuring the LSP resonance linewidth $\Gamma_{\mathrm{hom}}$ and correlating it with $T_2$ via eq. (4.18). Most of these techniques employ single particle detection. The first single-particle frequency-resolved measurement employed scanning near-field microscopy (SNOM) in individual gold nanoparticles [Kl98], where dephasing times of 8 fs were measured. Dark-field microscopy [Sö02a] was later applied to investigate the position and linewidth of the LSP resonance in a variety of sizes and shapes of noble metal particles [Sö01] [Hu08]. One of the advantages of dark-field microscopy is that a simple white lamp can be used. As these two techniques rely on the scattered light from the plasmonic structures, only nanoparticles with dimensions larger than 20 nm can be studied. Furthermore, nanoparticle-substrate interaction alters $T_2$ and the LSP resonance energy [Kn09] [Ve10].

Besides scattering-based frequency-resolved techniques, absorption-based single-particle techniques have also been employed. Photothermal heterodyning imaging (PHI) [Be04] [Be06] is a pump-probe technique, where an intensity-modulated heating beam (pump) is absorbed by a single particle and the refractive index changes due to local temperature increase is probed via a frequency shift of the second beam. This allows measurements of the absorption cross-section of nanoparticles with sizes down to 2 nm. Another absorption-based technique, which allows measurements of the extinction cross-section of small particles, is called spatial light modulation spectroscopy (SLMS) [Mu08] [Ar04]. In this scheme, the substrate is spatially modulated and the extinction/absorption changes are detected by lock-in amplifier.

All these single-particle frequency-resolved techniques demands that the sample is fixed on a substrate, which obviously changes the nanoparticles optical properties, and limits systematic variation of the environment. A different technique applied to ensembles, called persistent spectral hole burning (PSHB), which allows control of the environment and selective elimination of inhomogeneous broadening, is employed in this thesis. To understand the details of the PSHB technique given in the next section, a discussion about laser-induced ablation and reshaping of the metal nanoparticles is instructive.

### 4.1.8 Laser-induced evaporation and reshaping of metallic nanoparticles

An interesting aspect of metallic nanoparticles is that, under relatively small incident laser fluences, the nanoparticles in resonance with the laser frequency can heat up and eventually melt or evaporate. This phenomenon was first demonstrated by excitation of gold nanoparticles with nanosecond laser pulses [Ta99]. In that work, nanoparticles with broad shape distribution were reshaped into spherical nanoparticles and, depending on the laser fluence, they evaporated to produce smaller particles.

A key point of the laser-induced melting process is the slow heat transfer to the environment, which typically occurs in hundreds of picoseconds [Pl04]. This implies that the laser fluences necessary to melt nanoparticles are higher for nanosecond pulses compared to femtosecond ones. In [Li99], the authors performed a pump-probe experiment in gold nanorods to investigate the time necessary for shape transformation of the nanorods. As they turn into spheres, the LSP resonance frequency is shifted to higher energies and this energy shift is easily detected in a femtosecond differential absorption experiment. The average time for the shape change is ~ 30 ps. More recent experiments employ pump-probe with femtosecond and X-ray pulses [Pl04] [Pl06], and ultrafast electron diffraction [Ru07]. The fluence threshold for nanoparticle melting in these experiments is ca. 15 mJ/cm$^2$.

Different nanoparticles have been synthesized using the laser-induced heating and ablation of nanoparticles, aiming to control the size of the nanoparticles, the solvent and stabilizing molecules [Go07] [Br10] [Py07], for example. This approach combines both bottom-up and top-down methods [Ou05] [Hu11].

The laser heating of nanoparticles has found application in cancer-killing therapies using gold nanoshell or nanorods whose LSP resonance is located in the near-infrared [Lo05] [Di08]. In these applications, high energy infrared CW lasers are used. Another promising application is multidimensional optical data storage, which use thermal reshaping of nanorods. As the nanorod extinction is polarization sensitive, this allows an extra dimension for optical recording [Zi09].

### 4.1.9 The persistent spectral hole-burning technique

Persistent spectral hole-burning (PSHB) for measuring LSPs dephasing times in metallic nanoparticles is an ensemble technique that has been applied to measure $T_2$ of noble metal nanoparticles of different sizes in a variety of environments [Bo02] [He03] [Hu10] [Hu07] [Zi04] . It was first demonstrated experimentally in [St00] and theoretically modeled in [Va01].

In principle, the homogeneous linewidth could be extracted from the linear absorption spectrum. However, the synthesized nanoparticles always have a size and shape dispersion, leading to an inhomogeneous broadening of the ensemble. As discussed in chapter 2, hole-burning is an ideal frequency-domain technique in these cases. The basic aspects of the PSHB technique are depicted in Fig. 4.9. First, noble metal nanoparticles are synthesized with different sizes and shapes, which gives rise to an inhomogeneously broadened absorption profile. In some synthesis, the shape of the nanoparticles can be approximated by a prolate rotational elipsoids, with an aspect ratio *a/b* where *a* and *b* are the semiminor and semimajor axes, respectively. The ellipsoid can be characterized by its equivalent radius $R_{\mathrm{eq}}$, which is defined as the radius of the sphere with the same volume as the ellipsoid. When $R_{\mathrm{eq}} \approx 10$ nm, the LSP resonance frequency depends on its aspect ratio, rather than on its size. The extinction spectrum $S_1(\omega)$ of the as-prepared nanoparticles is measured. The ensemble of nanoparticles is then irradiated by several pulses from a narrowband nanosecond laser with the optical frequency tuned to the LSPs band. The laser spectral linewidth must be much narrower than both the homogeneous and the inhomogeneous linewidths. The laser selectively excites a class of nanoparticles, defined by their aspect ratio, whose LSP resonance frequency is resonant with the laser beam. As we have seen in the subsection (4.1.8), for certain fluences the resonant nanoparticles are heated and eventually melt or evaporate with a subsequent change in their shape and size. As the overall number of nanoparticles resonant with the lasers diminishes due to the melting/evaporation process, a hole is burned in the spectrum. The new particles formed by the laser-induced heating process are more spherical and their LSP resonance is located at higher frequencies than the ellipsoid LSP resonance. As a consequence, a peak appears at higher frequencies, rendering the spectrum asymmetrical. After the laser irradiation process, a second

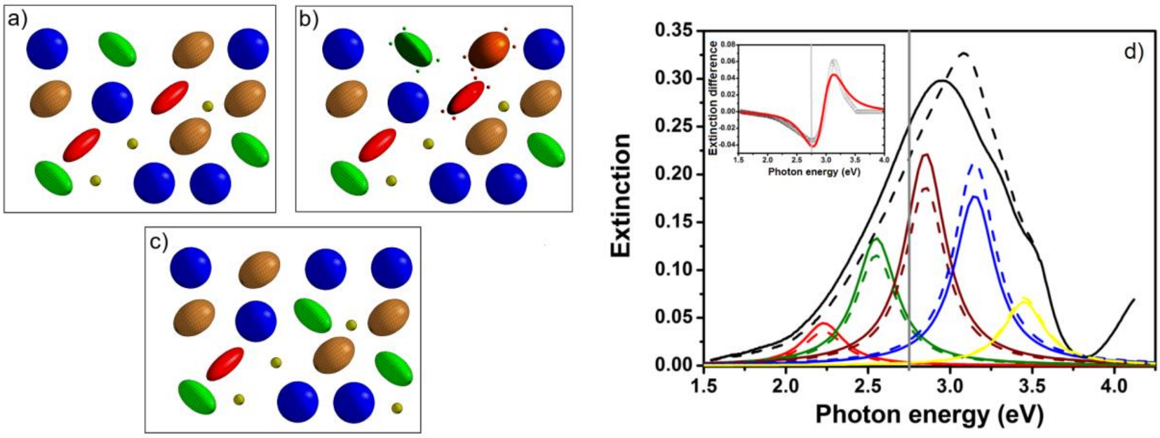

Fig. 4.9 – Scheme of the PSHB technique. a) as-prepared nanoparticles. The synthesized nanoparticles have a broad distribution of sizes and shapes, which gives rise to an inhomogeneous broadening, represented by the solid black line in the spectrum, and the corresponding spectra of homogeneously boadened particles (d). b) Nanoparticles irradiated by nanosecond laser pulses. The nanoparticles resonant with the laser heat and start to melt and evaporate, the atoms are preferentially released by the edges. c) modified nanoparticles and the corresponding total and individual spectrum (dashed lines). Inset) the difference spectra and the theoretical fit.

extinction spectrum $S_2(\omega)$ is measured and subtracted from $S_1(\omega)$. The laser-induced changes during this process can be modeled [Va01]. The extinction difference $\delta S(\omega) = S_2(\omega) - S_1(\omega)$ is given by

$$\delta S(\omega) = -\alpha \frac{(\gamma/2\hbar)^2}{(\omega-\Omega_0)^2 + (\gamma/2\hbar)^2} + \beta \frac{(\omega-\Omega_0)(\gamma/2\hbar)^3}{\left[(\omega-\Omega_0)^2 + (\gamma/2\hbar)^2\right]^2}, \tag{4.26}$$

where the even term proportional to $\alpha$ describes the contribution from shrinking of the nanoparticles, while the odd term proportional to $\beta$ accounts for shape changes (fig. 4.10); $\Omega_0$ is close to the laser fluence; $\gamma$ is the spectral hole width, which increases linearly on the laser fluence $F$ as

$$\gamma = \Gamma_{\mathrm{hom}} + cF, \tag{4.27}$$

where $c$ is a constant that depends on the environment and $\Gamma_{\mathrm{hom}}$ is the homogeneous linewidth. $\alpha$, $\beta$, $\Omega_0$ and $\gamma$ are the fitting parameters of the model.

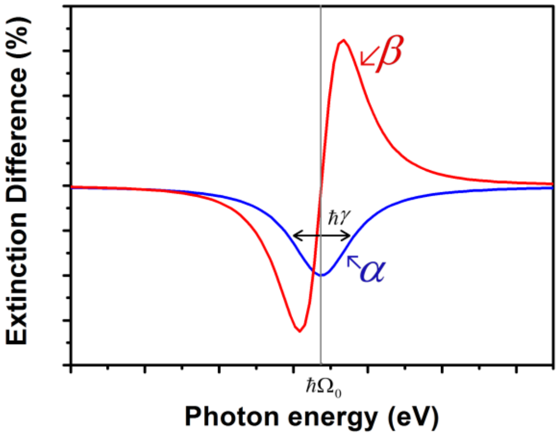

Fig. 4.10 – Representation of the parameters eq. (4.26) used in the PSHB model (see text). In the limit of the *quasi-static* approximation, unlike the shape changes, the size reduction does not affect the position of the resonance as represented by the blue Lorentzian curve.

The homogeneous linewidth, and hence $T_2$ [Eq. (4.22)], can be found by repeating the hole-burning processes at different fluences and extrapolating the hole spectral width, calculated from the experimental fits to eq. (4.26), to zero fluence in a graph that represents $\gamma$ as a function of $F$.

The fluence broadening of the burned hole is a signature of the fact that as the laser fluence increases, the particles that are not exactly resonant with the laser frequency start to contribute more effectively to the spectral hole. This power broadening also happens in conventional hole-burning [Vö89].

One of the differences between PSHB and conventional hole-burning is the fact that the reaction products (the new nanoparticles) still contribute to the spectral region of the original ensemble and this is explicitly taken into account in the model via the dispersive-like term proportional to $\beta$ (red curve in fig. 4.10).

## 4.2 Dephasing of LSPs in colloidal silver nanoparticles

After having reviewed the optical properties of metallic nanoparticles, discussed the dephasing mechanisms and the techniques for measuring $T_2$, we will now present some original results of this thesis. We focus on experimental and theoretical investigations of LSPs dephasing time changes for small colloidal silver nanoparticles when stabilized by different agents. Colloidal metallic nanoparticles need to be stabilized to avoid aggregation, and different capping agents have been used for this and other purposes (for example, biochemical sensing [Wi07], shape control [Lu09] and self-assembly [Li08]), but their effect on the local field enhancement, which is proportional to the plasmon dephasing time, has been often overlooked because $T_2 < 20$ fs, which is difficult to measure using time-resolved techniques. Furthermore, substrate-nanoparticle interaction in microscopy-based techniques also modifies $T_2$ [Ve10]. We apply the PSHB technique for measuring the dephasing times in colloidal silver nanoparticles stabilized with three different capping agents (trisodium citrate - TSC, Poly(vinylpyrrolidone) – PVP, and poly(vinylalcohol) – PVA). The experimental results are then complemented by *ab initio* calculations for the interaction among the nanoparticles and the capping agents.

### 4.2.1 Experiment

The colloidal nanoparticles were prepared by Dr. Antonio Marcos de Brito Silva during his Ph.D. program in the Materials Science Graduate program at Universidade Federal de Pernambuco, Brazil. The colloidal nanoparticles were synthesized by reducing silver nitrate ($AgNO_3$) with sodium borohydride ($NaBH_4$).

For the TSC-stabilized nanoparticles, a precursor solution was prepared by mixing equal volumes of $Na_3C_6H_5O_7$ (TSC) and $AgNO_3$ aqueous solutions at a concentration equal to 0.25 mmol/L (silver/citrate solution). Silver nanoparticles seeds were generated by adding 40 µL of $NaBH_4$ (10 mmol/L) to 5 mL of the silver/citrate solution in a test tube under 1500 rpm stirring for 30 sec. This procedure was repeated eight times to obtain 40 mL of the seed colloid. The growth of the particles was induced by adding 40 mL of the silver/citrate solution that was heated and kept under reflux for 1.5 hour. The resulting nanoparticle suspension was cooled down to the room temperature. Next, 40 mL of that suspension was mixed with 40 mL of the silver/citrate solution, re-heated until boiling and kept under reflux for 1.5 hour.

The PVP and PVA-stabilized silver nanoparticle followed a different procedure. PVP and PVA were purchased from Sigma-Aldrich and Vetec, respectively. A $4.7\text{x}10^{-2}$ mol/L $AgNO_3$ methanolic solution acted as the silver ion source in all experiments. PVP (0.25 g, 40,000 g/mol) and $NaBH_4$ ($2.9\text{x}10^{-4}$ mol/L) were dissolved in 250 mL of the liquid phase. The silver solution (1.4 mL) was added under strong stirring, heated and kept under reflux for 1.0 hour. The same procedure was done for the PVA-stabilized Ag nanoparticles.

The experimental apparatus for laser irradiation of the colloidal nanoparticles is depicted in fig. 4.11. As the light source, we used an optical parametric oscillator (OPO) (OPOTEK-Opolette 532 II) pumped by the second harmonic of a Nd:YAG laser. The OPO was tuned to 840 nm operating at repetition rate of 20 Hz. The pulse duration is 5 ns and the nominal spectral bandwidth of the pulse is in the range 4-20 $\text{cm}^{-1}$ (0.62-2.47 meV), which is much smaller than homogeneous linewidth of the LSP resonance (typically hundreds of meV [Kr95]). The light generated by the OPO was focused by a 10 mm focal length spherical lens into a nonlinear BiBO crystal (Castech, 1 mm long). The generated second harmonic radiation ($\lambda$ = 420 nm, $\hbar\omega_0$ = 2.94 eV) was collected by a 10 mm focal length cylindrical lens and filtered from the fundamental ($\lambda$ = 840 nm) beam, using a Corning 4-94 filter. The second harmonic then irradiated a 2 mm long quartz cuvette containing 100 μL of the colloidal NPs. The beam spot size incident on the sample was ≈ 2 mm x 65 μm. The laser fluences were set above 15 mJ/cm$^2$, where the NPs begin to melt and evaporate [Ru07] [Pl06]. To increase the beam-sample effective area of interaction, the cuvette was scanned transversally to the laser beam using a computer-controlled step motor, and was shot by 12,000 laser pulses.

Extinction spectra were taken using a CARY 5E Varian (UV-VIS-NIR) spectrophotometer. Before measuring the second extinction spectrum, the colloid in the cuvette was manually homogenized.

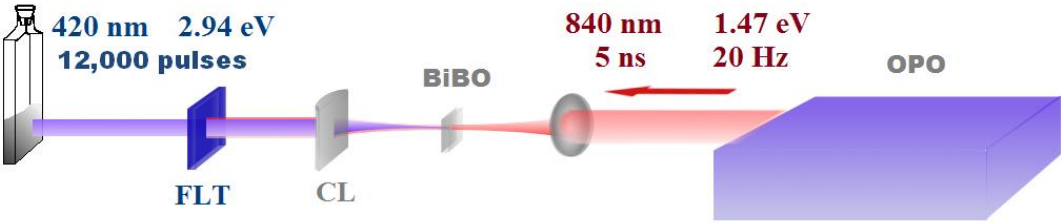

Fig. 4.11 – Simplified experimental scheme employed in the PSHB of the silver colloids. CL – Cylindrical lens, FLT – Filter.

### 4.2.2 DFT calculations

To further understand the mechanisms of LSPs dephasing induced by capping agents, we performed calculations based on the Density Functional Theory (DFT) for the electronic interaction between the silver nanoparticles and the stabilizing agents. A discussion of DFT is beyond the scope of this thesis and excellent references on the subject can be found in [Pa95] [Ko01] [Sz96]. The calculations, which were done by Dr. Augusto C. L. Moreira during his Ph.D. work at Physics Department–Universidade Federal de Pernambuco/Brazil, were carried out using the GAUSSIAN 03 software [Fr04]. The initial geometry was obtained as follows: First, the isolated stabilizing molecular structures were optimized at the Hartree-Fock level using the 6-31 Gaussian basis set for all atoms. Next, each optimized molecule was set above an ideal symmetric silver cluster containing 23 atoms. The crystalline plane orientation was (111) and the distance between the neighboring Ag atoms was set equal to the bulk distance (2.89 Å). Following the experimental results in [Hu96] [Li03c] [Le83] that shows that the oxygen atoms of the TSC, PVP and PVA molecules bind to the silver surfaces, we assumed that these atoms are the closest ones to the clusters. Starting with this unoptimized configuration, the system (molecule + Ag cluster) was optimized at the DFT level using the B3LYP hybrid functional basis set with LANL2MB for all atoms [Ja08]. With the optimized geometry, a single point calculation i.e, frozen geometry calculation, was performed with the B3LYP functional using the basis set LANL2DZ for the silver atoms and 6-31G (d,p) for the stabilizers' atoms.

Although in the calculations the system geometry is very small compared to the real NPs we have investigated, it is well established that the metal/molecule interaction is local. Therefore, in a theoretical approach, a unit cell composed of few atoms is often used to mimic the effective interaction region [Gr00] [So05] [He07] [Le10].

### 4.2.3 Results and discussion

A) PSHB in silver colloids

Figure 4.12 shows representative transmission electron microscopy (TEM) images of the colloidal silver nanoparticles stabilized with TSC, PVP and PVA. Based on these images, the nanoparticles shapes are approximated by prolate rotational ellipsoids. Part of the TSC-stabilized nanoparticles (~ 12 %) is flat and these were excluded from statistics. However, they also present plasmonic resonances that contributed to spectrum in the region investigated. The clustering seen in the TEM images of the TSC stabilized colloids is the result of the drying process in the sample preparation for TEM analysis. When in colloidal solution, the citrate anions impair a surface charge that repels other charged nanoparticles (electrostatic stabilization) [Na08]. Our colloids do not present any spectral indication of clustering, such as enhanced light scattering and spectral band asymmetries. The histograms of the equivalent radius and aspect ratio distribution of the colloids are shown in fig. 4.13 assuming that they are rotational ellipsoids. The nanoparticles with different capping molecules have approximately the same equivalent radius ~ 6 nm and, in this case, the quasi-static approximation is valid.

Figure 4.14 allows a comparison of the TSC-stabilized nanoparticles before and after irradiation by a laser fluence of 58 mJ/cm$^2$. The photon energy of 2.94 eV excites nanoparticles with aspect ratio $a/b$ = 0.78, according to the calculations in fig. 4.5. In the aspect ratio histogram after laser irradiation, the overall number of nanoparticles with $a/b \approx 0.75$ decreases while the relative number of the nanoparticles with $a/b > 0.8$ increases. From analysis of other TEM images, we could see the presence of spherical nanoparticles not present in the as-prepared colloid. We consider that these particles are formed by melting of non-spherical particles. Furthermore, smaller particles, formed by evaporation of the excited particles, were observed in the post hole-burning TEM images.

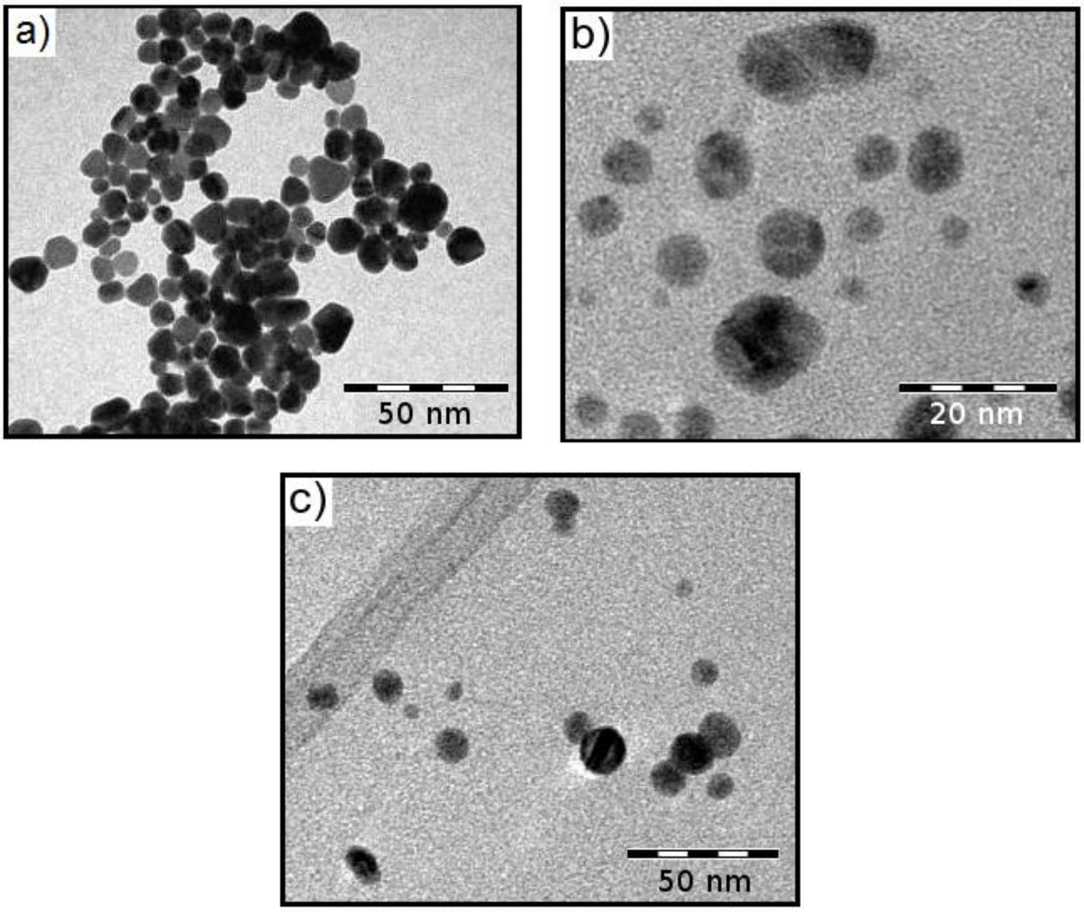

Fig. 4.12 – TEM images of the silver nanoparticles stabilized with TSC (a), PVP (b), and PVA (c).

The extinction spectra of the three different colloids before and after laser irradiation at different fluences, as well as the difference spectra $\delta S(\omega) = S_2(\omega) - S_1(\omega)$ and the best fits to eq. (4.26) are shown in fig. 4.15. For the fitting procedure, we used the Levenberg-Marquardt algorithm [Pr07] to minimize $\chi^2$. To help faster convergence of the fitting, the initial set of parameters in all fits was $\alpha = \beta = 1$, $\gamma = 0.5$ eV and $\hbar\Omega_0 = 2.94$ eV. The maximum standard error of $\gamma$ in the fitted curves was 12 meV. Clearly one can see in Fig. 4.15 that the widths of the holes changes with the stabilizer, and the hole is wider for PVA-capped nanoparticles.

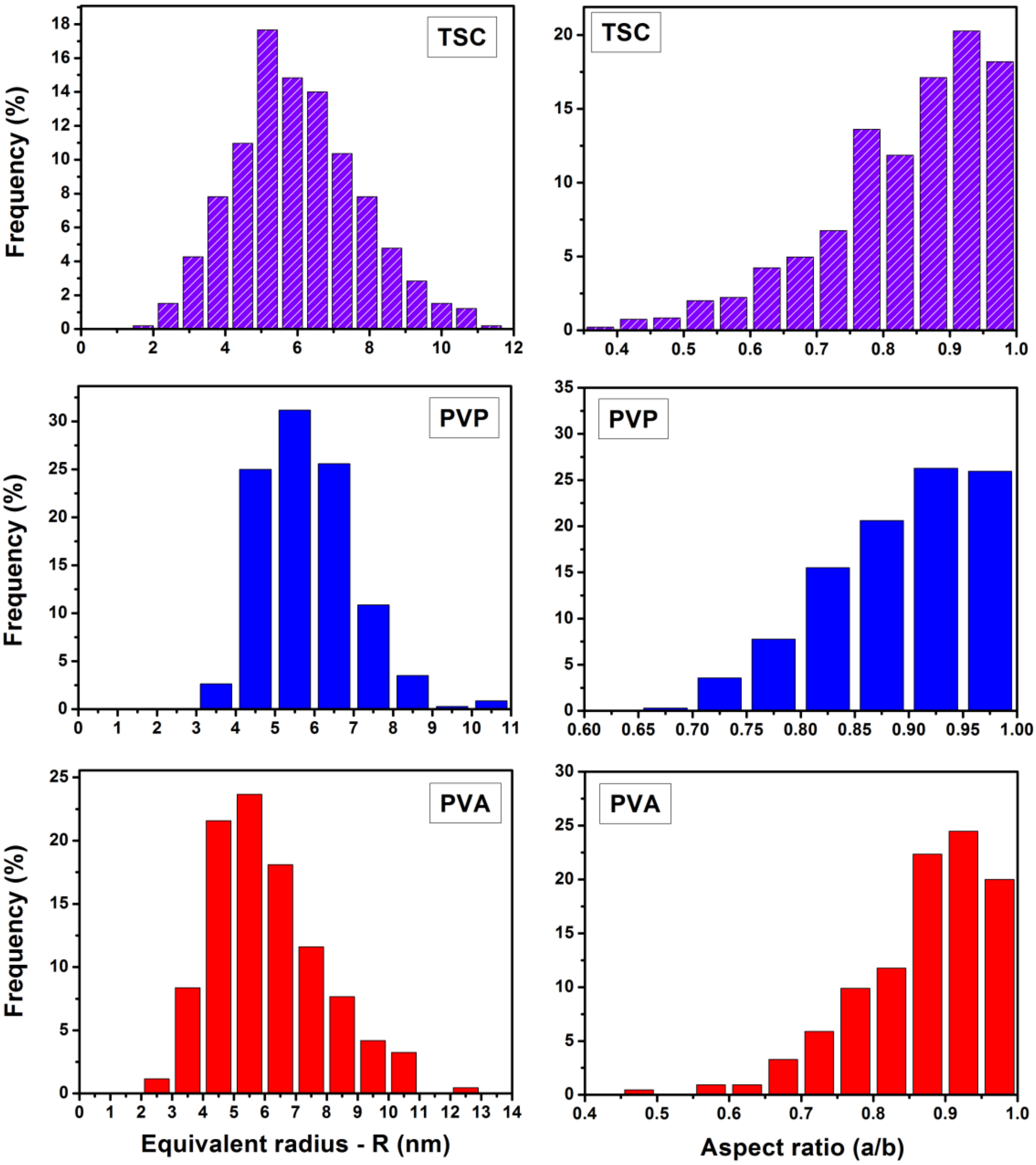

Fig. 4.13 – Histograms of the equivalent radius and aspect ratio of the nanoparticles capped with TSC, PVP and PVA.

The results for the holes' widths extracted from the fitting procedure in a set of different laser fluences are shown in fig. 4.16. To define the error bars, starting from the best fitted curves, we fixed the hole width to a different value and monitored the behavior of the $\chi^2$ value of the new fitted curve. We observed that within a range ± 40 meV in the value of the hole width, the quality of the fitting was not severely affected. In this case, the value of $\chi^2$ changed ~ 3%. The power broadening of the burned hole allows extracting $\Gamma_{\text{hom}}$ by extrapolation of straight lines to $F = 0$. Following this procedure, the values of $\Gamma_{\text{hom}}$ were (450 ± 40), (580 ± 40), and (740 ± 40) meV for nanoparticles stabilized with TSC, PVP and PVA respectively. This correspond to $T_2$ equal to (3.0 ± 0.3), (2.3 ± 0.3), and (1.8 ± 0.3) fs, respectively.

Recent results of single-particle measurements [Mu08] show that the homogeneous linewidths of the LSP resonance in chemically prepared nanoparticles varies from particle to particle, probably due to variations in the surface density of stabilizers and/or multifaceted character of the nanoparticles. Based on this, and since we are performing ensemble measurements, it should be reminded that the dephasing times measured here represent average values.

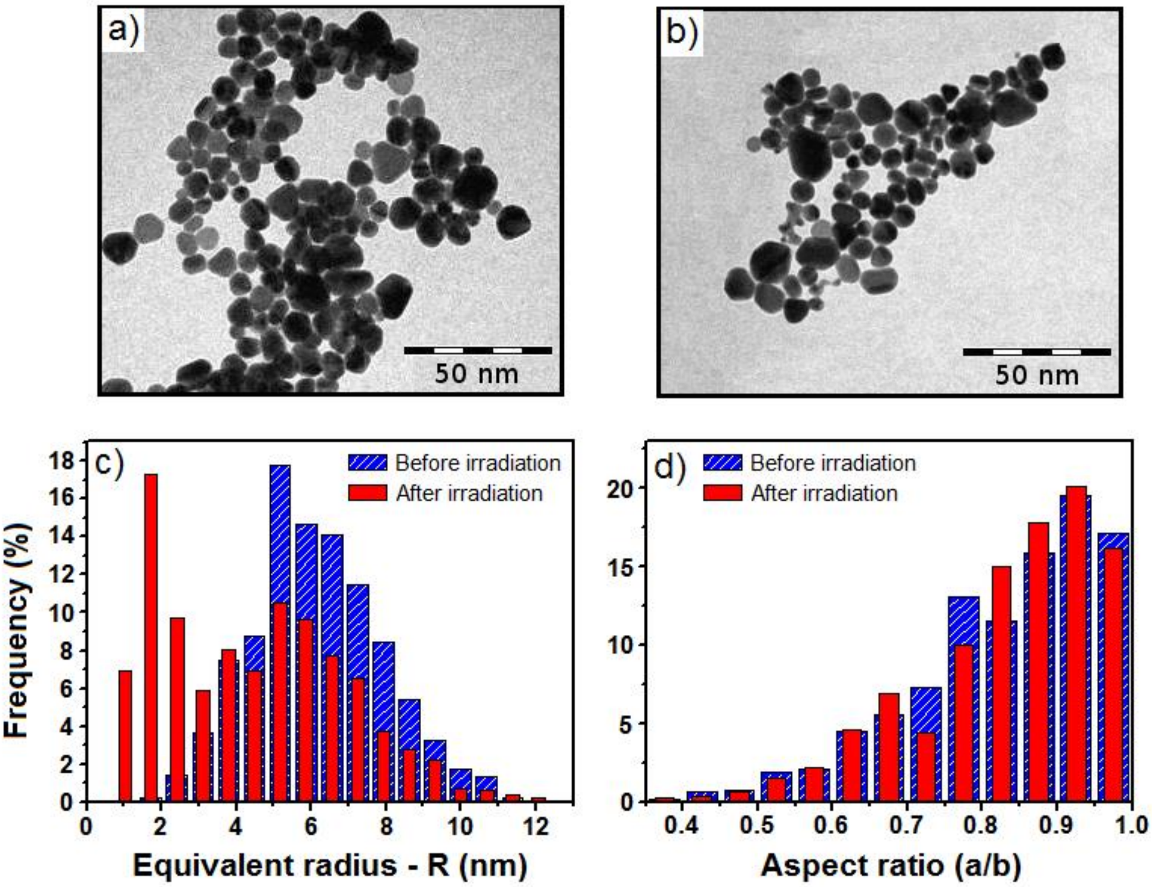

Fig. 4.14 – TEM images of the TSC-stabilized silver nanoparticles before (a) and after (b) laser irradiation. Histograms of the equivalent radius (c) and aspect ratio (d) before (cross-hatched blue bars) and after (solid red bars) laser irradiation.

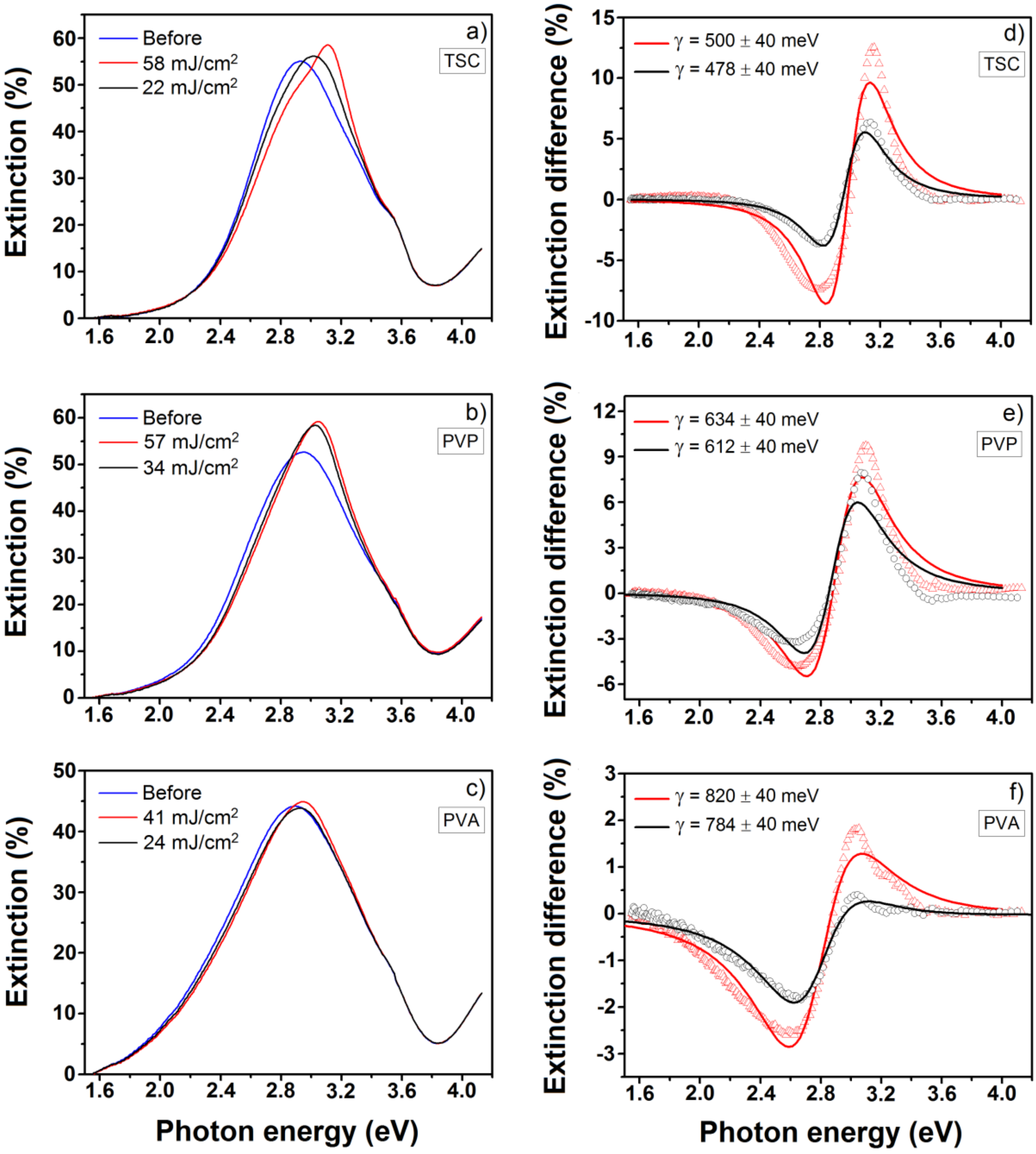

Fig. 4.15 – Extinction spectra (a)-(c) and difference spectra (d)-(f) along with the best fits for the silver nanoparticles stabilized with TSC (a) and (d), PVP (b) and (e), PVA (c) and (f).

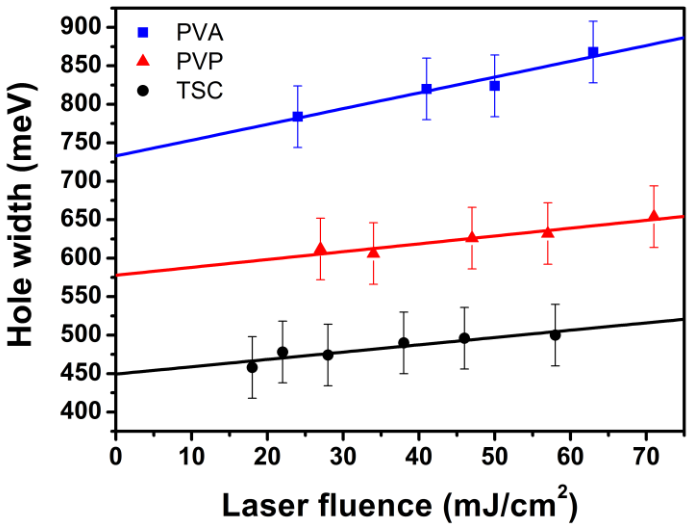

Fig. 4.16 – Fluence broadening of the PSHB for TSC (black circle), PVP (red triangles) and PVA (blue squares)-stabilized colloids. The homogenenous linewidth and hence the dephasing time is extracted extrapolating the linear fits to fluence $F = 0$.

Comparing the results presented in fig. 4.16 to the value of the dephasing time $T_2^{\infty} = 6$ fs, calculated from eq. (4.23) using the bulk values of the silver dielectric function (Fig. 4.2), we find that the dephasing times measured here are substantially shorter. They are also shorter than the dephasing times measured for silver nanoparticles with similar size at ultrahigh vacuum (UHV) conditions using PSHB [Bo02]. To allow further comparison with the results already found in the literature for particles with different sizes, it is mandatory to calculate the size-independent damping parameter $A$ according to eq. (4.24). Usually, $A$ is determined by measuring $T_2$ for different set of sizes and fitting the results to eq. (4.24). However, if $T_2^{\infty}$ is known, the damping parameter can be calculated using the $T_2$ measured for a single size of nanoparticles. For the nanoparticles with equivalent radius $R_{eq} = 6$ nm, the damping parameters are $A = (1.0 \pm 0.2)$, $(1.5 \pm 0.3)$, and $(2.4 \pm 0.6)$ nm/fs for TSC, PVP and PVA respectively. Table 4.1 shows some of the values of damping parameters of noble metal nanoparticles already reported. The damping parameters here significantly differ from that expected for pure surface scattering for silver nanoparticles in vacuum ($A_{surf} \sim 0.2$ nm/fs) [Pe93], which indicates that the chemical environment is leading to an additional LSPs damping.

As described earlier, the damping of the LSP resonance is a combination of several processes that at first approximation can be considered to contribute independently. Among these processes, we may exclude:

| **Reference** | **System** | **Nanoparticles' radius (nm)** | **Technique** | **Damping parameter *A* (nm/fs)** |
|---|---|---|---|---|
| **Baida *et al.* [Ba09]** | $Ag/SiO_2$ core/shell ellipsoids | 5-15 | SLMS | 0.5 |
| **Sönnichsen *et al.* [Sö02b]** | Silver spheres | ~ 20 | Dark-field | 0.42-1.46 |
| **Berclaud *et al.* [Be05]** | Gold spheres | 2-17 | PHI | 0.7 |
| **Hubenthal [Hu07]** | Aqueous gold ellipsoids | ~ 17 | PSHB | 2.7 |
| **Hubenthal *et al.* [Hu10]** | Gold ellipsoids supported on sapphire at UHV | 3-23 | PSHB | 0.3 |
| **Bosbach *et al.* [Bo02]** | Silver ellipsoids supported on quartz at UHV | 2-10 | PSHB | 0.4 |
| **Hubenthal and Träger [Hu11b]** | Silver ellipsoids supported on quartz/sapphire embedded in $SO_2$ | 10-15 | PSHB | 1.8 |
| **This work** | Aqueous silver ellipsoids capped with TSC/PVP/PVA | 6 | PSHB | 1.0-2.4 |

Table 4.1 – Comparison among the damping parameters *A* for different systems.

1) *Radiation damping* and *phase retardation effects*, since the synthesized nanoparticles are in the size regime where the quasi-static approximation is valid and;

2) *Interband damping* i.e, the LSPs decay into electron-hole pairs located in different bands, as the onset of interband transition (≈ 3.9 eV) [Kr95] is larger than the photon energy of the laser.

Since the chemical environment is leading to an additional damping, the differences among the dephasing time calculated from the optical constants of bulk silver and those measured here for nanoparticles with different stabilizers is attributed to the interaction of the coherently oscillating electrons with the surface of the nanoparticles. The mechanisms involve changes of the band structure at the nanoparticles boundaries. Two main mechanisms have been proposed:

1) *Chemical interface damping*, in which the oscillating electrons are excited to energy levels located in the adsorbate;

2) *Increased Landau damping* due to structural changes on the metal conduction band. The damping rate is enhanced by creation of electron-hole pairs near the nanoparticles surface. In this case, the electron-hole pairs are located inside the conduction band.

The relative contribution of both processes is still an open question and PSHB is unable to distinguish them.

The extra damping in the present measurements is comparable to results observed for nanoparticles functionalized with different molecules. In [Hu11b], the authors measured $T_2$ in silver nanoparticles with $R_{\mathrm{eq}}$ ~ 7.5 nm covered with $SO_2$. The damping parameter was approximately $A$ = 1.8 nm/fs. In a situation closer to the present case, [Hu07] investigated the dephasing time of a TSC-stabilized aqueous gold colloid with $R_{\mathrm{eq}}$ = 17 nm using the PSHB technique. The damping parameter was estimated to be $A$ = (2.72 ± 0.56) nm/fs, which is slightly larger than the found here.

It is interesting to discuss the role of water in the damping of the LSPs in passivated nanoparticles. The relative surface density of molecules for a given plane direction can be estimated by the Boltzmann statistics [Hu87]

$$\frac{N_a}{N_b} = \frac{\exp\left(E_a / k_b T\right)}{\exp\left(E_b / k_b T\right)} \tag{4.28}$$

where $N_a$ ($N_b$), $E_a$ ($E_b$) are the surface density and binding energy of molecule $a$ ($b$), respectively, $k_b$ is the Boltzmann constant and $T$ is the temperature of the system. As the binding energies of TSC [Ki08] and water molecules [Ra04] on the Ag (111) plane are estimated to be 0.6 eV and 0.2 eV respectively, the nanoparticle surface coverage of TSC is ~ $10^6$-fold larger than that of water. Therefore, we expect that the dephasing is mainly due to the interaction with the stabilizing molecules. However, it is a fact that the solvent can induce spectral line broadening of molecules in solution or influence the rate of charge transfer between interacting systems, according to Marcus electron transfer theory [Ma85]. Thus, the role of the solvent cannot be disregarded. This is corroborated by previous measurements of the damping parameters of the LSPs in silver nanoparticles capped by thick silica shells that protect the nanoparticles from solvation effects [Ba09]. In that case, the damping parameters found ($A$ ~ 0.5 nm/fs) are smaller than those found in the present study.

B) DFT calculations

The optimized geometries obtained from the DFT calculations are shown in fig. 4.17. The structural rearrangement of the metal molecule-interface is the result of an interfacial dipole created due to a permanent charge-transfer between the molecule and the metal [Cr02] [Ts10]. Figure 4.18 shows the Mulliken charge analysis for the different stabilizers. TSC binds to the surface by taking $0.87e^-$ from the surface, while the PVP monomer donates $0.38e^-$ and the PVA dimer takes $0.48e^-$. The non-integer charge represents a dislocation of the electronic cloud. Figure 4.19 shows a top and bottom view of the stabilizer-cluster bond, where the lower-lying Ag atoms were removed. The distance between the atoms are displayed in tables 4.2-4.4. In TSC, the carboxyl groups bind to the surface via the oxygen atoms, while the hydroxyl group points in opposite direction of the surface. The oxygen of the PVP pyrrolidone group binds to the Ag surface and, as a consequence of the rigid π bond between oxygen and pyrrolindone, the plane of the pyrrolidone group lies perpendicular to the surface. This oxygen is proximal to the barycenter of a triangle formed by Ag atoms at an average distance of 2.47 Å to the nearest silver atoms. PVA binds to the Ag surface via their unhydrolized oxygen atoms of the hydroxyl groups. As in PVP, the PVA oxygen atoms are located above the barycenter of a triangle formed by Ag atoms. However, the average distance from the O atoms to the nearest Ag atoms is shorter (2.29 Å) for PVA.

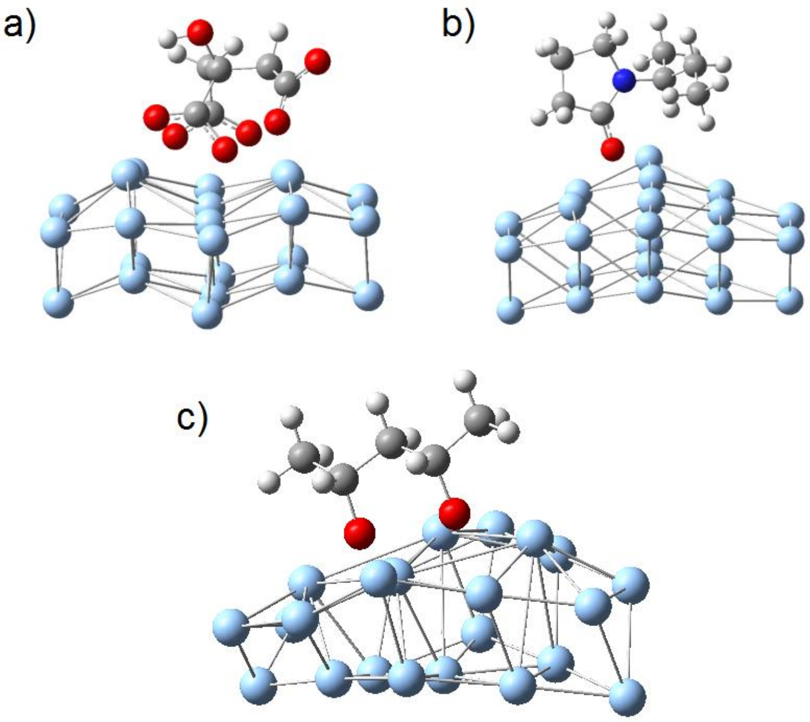

Fig 4.17 – Optimized geometries for TSC (a), PVP monomer (b), and PVA dimer (c) adsorbed on silver(111). Oxygen (red), carbon (dark gray), hydrogen (light gray), nitrogen (dark blue), silver (light blue).

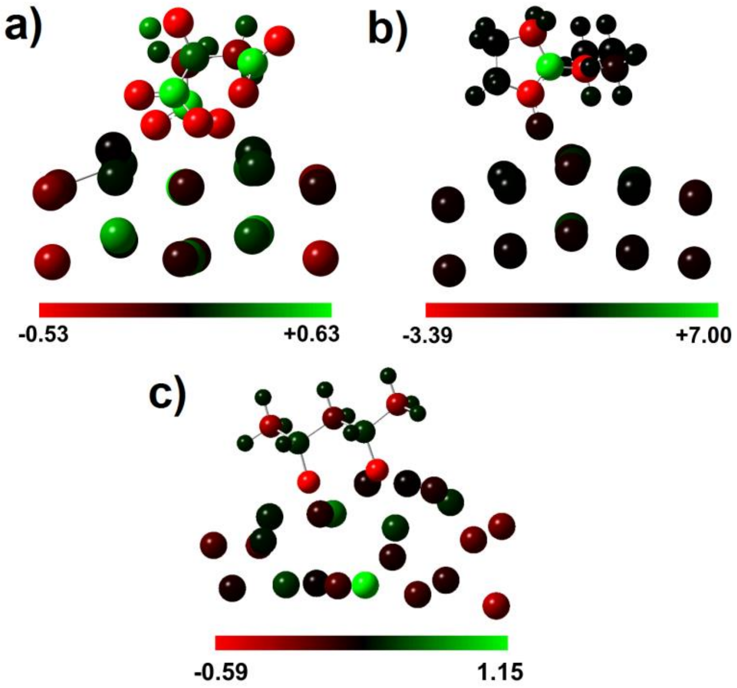

Fig. 4.18 – Mulliken charge analysis for TSC (a), PVP (b), and PVA adsorbed on silver (111). The scale is in units of elementary charge.

We now look for a more quantitative criterion for the electronic interaction between the clusters and the adsorbed molecules via the spatial localization of the molecular orbitals and the local density of states (LDOS). The atomic orbitals $\left|\phi_\mu\right\rangle$ of the total system (T) (cluster + molecule) are assumed to belong to two contiguous regions, namely the silver cluster group (C) and the molecular group (M), such that the molecular orbitals can be written as a linear combination of atomic orbitals as [Sz96]

$$\left|\psi_i\right\rangle = \sum_{\mu}^{T} c_{\mu i}\left|\phi_\mu\right\rangle = \sum_{\mu}^{C} c_{\mu i}\left|\phi_\mu\right\rangle + \sum_{\mu}^{M} c_{\mu i}\left|\phi_\mu\right\rangle, \tag{4.29}$$

where the $c_{\mu i}$'s are the coefficients in the linear expansion of the *i*th molecular orbital. The orthonormallity of the molecular orbitals,

$$\left\langle\psi_i\middle|\psi_j\right\rangle = \delta_{ij} = \Gamma_C^i + \Gamma_M^i , \tag{4.30}$$

is satisfied if

$$\Gamma_C^i = \sum_{\mu}^{C}\sum_{\nu}^{C}\left(c_{\nu i}\right)^* S_{\nu\mu} c_{\mu i} + \sum_{\mu}^{C}\sum_{\nu}^{M}\left(c_{\nu i}\right)^* S_{\nu\mu} c_{\mu i} , \tag{4.31}$$

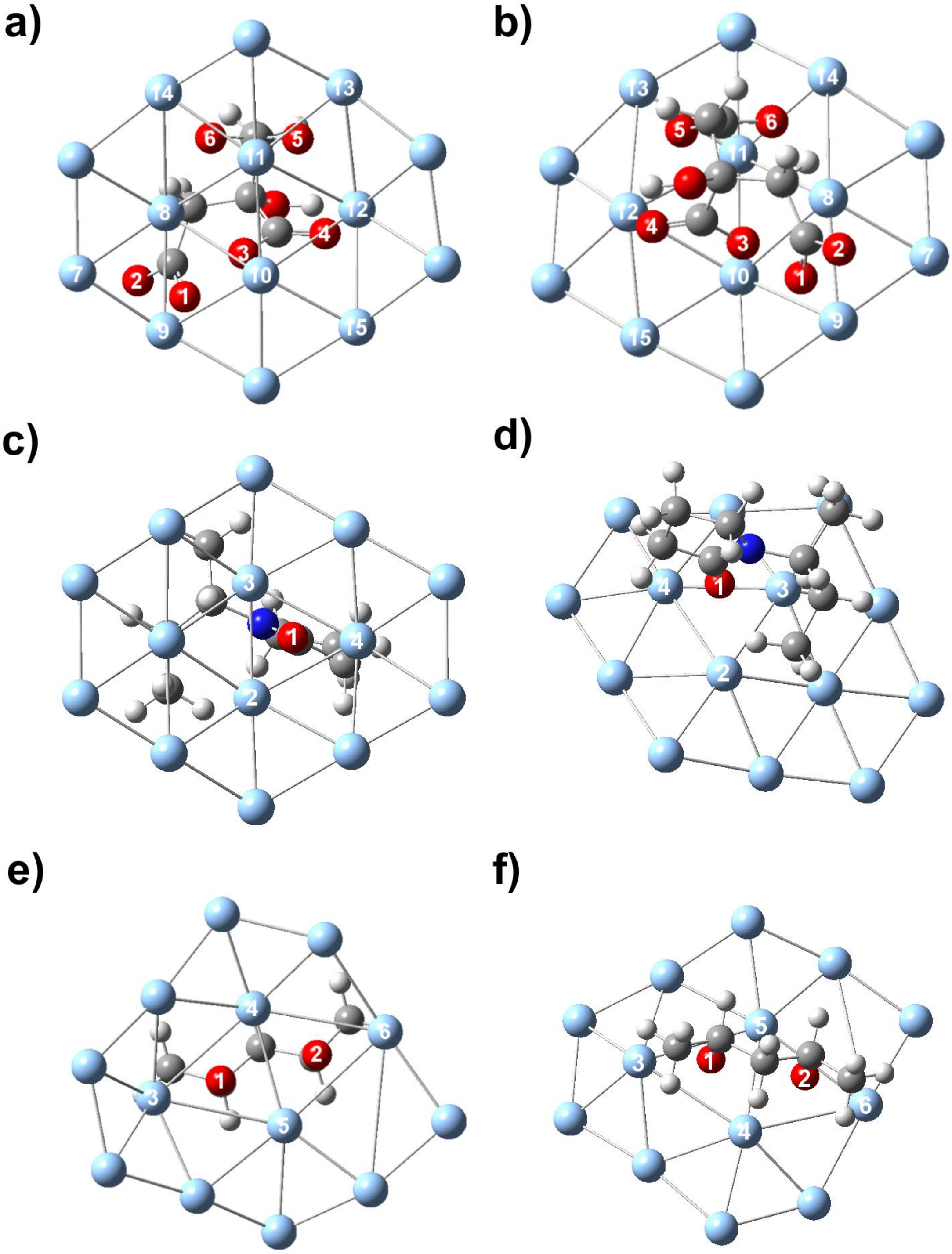

Fig. 4.19 - Bottom (left) and top (right) views of optimized geometries for the first atomic plane of silver (111) and the capping molecules TSC (a) and (b), PVP (c) and (d), and PVA (e) and (f). The distance between the molecules' atoms and the silver atoms are given in tables 4.2-4.4.

| Binding pair (O-Ag) | Distance (angstroms) | Binding pair (O-Ag) | Distance (angstroms) | Binding pair (O-Ag) | Distance (angstroms) |
|---|---|---|---|---|---|
| 1-8 | 3.53 | 3-8 | 2.67 | 5-11 | 2.48 |
| 1-9 | 2.76 | 3-10 | 2.37 | 5-12 | 2.48 |
| 1-10 | 4.18 | 3-9 | 3.15 | 5-13 | 2.53 |
| 2-7 | 5.59 | 4-10 | 3.69 | 6-11 | 2.63 |
| 2-8 | 4.94 | 4-12 | 2.41 | 6-8 | 2.39 |
| 2-9 | 4.66 | 4-15 | 3.64 | 6-14 | 2.53 |

Table 4.2 – Distance between the labeled oxygen atoms of TSC and silver atoms of the first silver (111) plane.

| Binding pair (O-Ag) | Distance (angstroms) |
|---|---|
| 1-2 | 2.53 |
| 1-3 | 2.44 |
| 1-4 | 2.45 |

Table 4.3 – Distance between the labeled oxygen atoms of PVP and silver atoms of the first silver (111) plane.

| Binding pair (O-Ag) | Distance (angstroms) |
|---|---|
| 1-3 | 2.24 |
| 1-4 | 2.32 |
| 1-5 | 2.33 |
| 2-4 | 2.35 |
| 2-5 | 2.35 |
| 2-6 | 2.21 |

Table 4.4 – Distance between the labeled oxygen atoms of PVA and silver atoms of the first silver (111) plane.

and

$$\Gamma_M^i = \sum_{\mu}^{M}\sum_{\nu}^{M}\left(c_{\nu i}\right)^* S_{\nu\mu} c_{\mu i} + \sum_{\mu}^{M}\sum_{\nu}^{C}\left(c_{\nu i}\right)^* S_{\nu\mu} c_{\mu i}\ , \tag{4.32}$$

where $S_{\nu\mu} = \left\langle \phi_\nu \middle| \phi_\mu \right\rangle$ is the overlap matrix elements of the (non-orthogonal) atomic orbitals. In eqs. (4.31) and (4.32), $\Gamma_C^i$ and $\Gamma_M^i$ are interpreted as the probability of finding the molecular orbital $\left|\psi_i\right\rangle$ in the C or M regions, respectively. With these probabilities, we can evaluate the spatial localization of the molecular orbitals and the LDOS, defined as [Da05]

$$D_M = \sum_i \Gamma_M^i \delta\left(\varepsilon - \varepsilon_i\right), \tag{4.33}$$

and

$$D_C = \sum_i \Gamma_C^i \delta\left(\varepsilon - \varepsilon_i\right), \tag{4.34}$$

where $D_M$ ($D_C$) is the LDOS for the adsorbate (cluster) region.

The LDOS calculated with basis on the above definitions for energies near the Fermi level are shown in fig. 4.20. For the three different stabilizing agents, there are several empty adsorbate states with energy $E$ such that the energy difference ($E - E_F$) with respect to the Fermi level $E_F$ is smaller or close to the photon energy used (2.94 eV) to excite the LSPs. This justifies an increase in the CID rate and shortening of $T_2$ compared to $T_2^\infty$. The resonance states whose excitation energies are much larger than the LSPs energy do not contribute to the CID effect [Pi03].

Interestingly, as displayed in Fig. 4.20, the structure of the LDOS at the metal region depends on the stabilizer, and a broadening of the conduction band states may lead to increased Landau damping at the nanoparticles surface. To the best of our knowledge, this adsorbate-induced band structure changes was never taken into account in the CID models. However, since Landau damping is the dominant dephasing mechanism in bare particles, these changes cannot be overlooked.

Figure 4.20 also shows isosurfaces of the probability density for the Kohn-Sham orbitals that may be involved in relevant transitions indicated by gray arrows. Most plasmon-driven electronic transfers occur from the silver clusters to atomic orbitals located near the binding oxygen atoms. Ideally, we could quantify the computational results with the experimental ones

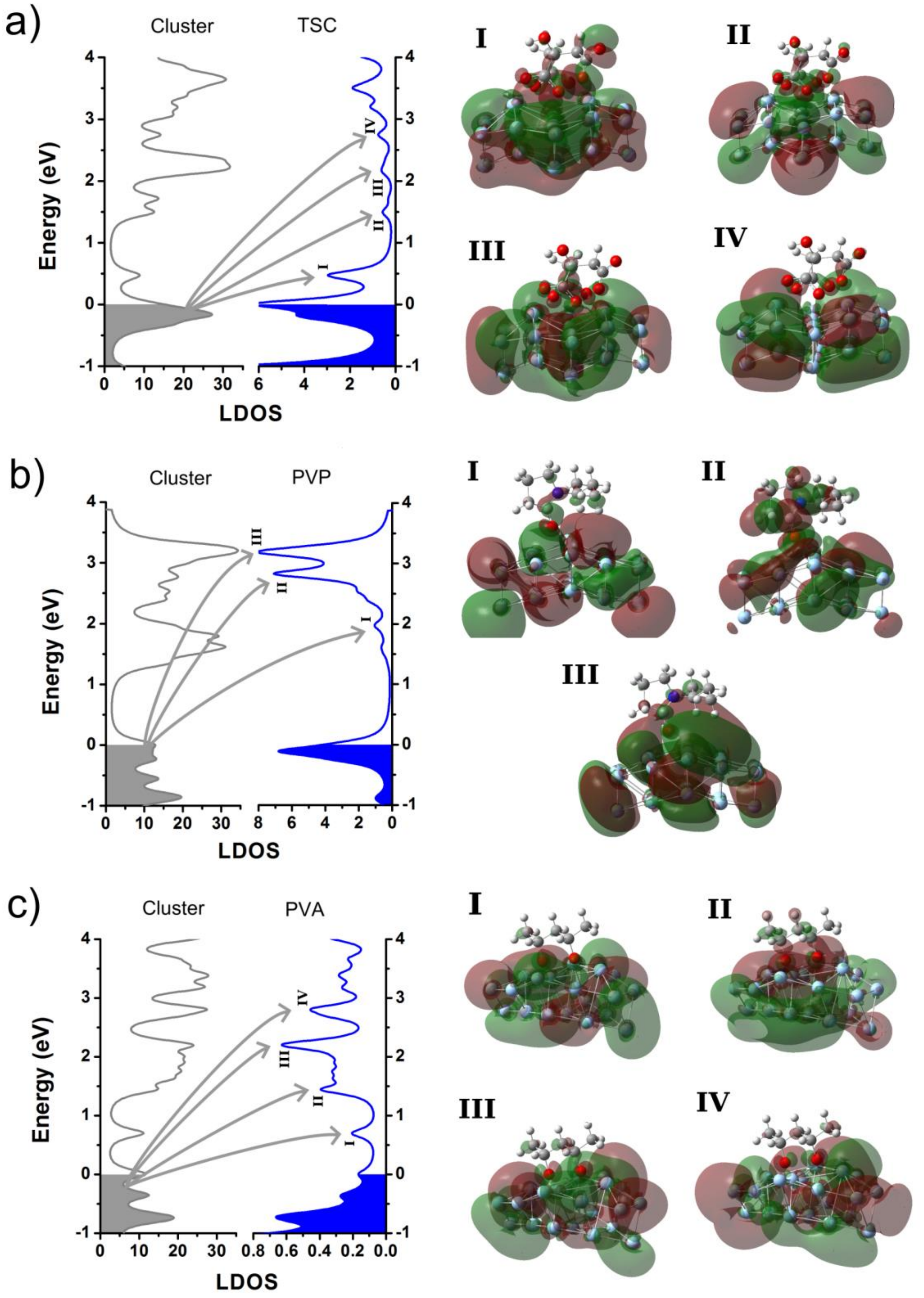

Fig. 4.20 – Calculated LDOS for silver nanoparticles stabilized with TSC (a), PVP (b), and PVA (c). The zero energy corresponds to the Fermi level of the metal. The relevant transitions are indicated by gray arrows along with the corresponding Kohn-Sham wavefunctions. The molecular orbitals are the following: a) I-LUMO, II-LUMO+1, III-LUMO+3, IV-LUMO+7; b) I-LUMO+6, II-LUMO+10, III-LUMO+13; and c) I-LUMO, II-LUMO+1, III-LUMO+6, IV-LUMO+10.

and compare the different stabilizers. However, that comparison can only be made qualitatively, since quantitative results depend on computationally expensive factors and parameters that are not available, such as the molecular surface density, the polymeric chain length, the size of the cluster and solvent effects. One interesting fact that may explain the longer $T_2$ measured for TSC-stabilized nanoparticles is that the molecular surface density of TSC depends on the Ag plane to which TSC in binded, as demonstrated in [Ki08]. By means of DFT calculation, they demonstrated that the binding energy of TSC in Ag is larger for the (111) plane compared (110) as a consequence of the best geometry matching between the Ag and O atoms of the carboxyl group for the (111) plane. They estimated that, with basis in eq. (4.28), the molecular surface density in the (111) plane is $10^6$-fold larger than in the (110) plane.

## 4.3 Conclusions

In this chapter, we investigated experimentally and theoretically the LSPs dephasing in colloidal silver nanoparticles, with typical diameters about 12 nm, stabilized with different capping agents. The results demonstrated that the dephasing times depends on the stabilizer chosen and are shortened due to the chemical interface damping effect or increased Landau damping at the nanoparticles surface. DFT calculations were performed for the metal cluster-adsorbate interaction and the results showed that either CID or increased Landau damping is occurring.

# 5. Pump-and-probe Spectroscopy in Rhodamine 590 Functionalized $TiO_2$ Nanoparticles and Glass-Ceramics Containing $NaNbO_3$ Nanocrystals

This chapter presents results of pump-and-probe transient absorption in two different systems: Rhodamine 590 linked to $TiO_2$ nanoparticles and glass-ceramics containing sodium niobate nanocrystals (GC-SNN). The aim in the first system is to probe charge injection from Rhodamine 590 into the $TiO_2$ nanoparticles at the surface, while in the second system we used transient absorption to investigate the ultrafast dynamics of in-gap states in the GC-SNN. For the second system, we also performed a time-resolved optical limiting experiment. In this case, we study the slow temporal decay of in-gap states. The results are theoretically modeled using a coupled rate equation model for the populations of the excited energy levels.

## 5.1 Dynamics of in-gap states of a glass-ceramic containing sodium niobate nanocrystals

The GC-SNN linear and nonlinear optical properties were discussed in detail in chapter 3. Optical limiting behavior was demonstrated in this material in the visible region of the spectrum, using picosecond [Fa04] and nanosecond lasers [Ol07]. The two-photon absorption coefficient in the nanosecond regime differs from that in the picosecond regime [Ol07] and the difference was attributed to the contribution of excited state absorption (ESA) and free-carriers absorption (FCA) to the nonlinear absorption. In chapter 3, we have shown how in-gap states of the GC-SNN, such as the nonbridging oxygen hole center (NBOHC), may contribute to the optical properties in the visible. In this chapter, we distinguish the different time scales of ESA using two different techniques: Femtosecond pump-and-probe transient absorption and dynamical optical limiting. Pump-and-probe experiments revealed at least two components for excited state absorption: a fast component with decay time shorter than 2 ps and a slow component whose decay time was beyond the temporal range of our apparatus. In dynamical optical limiting, a slower decay (ca. 150 μs) was measured, and a model was proposed taking into account the population of the energy levels participating in the process.

### 5.1.1 Femtosecond pump-and-probe transient absorption experiment

The experimental apparatus of the femtosecond transient absorption experiment is depicted in Fig. 5.1. For the pump beam, we used a Coherent Libra regeneratively amplified Ti:Sapphire laser ($\lambda$ = 800 nm, $\tau_p$ = 100 fs, 1 kHz repetition rate). The probe beam was derived from an optical parametric amplifier (OPA) (Coherent, Opera solo) pumped by the Libra laser whose output beam wavelength could be tuned from the UV to the NIR. The pump beam was frequency doubled by a nonlinear BiBO crystal (Castech, 1 mm long). A shortpass filter (Edmund optics, A84714) was used to reject the fundamental beam after the BiBO crystal. The pump beam intensity could be controlled by a $\lambda/2$ plate and a Glan polarizer. The pump beam was modulated by an optical chopper operating at 461 Hz and its optical path was controlled by a delay line (Newport, ESP301). The probe beam generated by the OPA was attenuated by neutral density filters and its intensity could be controlled by another $\lambda/2$ plate/Glan polarizer set. The probe beam was split into two beams: a weaker one called reference beam, with intensity ≈ 4% of the original beam, and a stronger one (compared to the reference) that we will still continue to call the probe beam. The pump and probe beams are slightly focused in the sample and the signal beam, generated along the probe direction, is detected (heterodyne detection, see chapter 2) by a BPW21 silicon photodiode. The pump and probe beams polarizations were set parallel except for degenerate excitation at 400 nm, in which their polarizations were set perpendicular and a polarizer in front of the detector filtered the signal beam from stray light of the pump beam. The probe beam intensity fluctuations were normalized using the reference beam detected by another identical BPW21 photodiode. This normalization is crucial to improve the signal-to-noise ratio. The intensity of unperturbed probe beam i.e., the beam that

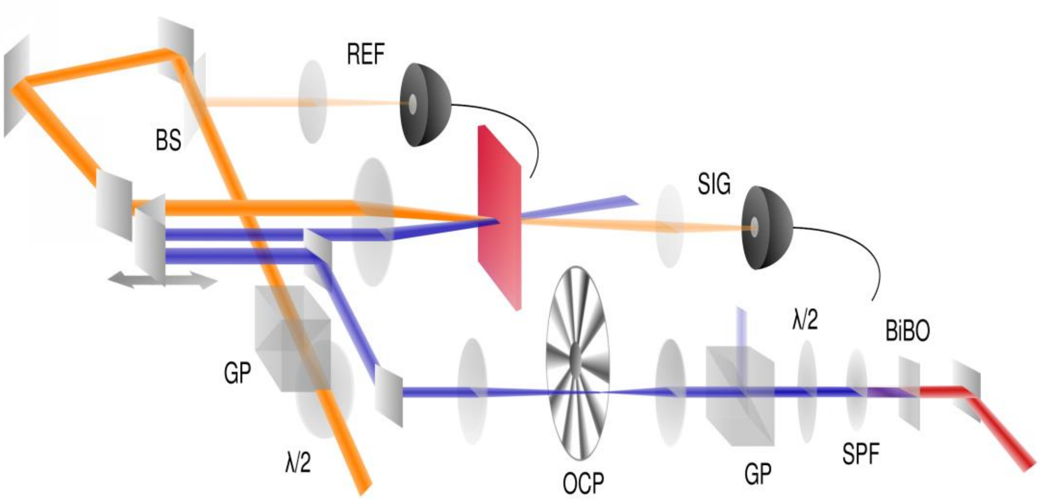

Fig. 5.1 – Simplified scheme of the pump-probe transient absorption experimental apparatus (see text). The blue beam is the pump, while the orange beam is the probe. SPF – shortpass filter, GP – Glan prism, OCP – optical chopper, BS – beam splitter, SIG – signal, REF – reference.

passed the sample without the presence of the pump, was set to 80 % of the reference beam intensity using variable neutral density filters in front of the detectors. The photodiode signals from the reference and signal beams were sent to two different boxcar averagers (Stanford SR250). The parameters of the two boxcars integrators were chosen to be the same. The averaging mode was set to "last shot". The signals processed by the two boxcars were then sent to an analog processor (Stanford, SR235) to normalize intensity fluctuations of the probe. The analog processor performed the operation $V_{out} = 10V_{sig}/V_{ref} = 8V_{sig}/V_{probe}$ were $V_{\text{sig}}$, $V_{\text{ref}}$ and $V_{\text{probe}}$ are the processed intensities of the signal, reference and unperturbed probe beams, respectively. The analog processor output voltage was sent to a lock-in amplifier (Stanford, SR530) locked at the chopper frequency (461 Hz). The phase of the lock-in was set positive (π/2) for excited state absorption and negative (-π/2) for bleach/stimulated emission. The lock-in amplifier communicated to a personal computer, which also controlled the delay line, via a GPIB interface.

The modulation of the pump beam by the optical chopper produces a square wave in the pump beam intensity. Hence, the signal intensity can be expressed in terms of Fourier series as [Ho98]

$$I(t) = I_0 + \Delta I\left[0.64\sin(\omega_c t + \theta_c) + 0.21\sin(3\omega_c t + \theta_c) + 0.13\sin(5\omega_c t + \theta_c) + \ldots\right] \quad (5.1)$$

where $I_0$ is the intensity of the unperturbed probe beam, $\Delta I$ is the variation in the probe beam intensity induced by the pump cf. eq. (2.7), $\omega_c$ = 461 Hz and $\theta_c$ are the frequency and phase of the chopper respectively. The lock-in detects the signal at the frequency $\omega_c$ and displays its root-mean-square (rms) voltage. Therefore, the lock-in output is given by

$$V_{rms} = \frac{1}{\sqrt{2}} 0.64 \frac{\Delta I}{I_{ref}} = 3.62 \frac{\Delta I}{I_{probe}} \quad (5.2)$$

where $I_{ref}$ and $I_{probe}$ are the intensities of the reference and unperturbed probe beams respectively. Defining the absorbance $A$ of the sample as

$$A = \log\left(\frac{I_0}{I}\right) \quad (5.3)$$

the absorbance changes $\Delta A$ are expressed as

$$\Delta A = \frac{1}{2.3} \frac{\Delta I}{I} \quad (5.4)$$

In terms of the lock-in output voltage, the absorbance changes are given by

$$\Delta A = 0.12 V_{rms} \tag{5.5}$$

With this system, absorbance changes as low as $10^{-5}$ could be accurately measured. The temporal resolution of the system is limited by the cross-correlation of the pump and probe beams, that was acquired by sum-frequency generation (SFG) of the pump ($\lambda$ = 400 nm) with the probe ($\lambda$ = 580 nm) in a BBO nonlinear crystal. The SFG signal ($\lambda$ = 237 nm) excited a rhodamine 590 ethanolic solution and the fluorescence intensity was measured with a BPW21 detector, whose spectral response is higher in the visible than in the UV. The cross-correlation is shown in Fig. 5.2. The full-width at half maximum (FWHM) is ~ 400 fs and is larger than the nominal pulse duration of the fundamental ($\tau_p$ ~ 100 fs) and probe beams ($\tau_p$ ~ 65 fs). Two main mechanisms may explain the broadening of the cross-correlation: dispersion by glassy optical components on the pump beam path and the relatively large beam waist at the sample[3] (~ 750 µm and ~ 380 µm for the pump and the probe beams respectively). Large beams waists were chosen to minimize overlap mismatch of the beams due to spatial variations of the probe beam. The overlap mismatch is critical since the beams traveled a long distance to reach the sample (~5m) and fluctuations in the room temperature caused displacement of the probe beam.

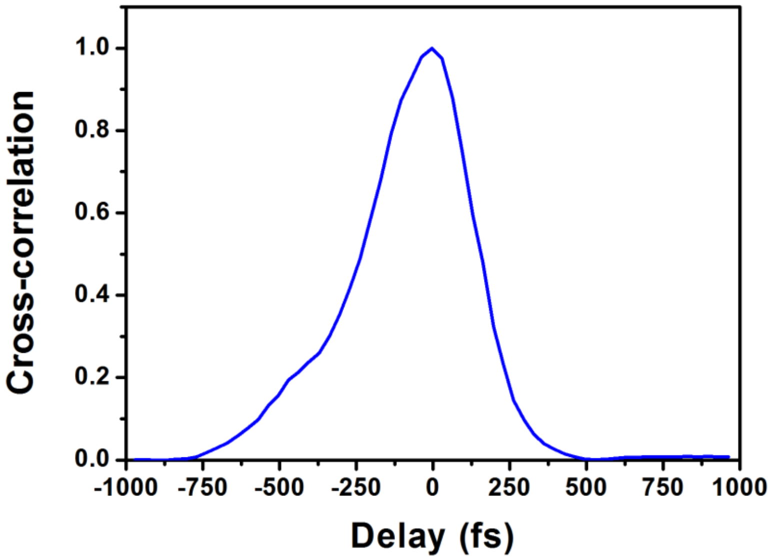

Fig. 5.2 – Cross-correlation between the pump ($\lambda$ = 400 nm) and the probe ($\lambda$ = 580 nm) in a 1 mm-thick BBO crystal.

---

[3] As, for large beam waists, the pulses experience different delays at different points of the superimposition region, this principle can be used to characterize the pulses (as in the Grenouille technique [Pa01]) or perform time-resolved spectroscopy [Pa07] without the need of a mechanical delay line.

| Sample | Annealing time (hours) | Filling fraction *f* | Sample length (mm) | Density $\rho_m$ (g/cm$^3$) | Band-gap energy $E_g$ (eV) |
|---|---|---|---|---|---|
| S2 | 2 | 0.00 | 3.25 | 3.670 | 3.6 |
| S8 | 8 | 0.03 | 3.45 | 3.692 | 3.5 |
| S33 | 32 | 0.20 | 3.30 | 3.695 | 3.2 |
| S69 | 69 | 0.36 | 3.65 | 3.757 | 3.2 |
| S92 | 92 | 0.36 | 3.45 | 3.810 | 3.2 |
| S114 | 114 | 0.35 | 3.15 | 3.823 | 3.2 |
| S206 | 206 | 0.37 | 3.50 | 3.835 | 3.2 |

Table 5.1 – Some features of the GC-SNN investigated by femtosecond pump-probe differential absorption.

The glass-ceramics containing $NaNbO_3$ nanocrystals (GC-SNN) were prepared by annealing the glass with a molar % composition of $35SiO_2$-$31Nb_2O_5$-$19Na_2O$-$11K_2O$-$2CdO$-$2B_2O_3$ at 610 ºC during different time intervals (see chapter 3 and references [Fa04] [Li03b]). Table 5.1 shows some features of the samples investigated in this chapter. The average size of the nanocrystals (~ 12 nm) is independent of the annealing time. However, the filling factor *f* i.e., the volumetric fraction of the crystalline phase, increases during the annealing time and saturates after 69 h of heat treatment. Figure 5.3 shows the linear absorption spectra of the GC-SNN. The samples present a large transparency window extending from blue to the near-infrared. The optical band-gap of the GC-SNN varies from 3.6 eV ($f$ = 0) up to 3.2 eV ($f$ ~ 0.37). The absorption spectrum (extinction spectrum, more precisely) of the S33 shows a $1/\lambda^4$ dependence due to light scattering by $NaNbO_3$ nanocrystals aggregates [Fa04].

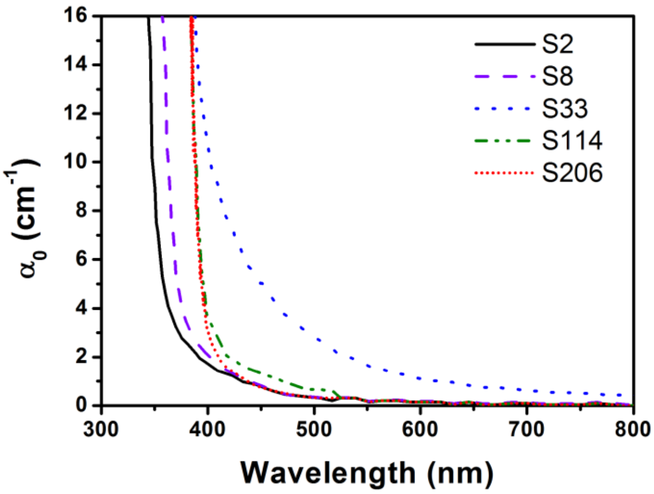

Fig. 5.3 – Linear absorption spectra of some GC-SNN.

### 5.1.2 Results and discussion

Figure 5.4 shows the transient absorption signals for probe wavelengths at 400 nm (a), 530 nm (b), 580 nm (c) and 640 nm (d). The pump and probe energies per pulse are ≈ 1 µJ and ≈ 65 nJ respectively. The samples present an ESA signal whose dynamics depends on the excitation wavelength and the filling factors of the samples. For degenerate pump-probe, the dynamics resembles the cross-correlation, while for the other probe wavelengths at least four different dynamics can be distinguished (including the rise of the signal). In the first part, the strong peak, common to all samples, is due to the overlap between both pump-probe beams. After the excitation the temporal behavior of the signal (fig. 5.5) can be fitted by an exponential function whose decay time varies from $\tau_d \sim 1.1$ ps (for $\lambda = 530$ nm and 580 nm) to $\tau_d \sim 1.7$ ps ($\lambda = 640$ nm). Clearly, the signal decays slower for longer wavelengths. After the first decay process, the signal decays suddenly with a characteristic time ~ 400 fs, which is almost equal to the temporal resolution of the apparatus. This implies that this decay time might be even faster. Its origin is unclear but the presence of an intermediate short lived in-gap state or stimulated emission of the probe might explain this behavior. The hypothesis of stimulated emission is corroborated by the fact that the first

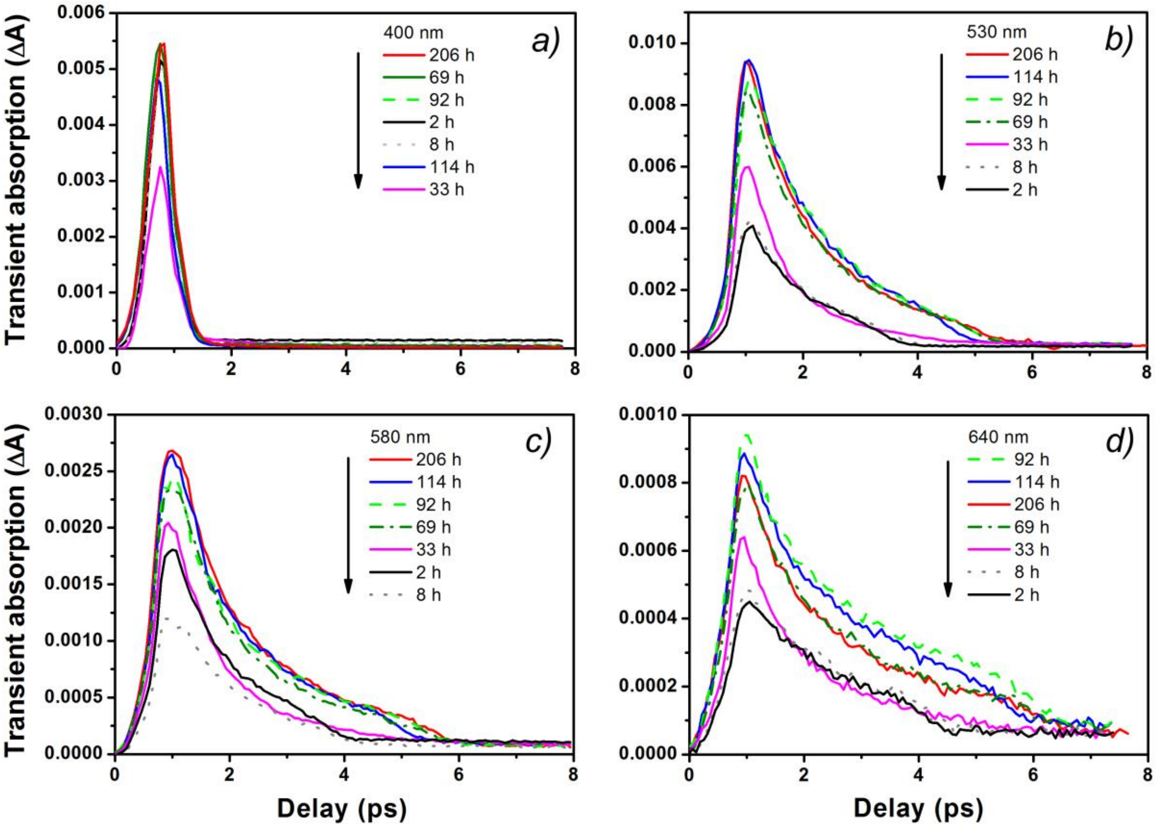

Fig. 5.4 – Transient absorption signal in the GC-SNN for pump excitation at 400 nm and probe wavelengths 400 nm (a), 530 nm (b), 580 nm (c) and 640 nm (d).

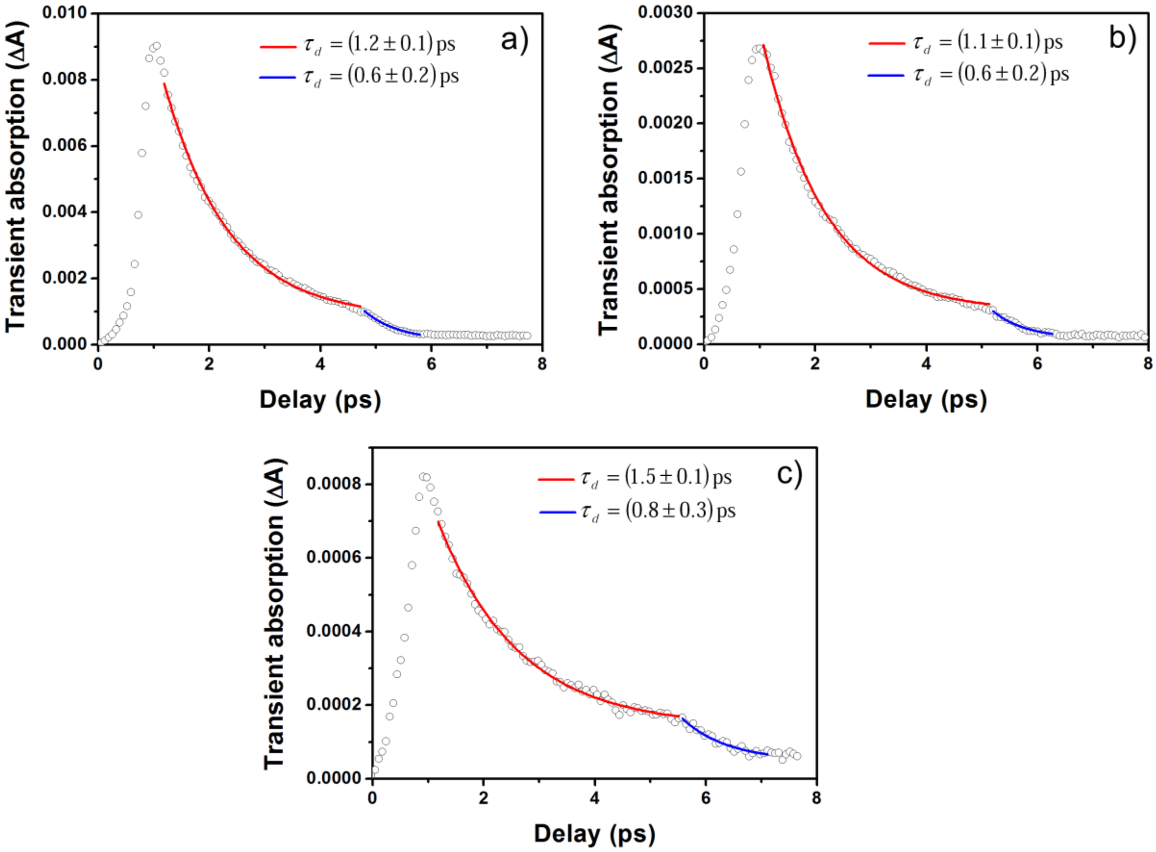

Fig. 5.5 – Exponential fits to the transient excited state absorption signal of the glass-ceramic annealed for 206 h for probe wavelength at 530 nm (a), 580 nm (b) and 640 nm (c) and their respective decay times.

signal decay, which is stopped by the second process, is longer for smaller photon energies. Furthermore, this sudden decay is not present in the degenerate pump-probe experiment. The decay time of the last process is beyond the range of our delay line (which is ~ 3 ns) and may be attributed to long lived deep trap states. These long lived trap states contribute for ESA in the optical limiting experiments in the nanosecond and picosecond regimes [Fa04] [Ol07].

The decay times are almost independent of *f* and the long component of the ESA decay is present in all samples. However, the decay profile of the undoped sample S2 is different compared to the other samples' signal decay. The decay behavior of the S2 sample is non-exponential at earlier times.

## 5.2 Pump-probe transient absorption in rhodamine 590 linked to amorphous $TiO_2$ nanoparticles

The charge-transfer mechanisms from dye to semiconductor nanoparticles and the time scales involved in these processes are a matter of interest for diverse applications, such as dye-sensitized solar cells (DSC) [Gr03] [Ha12], photodynamic therapy [Wa03] and photocatalysis [Be00]. In DSC, electron transfer occurs from excited LUMO (lowest unoccupied molecular orbitals) states of the dye to the conduction band of the semiconductor. For the electron transfer to take place, the conduction band energy of the semiconductor must be lower than the LUMO states of the sensitizer. Titanium dioxide ($TiO_2$) often meets this requirement and therefore, is the most widely semiconductor employed in DSC.

Fast electron transfer is mandatory to avoid exciton recombination before charge transfer and therefore, improve the efficiency of a DSC. Conversely, slow backward charge transfer (from the semiconductor to the dye) increases the efficiency of a DSC. The charge transfer is highly sensitive to surface conditions, such as the presence of defects, and the energetic distances and spatial overlap between the LUMO states of the dye and the semiconductor conduction band [An05]. The LUMO-conduction band energetic distance can be tuned by the appropriate choice of the dye or, if another semiconductor is employed as the sensitizer, by changing the size, and hence the energy band-gap, of the semiconductor. Furthermore, the solvent is another factor that contributes to the electron transfer rates [Ma85].

In this chapter, we investigate charge transfer from rhodamine 590 to amorphous $TiO_2$ nanoparticles in colloidal suspension via pump-probe transient absorption. The fundamentals of the pump-probe technique were discussed in detail in chapter 2. The experimental apparatus is the same as described in section 5.1.1.

### 5.2.1 Experiment

The rhodamine 590 functionalized $TiO_2$ nanoparticles were synthesized by Dr. Antonio Marcos de Brito Silva from the Centro de Tecnologias Estratégicas do Nordeste (CETENE)-Brazil and Ms. Andréa F. da Silva from the Materials Science Graduate Program at Universidade Federal de Pernambuco, Brazil. The synthesis involved the formation of amorphous $TiO_2$ nanoparticles by hydrolysis of titanium tetrabutoxide with subsequent functionalization of the nanoparticles with Rhodamine 590 (Rh6G). Amorphous $TiO_2$ nanoparticles were synthesized as described in [Su08]. First, 5 mL of a 1:1 ethanol/acetonitrile solution was prepared. Then 0.1 M of titanium tetrabutoxide (TBO) was added to this solution under nitrogen atmosphere to form the EtOH/AN/TBO solution. A second 1:1 ethanol/acetonitrile solution (5 mL) was prepared. To this new solution, 0.2 M of $NH_4OH$ and 1 M of Milli-Q water were added to form the EtOH/AN/NOH solution.

$TiO_2$ nanoparticles were generated by adding the EtOH/AN/NOH solution to the EtOH/AN/TBO solution under magnetic stirring. The final solution was stirred at 550 rpm for 5 hours. After this interval, 10 mL of ethanol were added to stop the reaction.

The final solution was centrifuged at 10,000 rcf for 5 minutes and the supernatant was extracted. The nanoparticles at the bottom of the tube were resupended in ethanol. This procedure was repeated five times.

To functionalize the $TiO_2$ nanoparticles with rhodamine 6G, a precursor Si:Rh6G solution [Gr07] was prepared by first adding $1.6x10^{-4}$ M of Rhodamine 6G to 13 mL of acetonitrile under magnetic stirring. To this solution, 1 mL of methanol was added to increase the solubility of the dye. Then $1.6x10^{-4}$ M of 3-isocyanatepropyltriethoxysilane were added. The final Si:Rh6G solution was stirred for 24 hours. The dye reacts with the silane according to fig. 5.6. After the reaction, 5 mL of the $TiO_2$ colloidal solution was mixed with 10 mL of the precursor Si:Rh6G solution. The colloid was kept under reflux at 80 ºC for 24 hours.

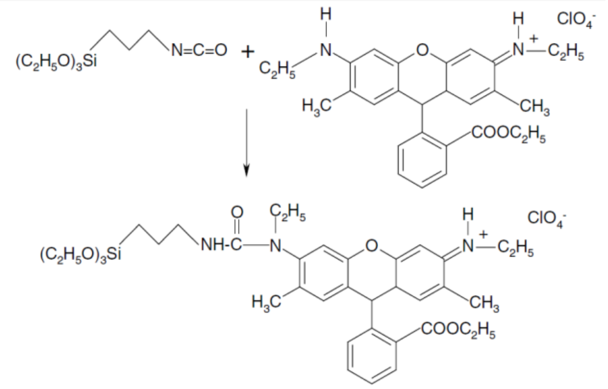

Fig. 5.6 – Product of the reaction between Rh6G and the silane used in the synthesis (from [Gr07]).

After 24 hs, the new colloid was centrifuged at 10.000 rcf for 5 minutes. The supernatant was extracted and the particles at the bottom of the tube were redispersed again in ethanol under sonification. This procedure was repeated until no more dye could be extracted from the suspension. After the last centrifugation, the functionalized particles were redispersed in 14 mL of ethanol.

### 5.2.2 Results and discussion

A representative scanning electron microscopy (SEM) image of the synthesized amorphous $TiO_2$ nanoparticles is shown in fig. 5.7. The nanoparticles are ellipsoidal with an average equivalent

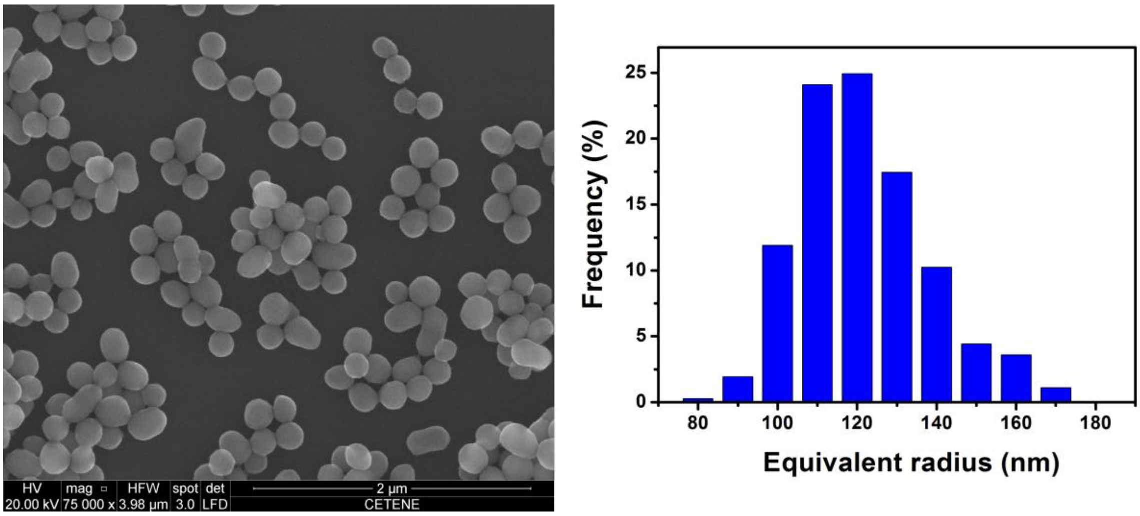

Fig. 5.7 – Representative SEM image of the synthesized titanium dioxide nanoparticles and histogram of the corresponding size distribution.

radius of 120 nm. The dye is proposed to anchor to the $TiO_2$ nanopaticles via OH groups at the nanoparticles surface formed during the hydrolysis reaction. Fig 5.8 shows the absorption spectrum of the Si:Rh6G solution. The rhodamine 590 absorption bands are unmodified despite the binded silane [Gr07]. The absorption spectrum of the functionalized $TiO_2$ nanoparticles (not shown) is dominated by scattering due to the nanoparticles. In the ultraviolet, absorption by the nanoparticles starts to contribute since the energy band–gap of amorphous $TiO_2$ is ≈ 3.3 eV. For the TA experiment, the pump was chosen at 400 nm, resonant with the dye, and the probe was set at 530 nm at the maximum of the $S_0$-$S_1$ transition of the dye. The polarizations of the pump and probe beams were set parallel and they crossed in a 2 mm long quartz cuvette containing the dye and the colloid. The optical density at 400 nm was ≈ 0.03 for the dye and ≈ 2.50 for the colloid.

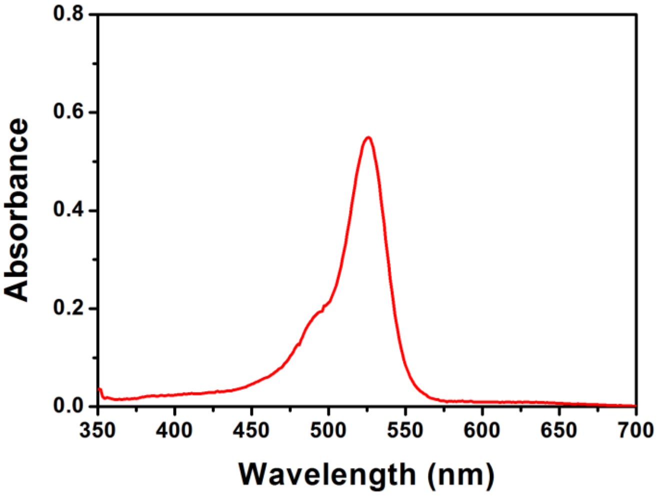

Fig. 5.8– Absorption spectrum of the Si:Rh6G solution.

The normalized transient bleaching signal is shown in fig. 5.9a for the Si:Rh6G solution (squares) and the functionalized $TiO_2$ nanoparticles (circles). The unfunctionalized nanoparticles did not show any transient absorption signal. Although the colloid is highly scattering, our experimental apparatus was sensitive to measure absorbance changes in the transmission mode. In this case, the absorbance changes were on the order of $10^{-4}$ at the maximum of the signal for the colloid. Figure 5.9b shows the possible pathways that the excited electron can follow after pump excitation. As the excited electrons and holes in the dye are transferred or recombine, the bleaching signal is recovered. The TA curves were fitted by single exponential functions. For the Si:Rh6G solution, the bleaching recovery time is ≈ (2.9±0.5) ns, which is smaller than the rhodamine 590 lifetime in ethanol (~ 4.0 ns) [Po78]. However, for the dye binded to $TiO_2$, the bleach recovery time was shortened to (0.7±0.2) ns, indicating that charge transfer is occurring from thermalized excited states of the dye to the $TiO_2$ conduction band.

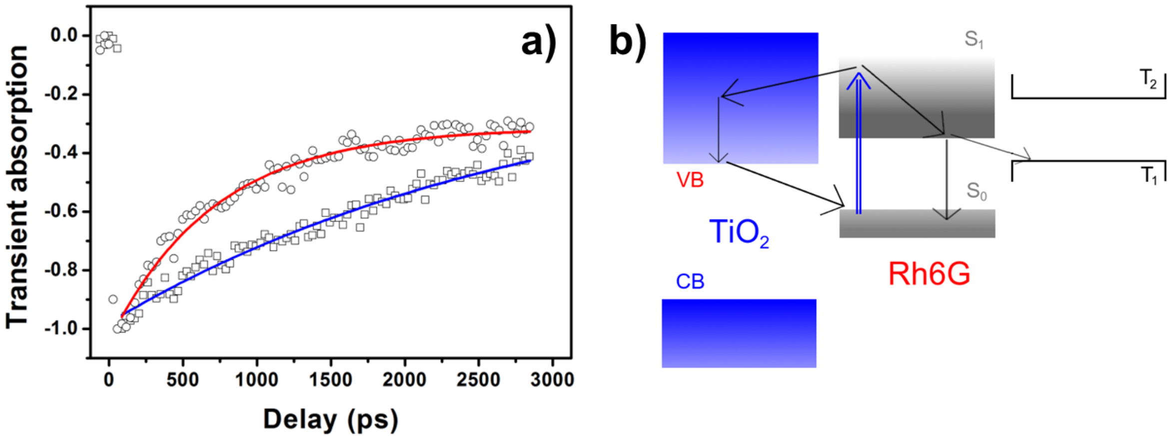

Fig. 5.9 – a) Normalized transient absorption signal for the Si:Rh6G solution (open squares) and Rh6G linked to $TiO_2$ nanoparticles (open circles). The curves are exponential fits to the experimental data. b) Schematic representation of the possible pathways for an electron following excitation at 400 nm. CB – conduction band, VB – valence band.

The offset is a signature that the bleaching recovery is not completed during the time scale investigated due to trapping of electrons at in-gap states of the semiconductor or trapping of molecules in triplet states. The charge-transfer rate can be calculated by

$$k_{et} = \frac{1}{\tau_{(Si:Rh6G+TiO_2)}} - \frac{1}{\tau_{(Si:Rh6G)}} \tag{5.6}$$

where $\tau_{(Si:Rh6G+TiO_2)}$ and $\tau_{(Si:Rh6G)}$ are the lifetimes of the dye linked to $TiO_2$ and the Si:Rh6G solution, respectively. Using the constants extracted from the exponential fits to the transient absorption data, the charge transfer rate is on the order of $10^9$ $s^{-1}$. This value is smaller than the charge transfer rates for other classes of dyes, such as ruthenium complexes or donor-pi-acceptors [Ha15], or semiconductor quantum dots linked to anatase $TiO_2$ nanoparticles in different environments [Ro06]. Values for $k_{et}$ in these systems are in the range $10^9$–$10^{13}$ $s^{-1}$. The charge transfer rate is sensitive to the distance between the center of excitation at the donor and the acceptor. In our case, the silane molecule is a barrier for the charge transfer. Furthermore, it is known that both forward and backward charge transfer rate are smaller for amorphous $TiO_2$ nanoparticles than for anatase [Ma98]. In summary, systematic variations in the hybrid system (linking molecule, solvent and crystallinity of the nanoparticles) are necessary to improve the charge transfer rate.

## 5.3 Dynamical optical limiting experiment in a GC-SNN

### 5.3.1 Experiment

To further understand the dynamics of in-gap states of the GC-SNN, we performed a dynamical optical limiting experiment using a time-resolved optical limiting apparatus (Fig. 5.10). As the light source, we used a Coherent Mira 900 mode-locked Ti:Sapphire laser (λ = 772 nm, 100 fs, 76 MHz). The fundamental radiation was frequency doubled by a nonlinear BiBO crystal (386 nm, 3.21 eV). The energy of the second harmonic could be controlled by a λ/2 plate – Glan polarizer set positioned before the BiBO crystal. The fundamental radiation was later rejected by a shortpass filter (Edmund, A84714) positioned after the doubling crystal. The beam passed through a 1:1

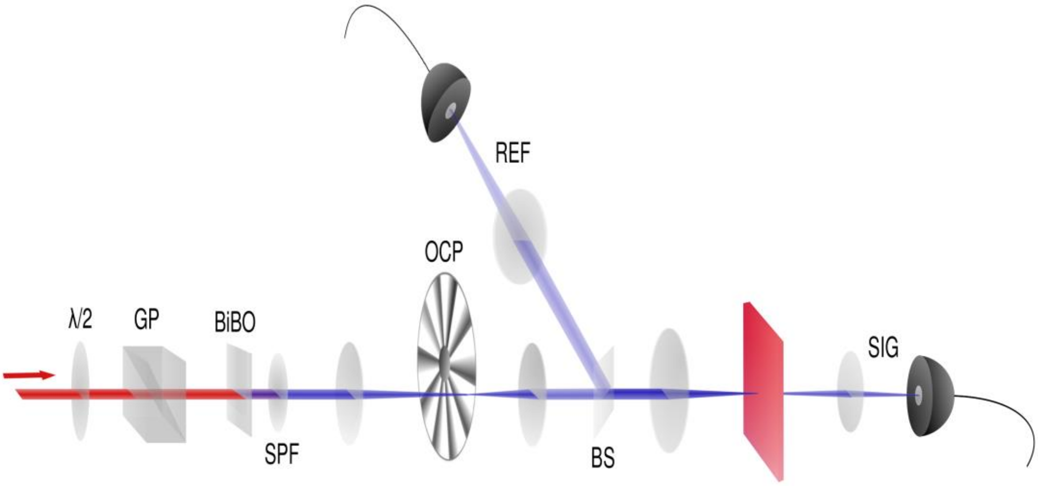

Fig. 5.10 – Schematic representation of the optical limiting experimental apparatus. SPF – shortpass filter, GP – Glan prism, OCP – optical chopper, BS – beam splitter, SIG – signal, REF – reference.

telescope and, at the focal region of the telescope, the beam was modulated by an optical chopper. The beam was further split into two beams. One of them, with energy almost 4 % of the original beam, is sent to a reference silicon photodiode (BPW21). The majority of the beam was then focused by a 10 cm focal length lens on the sample. The estimated beam waist in the focus is ≈ 30 μm. The transmitted light was collected by a 10 cm focal length lens and focused on another BPW21 photodiode. The signals from this photodiode were sent to a Tektronix TDS1012 digital oscilloscope, were the waveform of the signal could be recorded. The energy of the transmitted beam was measured after the sample by a joulometer that was removed from the beam path for the acquisition of the signal's waveform.

### 5.3.2 Results and discussion

The temporal evolution of the transmitted intensities by the samples S2, S8, S114 and S206 are shown in fig. 5.11 for different excitation intensities. Clearly, the transmitted intensity decays with time for all samples and this effect is more pronounced for higher incident intensities. The behavior

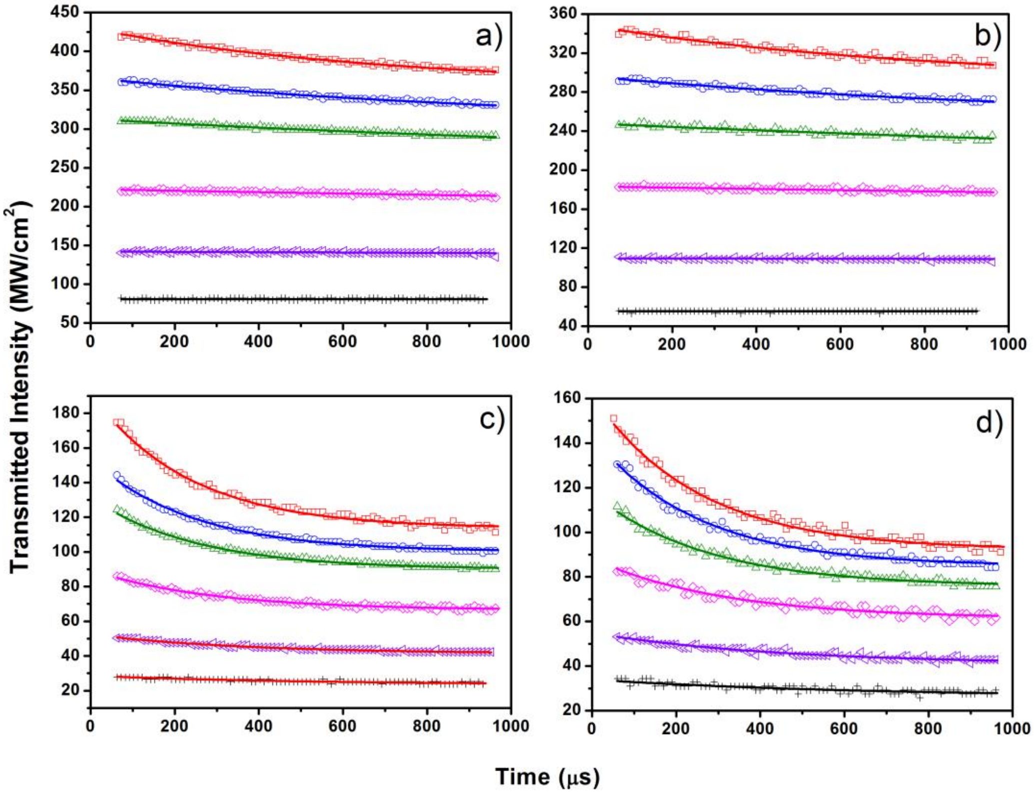

Fig. 5.11 – Dynamical OL behavior for the samples S2 (a), S8 (b), S114 (c), S206 (d) at different incident intensities. The incident intensities are 1620 MW/cm$^2$ (red squares), 1340 MW/cm$^2$ (blue circles), 1120 MW/cm$^2$ (green up triangles), 780 MW/cm$^2$ (magenta diamonds), 450 MW/cm$^2$ (violet dropped triangles) and 240 MW/cm$^2$ (black crosses).

of the transmitted intensity can be described reasonably well by exponential functions. During the illumination time (≈ 1ms), the transmitted intensity reaches the steady state. An optical limiting (OL) behavior is observed for longer times. This is clear from fig. 5.12, where the transmitted intensity is plotted as a function of the incident intensity for $t = 0$ and $t =$ "infinity". The transmitted intensity was obtained at these times extrapolating the fitted exponential curves. When an exponential curve could not be fitted, an average of the signal at earlier times was taken (chopper aperture) and at later times (before chopper blocks the beam).

To model the dynamical OL of these samples, we propose that the dynamical OL is associated with population accumulation effects. The proposed model is shown in Fig. 5.13. First, the pulses drives population from the top of the valence band (state $|0\rangle$) to the bottom of the conduction band (state $|1\rangle$) at a pump rate $W_{p01}(t) = \sigma_{01} I(t)/h\nu_p$, where $\sigma_{10}$ is the linear absorption cross-section, $I(t)$ is the time-dependent excitation intensity, $h$ is the Planck constant and $\nu_p$ is the laser optical frequency. As the repetition rate of the laser is 76 MHz, the pulses arrive at the sample every 13.1 ns. From the bottom of the conduction band, the excited electrons may follow three different paths:

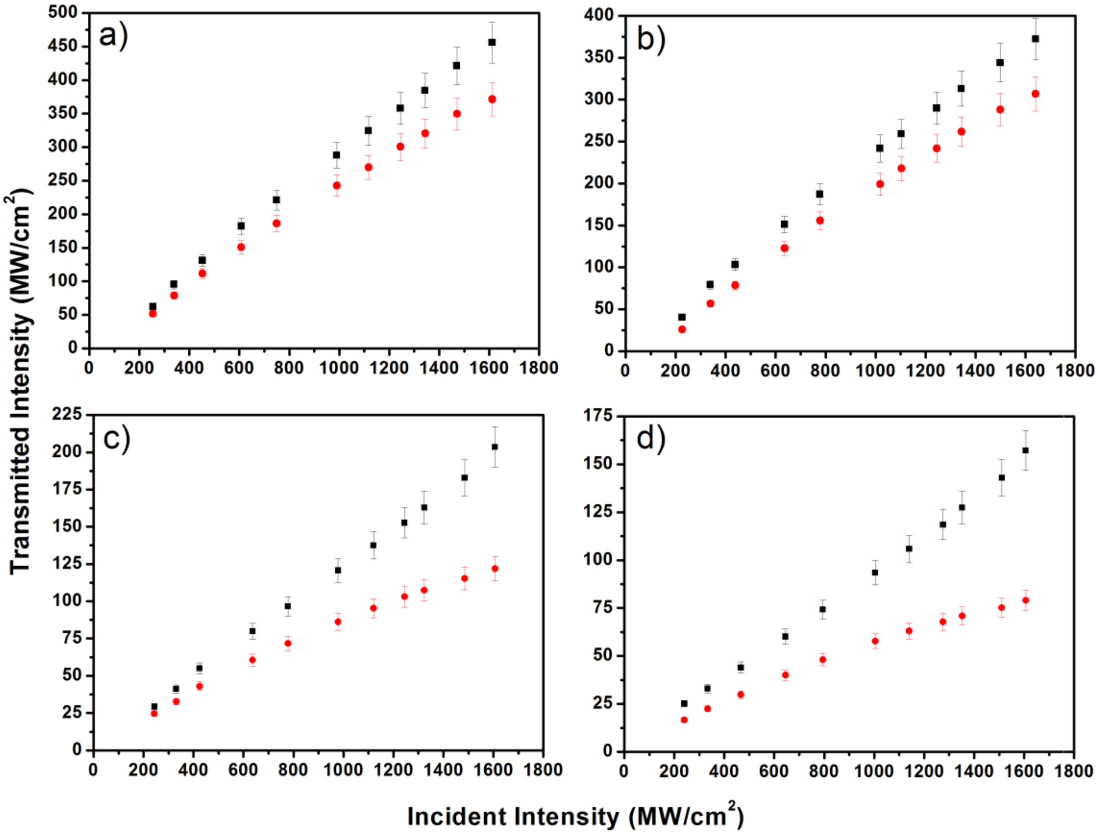

Fig. 5.12 – "Classical" OL curves for samples S2 (a), S8 (b), S114 (c), S206 (d). The black squares and red circles are the transmitted intensities for time $t = 0$ and $t =$ "infinity" (see text).

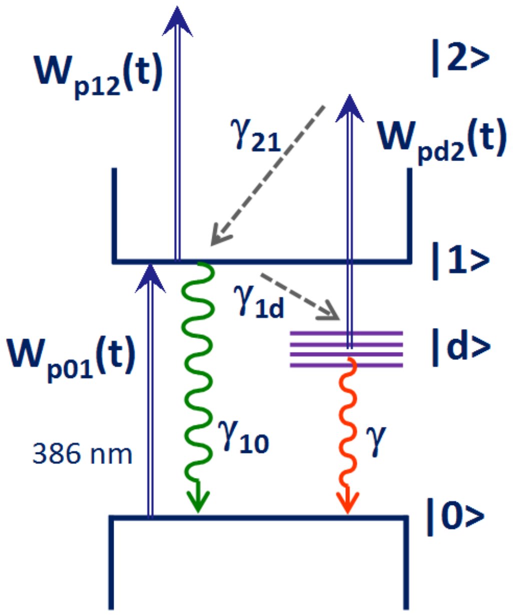

Fig. 5.13 –Scheme of the energy levels proposed to explain the OL behavior of the GC-SNN (see text).

1) be excited to higher energy levels inside the conduction band (state $\left|2\right\rangle$) at a pump rate $W_{p12}(t) = \sigma_{12} I(t)/h\nu_p$, where $\sigma_{12}$ is the absorption cross-section from state $\left|1\right\rangle$ to $\left|2\right\rangle$; 2) Decay radiatively to the state $\left|0\right\rangle$, at a rate $\gamma_{10}$; 3) relax nonradiatively to trap states (defects) $\left|d\right\rangle$ at a rate $\gamma_{1d}$. The population in state $\left|2\right\rangle$ can decay nonradiatively to the bottom of the conduction band (intraband process) with a rate $\gamma_{21}$. The population in state $\left|d\right\rangle$ can be either excited to $\left|2\right\rangle$ at a pump rate $W_{pd2}(t) = \sigma_{d2} I(t)/h\nu_p$ or decay to state $\left|0\right\rangle$ at a global rate $\gamma$. The whole process can be described by a set coupled rate equations as

$$\begin{aligned}
\dot{n}_0 &= -W_{p01}(t)n_0 + \gamma_{10}n_1 + \gamma n_d \\
\dot{n}_1 &= W_{p01}(t)n_0 - \left[\gamma_{10} + \gamma_{1d} + W_{p12}(t)\right]n_1 + \gamma_{21}n_2 \\
\dot{n}_2 &= W_{p12}(t)n_1 + W_{pd2}(t)n_2 - \gamma_{21}n_2 \\
\dot{n}_d &= \gamma_{1d}n_1 - \left[W_{pd2}(t) + \gamma\right]n_d
\end{aligned} \tag{5.7}$$

where $n_i$ is the population in level $\left|i\right\rangle$ ($i$ = 0, 1, 2, $d$) and satisfies $\sum_i n_i = 1$. The excitation intensity along the sample can be expressed as

$$\frac{\partial I(z,t)}{\partial z} = -\left[\alpha_0 + \sigma_{12}n_1(t) + \sigma_{d2}n_d(t)\right]I(z,t) = -\alpha_{eff}(t)I(z,t) \tag{5.8}$$

Integrating eq. (5.8) along the sample thickness $L$, furnishes the transmitted intensity:

$$I(z=L,t)=I(z=0)(1-R)^2\exp\left[-\alpha_{eff}(t)L\right] \tag{5.9}$$

The time-dependence of the transmitted intensity is incorporated in the effective absorption coefficient $\alpha_{eff}(t)$. The set of coupled equations (5.7) was solved using the Runge-Kutta method (see appendix B for source code written in Mathcad) to obtain the time dependent population of levels $|1\rangle$ and $|d\rangle$. The results are then plugged into eqs. (5.8)-(5.9) to obtain the transmitted intensity. The femtosecond pulses are assumed to have a top-hat temporal shape in the model with temporal duration equal to 100 fs. In the Mathcad algorithm, the equations (5.7) were solved in steps of 10 fs during the time the pulses irradiate the sample, in order to include excited state absorption induced by a single pulse, and steps of 100 ps between consecutive pulses.

To numerically solve eqs. (5.7), the absorption cross-sections and decay rates must be properly introduced. The absorption cross-sections $\sigma_{01}$ were obtained from the linear absorption spectra of the samples via the usual relation $\sigma = \alpha/\rho_{en}$ , where $\rho_{en}$ is the volume density of absorbing entities, which is obtained by averaging both the silicate-based matrix and $NaNbO_3$ molar masses, with weigths *f* and (1-*f*) respectively and using the known mass densities $\rho_m$ (table 5.1) of the samples. Typical values of $\sigma_{01}$ were $10^{-22}$ cm$^2$. The excited state absorption cross-sections $\sigma_{12}$ and $\sigma_{d2}$ were estimated with basis on OL experiments reported in [Ol07] using nanosecond pulses in the visible, and the results of the femtosecond transient absorption experiment in this chapter. In [Ol07], the optical limiting behavior was explained by the contribution of two-photon absorption and ESA. For $\sigma_{ESA}$, based on their theoretical model, values on the order of $10^{-18}$ cm$^2$ were obtained. The ESA is equivalent to the transition $|1\rangle$ - $|2\rangle$ in the scheme proposed in fig. 5.13. Here, as we are using femtosecond pulses, $\sigma_{12}$ should be smaller than $\sigma_{ESA}$. However, this decrease in the ESA absorption cross-section is partially compensated by the fact that higher-energy photons are used in the experiment here, resonant with a region of higher density of states in the conduction band. Hence we estimate $\sigma_{12}$ ~ $10^{-20}$ cm$^2$. For $\sigma_{d2}$, the results of transient absorption (TA) in Fig. 5.4 show that the slower component of TA is at least one order of magnitude smaller than the fast component (which is described by $\sigma_{12}$). Hence we assumed $\sigma_{d2}$~ $10^{-22}$ cm$^2$ for the higher doped sample and $\sigma_{d2}$~ $10^{-23}$ cm$^2$ for the undoped sample, since the density of defects is expected to be higher for the doped samples due to the presence dangling bonds in the surface of the nanocrystals.

The relaxation rates were estimated with basis on the luminescence experiments reported in chapter 3 and the TA experiment of this chapter. $\gamma_{10}$ represents the direct exciton recombination whose lifetime is ~ 25 ns and hence $\gamma_{10}$ ~ 4x10$^{7}$ s$^{-1}$. The intraband relaxation rate $\gamma_{21}$ is typically on the order of 10$^{12}$ s$^{-1}$. The decay of the strong ESA signal in Fig. 5.4 implies $\gamma_{1d}$ ~ 10$^{12}$ s$^{-1}$. The decay rate of the trap states from the luminescence experiments at 60 K is $\gamma$ = (500 ns)$^{-1}$ = 4x10$^{6}$ s$^{-1}$ for the doped S206 sample. At room temperature, we expect this decay rate is increased due to thermal activation of nonradiative channels. Furthermore, other defects states are present, such as the nonbridging oxygen hole centers (NBOHC), which possesses decay times ≈ 15 microseconds [Sk92]. This adds uncertainty to this relaxation lifetime and therefore it is considered the only free parameter of the model.

The results of the fitting procedure are represented by the black lines in Fig. 5.14 for the S206 sample. In all curves, all the parameters were kept the same, except the excitation intensities that changed from curve to curve. A good agreement is seen between the experimental results and the theoretical model. Interestingly, the values for $\gamma$ are on the order of 10$^{4}$ s$^{-1}$, which is two orders of magnitude smaller than the obtained from the luminescence experiments. This is interpreted as an indication of the presence of a deep trap states close to the top of the valence band, which is manifested in our model in a slower decay from state $\left|d\right\rangle$. To verify this hypothesis, luminescence or femtosecond absorption experiments are necessary.

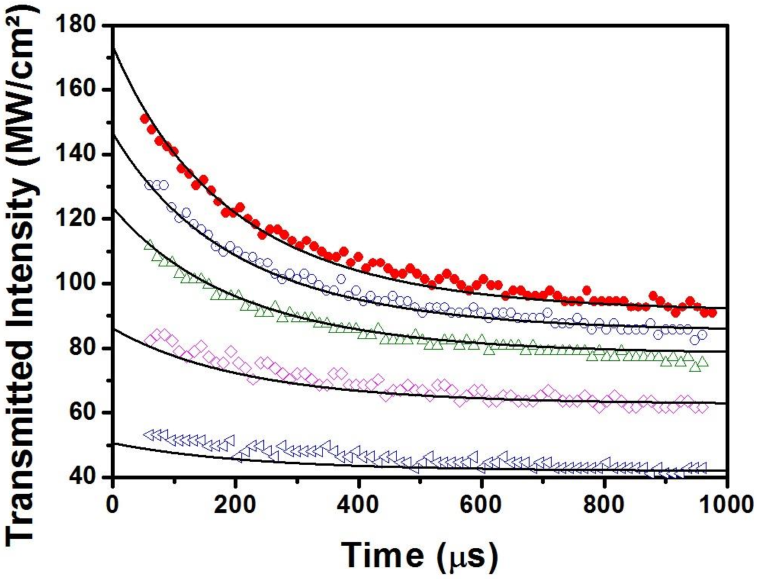

Fig. 5.14 – Theoretical fits based on the rate equations model to the experimental data of fig. 6.2d) (Sample S206) for different excitation intensities.

## 5.4 Conclusions

This chapter was devoted to the investigation of the dynamics of in-gap states in a glass doped with $NaNbO_3$ nanocrystals and charge-transfer dynamics between Rhodamine 590 and $TiO_2$ nanoparticles. Femtosecond pump-probe and dynamical optical limiting were the techniques employed. The femtosecond TA of the GC-SNN revealed a strong ESA signal with at least two different dynamics: a fast one, with decay time approximately 1 ps and a slower component that could not be resolved with our apparatus. Dynamical optical limiting experiment was also performed in this system. The results show that, for near band-gap excitation, the sample presents OL behavior with a slow decay time. The OL behavior was modeled taking into account effects of population accumulation. The set of coupled differential rate equations was numerically solved and the results agreed with the experimental data.

The TA absorption of the Rhodamine 590 functionalized $TiO_2$ nanoparticles shows a bleaching signal that is shortened compared to the bleaching of the free dye in solution. This phenomenon was attributed to charge transfer from the dye to the semiconductor and the back transfer from semiconductor to the dye.

# 6. Conclusions and perspectives

In this thesis, we employed nonlinear optical techniques to investigate ultrafast phenomena arising from the interaction between light and some nanostructured systems.

The basic aspects of nonlinear spectroscopies and the optical techniques employed were presented in chapter 2. The signal generated in a nonlinear spectroscopy is the result of the convolution between the material response function and the applied electric fields. Therefore, this signal carries information about the incident fields and the optical properties of material and dynamical contents hidden in linear spectroscopies can be extracted from the nonlinear ones. The diagrammatic perturbation theory was presented. The double-sided diagrams are particularly useful for keeping track of the temporal evolution of the density matrix when several time-delayed electric fields are applied. Finally, some nonlinear optical techniques were discussed, such as photon echoes, pump and probe and spectral *hole-burning* as well as how information can extracted from these techniques.

Ultrafast dephasing of excitons in a glass-ceramic containing sodium niobate nanocrystals was investigated in chapter 3 as well as the luminescence properties of excitons and trap-states in this material. The measured ultrafast dephasing time ($T_2$ = 20 fs) indicates that several different mechanisms contribute altogether to the exciton decoherence. Unfortunately, under the conditions of our experiment, it was not possible to separate the individual contribution of these mechanisms. Low-temperature luminescence experiments were also performed. The estimated exciton recombination time in the $NaNbO_3$ nanocrystals is 25 ns. A luminescence band centered in 540 nm was attributed to emission from defect states on the nanocrystals surface. The lifetime of this emission was estimated to be 500 ns. Interestingly, the undoped material presents, at low temperatures, a strong luminescence band in approximately 640 nm. This band is attributed to nonbridiging oxygen hole centers (NBOHC) present in this material. The presence of NBOHC contributes to the enhanced optical limiting behavior of this material in the visible. This information was missing in the optical limiting experiments in these samples reported in the literature.

In chapter 4, ultrafast dephasing of localized surface plasmons in colloidal silver nanoparticles capped with different stabilizing molecules was investigated using the persistent spectral hole burning technique. The dephasing times measured are shorter than the one calculated using the bulk values for the dielectric function of the metal. The increased dephasing was attributed to the interaction of the coherently oscillating electrons with the nanoparticles' surface. Two mechanisms were proposed for the this effect: 1) Chemical interface damping (CID), which is manifested by a dynamic charge transfer between the metal and the capping molecules and 2) increased Landau damping i.e., damping of the LSPs in broadened electron and holes eingenstates near the nanoparticles surface. The PSHB technique cannot separate the relative contribution of both mechanisms. Density functional theory calculations were performed to investigate the interaction between the metallic clusters and the adsorbates. Relevant transitions for CID were identified and the calculations revealed that the electronic local density of states on the metal changes with the stabilizer. Therefore, the Landau damping contribution may also evolve with the stabilizer.

Several interesting questions are unresolved concerning the dephasing dynamics of LSPs. One of them is the relative contributions of CID and Landau damping. Up to this work, there was no direct measurement of the dynamical charge transfer during the plasmon excitation. This is particularly challenging as it occurs during almost one optical cycle. One possibility to proof the charge transfer between the molecule and the metal would involve the combined use of ultrashort visible pulses for plasmons excitation and attosecond probe pulses to track electrons motion in the stabilizing molecules. This kind of experiment would also be important to understand the chemical effect of surface enhanced Raman scattering.

Another interesting open problem is the solvent contribution to the CID effect. To this end, experiments in colloidal metallic nanopartciles in different solvents are necessary. An unresolved problem is whether the Marcus charge transfer theory, the dominant model of charge transfer between molecules, would be applied to find the charge transfer rate between the molecule and the metal, and hence the the LSPs dephasing rate.

The experiments to verify the dynamical effects proposed above require systematic variation of the environment of the metal nanoparticles. Single-particle techniques are suitable for eliminating inhomogenous broadening however, to avoid substrate contribution to the LSPs properties, performing experiments in free nanoparticles in solution are mandatory. This is challeging since the Brownian motion of the nanoparticles adds extra noise to the measurement. A solution would be the use for example of an anti-Brownian electrokinetic trap [Co06] to study individual metallic nanoparticles.

In principle, quantum chemical calculations are able to completely calculate the plasmon resonance of metallic nanoparticles taking into account the contribution of the environment and of the capping molecules. Large computational resources are necessary to increase the number of atoms of a metallic cluster and obtain accurate results.

In chapter 5, we applied femtosecond pump-probe and dynamical optical limiting to investigate excited states dynamics in the GC-SNN. A strong ESA signal was verified. This ESA signal decays in at least two different time scales, the faster decay (~1ps), associated with excitation of levels near the bottom of the conduction band and a slower decay whose characteristic time could not be measured with our apparatus. The slower decay was attributed to ESA of electrons in deep trap states. The dynamical optical limiting experiment employed a train of femtosecond pulses and revealed a time-dependent OL behavior. The dynamics of this OL effect reflects the dynamics of the populations in the energy levels of this system. The OL was modeled by a set of coupled differential rate equations that were numerically solved to test our model. The numerical results agree very well with the experimental data. The model is general and can be applied to other multilevel systems excited by a train of femtosecond pulses.

Also in chapter 5, femtosecond pump-probe transient absorption was applied to investigate charge transfer between rhodamine 590 and amorphous $TiO_2$ nanoparticles linked to them. The bleaching signal of the rhodamine absorption is altered by the presence of the semiconductor nanoparticles, which is an evidence of charge transfer. The bleaching signal was fitted by single exponential functions and the rate of charge transfer was estimated to be on the order of $10^9$ $s^{-1}$. This rate could be increased, for example, by linking the dye to crystalline, instead of amorphous, $TiO_2$ particles. A possible application of $TiO_2$ functionalization by Rhodamine 590 is the photodegradation of pollutants, since Rhodamine 590 is a carcinogenic dye.

# Publications and presentations at conferences

Part of the content of this thesis has been published in the following papers:

1. Luminescence and optical dephasing in a glass-ceramic containing sodium-niobate nanocrystals. **E. Almeida**, L. de S. Menezes, Cid B. de Araújo, A. A. Lipovskii. Journal of Applied Physics 109, 113108 (2011). DOI: 10.1063/1.3596518. **Selected for publication in *Virtual Journal of Ultrafast Science*, Vol. 10, Issue 7 (2011).**

2. Ultrafast dephasing of localized surface plasmons in colloidal silver nanoparticles: the influence of stabilizing agents. **E. Almeida**, A. C. L. Moreira, A. M. Brito-Silva, A. Galembeck, C. P. de Melo, L. de S. Menezes, Cid. B. de Araújo. Applied Physics B 108, 9 (2012). DOI: 10.1007/s00340-012-5057-y.

Submitted and in preparation,

3. Dynamical optical limiting in the UV-blue in a silica niobic matrix hosting sodium niobate nanocrystals. **E. Almeida**, K. C. Jorge, L. de S. Menezes, Cid B. de Araújo, A. A. Lipovskii. **(submitted)**

4. Ultrafast excited state absorption in glass-ceramics containing sodium niobate nanocrystals. **E. Almeida**, L. de S. Menezes, Cid B. de Araújo, A. A. Lipovskii.

5. Charge transfer dynamics from Rhodamine 6G linked to amorphous $TiO_2$ particles. **E. Almeida**, A. M. Brito-Silva, A. F. da Silva, G. Machado, L. de S. Menezes, Cid B. de Araújo.

Conference proceedings:

1. Ultrafast dephasing time measurements in a niobic-silicate nanocomposite using incoherent light. **Euclides C. L. Almeida**, Leonardo de S. Menezes, Cid B. de Araújo, A. A. Lipovskii. In Advances in Optical Materials OSA Technical Digest (CD) (Optical Society of America 2009), paper AThC5.

2. Dephasing relaxation of localized surface plasmons investigated by persistent hole burning: role of stabilizing molecules in nanocolloids. L. de S. Menezes, **E. Almeida**, A. C. L. Moreira,

A. M. Brito-Silva, C. B. de Araújo. In CLEO/Europe and EQEC 2011 Conference Digest, OSA Technical Digest (CD) (Optical Society of America, 2011), paper CE_P37.

3. Ultrafast dephasing of surface plasmons in silver nanoparticles: the role of capping agents. **E. Almeida**, A. C. L. Moreira, A. M. Brito-Silva, L. de S. Menezes, A. Galembeck, C. B. de Araújo. In *Laser Science,* OSA Technical Digest (Optical Society of America, 2011), paper LWJ2.

Presentations in international conferences:

1. Ultrafast dephasing of surface plasmons in silver nanoparticles: the role of capping agents. **E. Almeida**, A. C. L. Moreira, A. M. Brito-Silva, L. de S. Menezes, A. Galembeck, C. B. de Araújo. 95th Frontiers in Optics/Laser Science XXVII, San Jose/CA (2011). **(Oral)**

2. Ultrafast dephasing time measurements in a niobic-silicate nanocomposite using incoherent light. **Euclides C. L. Almeida**, Leonardo de S. Menezes, Cid B. de Araújo, A. A. Lipovskii. ***Advances in Optical Materials***/93rd Frontiers in Optics/Laser Science XXV, San Jose/CA (2009). **(Oral)**

3. Damping of localized surface plasmon resonance in colloidal silver nanoparticles. **E. Almeida**, A.C. L. Moreira, A. M. Brito-Silva, L. de S. Menezes, Cid B. de Araújo. 2nd International Workshop on Fundamentals of Light-Matter Interaction, Porto de Galinhas, Brazil (2011). **(Poster) – Best Poster Prize.**

4. Ultrafast dephasing of localized surface plasmons in colloidal silver nanoparticles: the role of capping agents. **E. Almeida**, A. C. L. Moreira, A. M. Brito-Silva, L. de S. Menezes, A. Galembeck, C. P. de Melo, Cid B. de Araújo. 3rd International OSA network of Students-NA/Stanford, Stanford/CA (2011). **(Poster)**

5. Dephasing relaxation of localized surface plasmons investigated by persistent hole burning: role of stabilizing molecules in nanocolloids. L. de S. Menezes, **E. Almeida**, A. C. L. Moreira, A. M. Brito-Silva, C. B. de Araújo. CLEO/Europe 2011, Munich, Germany **(2011)**. **(Poster)** – Presented by L. de S. Menezes.

Presentations in national conferences:

6. Ultrafast dephasing time measurements at low temperatures in a glass-ceramic containing sodium niobate nanocrystals. **E. C. L. Almeida**, L. de S. Menezes, Cid B. de Araújo, A. A. Lipovskii. XXVII Encontro de Físicos do Norte e Nordeste, Belém, Brazil (2009). **(Oral)**

7. Dynamical optical limiting in the blue in a transparent glass ceramic containing sodium niobate nanocrystals. L. de S. Menezes, **E. Almeida**, Cid B. de Araújo, A. A. Lipovskii. XXXV Brazilian Meeting on Condensed Matter Physics, Águas de Lindóia, Brazil (2012). **(Oral)** – Presented by L. de S. Menezes.

8. Femtosecond optical measurements in a niobic-silicate nanocomposite. **E. Almeida**, L. de S. Menezes, Cid B. de Araújo, A. A. Lipovskii. XXXII Brazilian Meeting on Condensed Matter Physics, Águas de Lindóia, Brazil (2009). **(Poster)**

# A. Derivation of equation (3.10)

The double-sided Feynman diagrams that contribute to the DFWMIL signal are presented in fig. 3.1 The analytic form of the pair of diagrams $R_1$-$R_2$ and $R_3$-$R_4$ are equal for a two-level system. Therefore, it is necessary to calculate only the analytic form of diagrams $R_2$ and $R_3$:

$$R_2(\tau_3,\tau_2,\tau_1) \propto \exp\left[\left(-\frac{1}{T_2}-i\omega_{10}\right)\tau_1\right]\exp\left(-\frac{\tau_2}{T_1}\right)\exp\left[\left(-\frac{1}{T_2}+i\omega_{10}\right)\tau_3\right]= \\ \exp\left(-\frac{\tau_2}{T_1}\right)\exp\left[\left(-\frac{1}{T_2}-i\omega_{10}\right)(\tau_1+\tau_3)\right] ,$$

(A.1.1a)

$$R_3(\tau_3,\tau_2,\tau_1) \propto \exp\left[\left(-\frac{1}{T_2}+i\omega_{10}\right)\tau_1\right]\exp\left(-\frac{\tau_2}{T_2}\right)\exp\left[\left(-\frac{1}{T_2}+i\omega_{10}\right)\tau_3\right]= \\ \exp\left(-\frac{\tau_2}{T_1}\right)\exp\left[-\frac{\tau_1+\tau_3}{T_2}\right]\exp\left[\left(-\frac{1}{T_2}+i\omega_{10}\right)(\tau_1-\tau_3)\right] .$$

(A.1.1b)

The third-order nonlinear polarization is given by

$$P^{(3)}(t)=\int_0^\infty d\tau_3\int_0^\infty d\tau_2\int_0^\infty d\tau_1 \\ E(t-\tau_3)E(t-\tau_3-\tau_2)\ldots E(t-\tau_3-\tau_2-\tau_1)R^{(3)}(\tau_3,\tau_2,\tau_1) , \quad \text{(A.1.2)}$$

where the electric field is the superposition of the fields of beams $\boldsymbol{k}_1$ and $\boldsymbol{k}_2$ crossing the sample,

$$E(t)=\tilde{E}(t+\tau)\exp\{-i[\omega(t+\tau)-\boldsymbol{k}_1\cdot\boldsymbol{r}]\}+\tilde{E}(t)\exp[-i(\omega t-\boldsymbol{k}_2\cdot\boldsymbol{r})] \quad \text{(A.1.3)}$$

We assumed $\tau > 0$ when $\boldsymbol{k}_1$ precedes $\boldsymbol{k}_2$. Then, in the $\boldsymbol{k}_3 = 2\boldsymbol{k}_2 - \boldsymbol{k}_1$ direction,

$$\begin{aligned}
P^{(3)}(t,\tau) \propto\ & \exp\{i(2\boldsymbol{k}_2-\boldsymbol{k}_1)\cdot\boldsymbol{r}\}\int_0^\infty d\tau_3\tilde{E}(t-\tau_3)\exp[-i\omega(t-\tau_3)]\int_0^\infty d\tau_2 \exp\left(-\frac{\tau_2}{T_1}\right)\int_0^\infty d\tau_1 \\
& \{\tilde{E}^*(t-\tau_3-\tau_2+\tau)\tilde{E}(t-\tau_3-\tau_2-\tau_1)\times \\
& \exp\left[\left(-\frac{1}{T_2}-i\omega_{10}\right)(\tau_1+\tau_3)\right]\exp[i\omega(t-\tau_3-\tau_2+\tau)]\exp[-i\omega(t-\tau_3-\tau_2-\tau_1)]+ \\
& \tilde{E}(t-\tau_3-\tau_2)\tilde{E}^*(t-\tau_3-\tau_2-\tau_1+\tau)\times \\
& \exp\left(-\frac{\tau_1+\tau_3}{T_2}\right)\exp[i\omega_{10}(\tau_1+\tau_3)]\exp[-i\omega(t-\tau_3-\tau_2)]\exp[i\omega(t-\tau_3-\tau_2-\tau_1+\tau)]\}
\end{aligned} \tag{A.1.4}$$

and therefore,

$$\begin{aligned}
P^{(3)}(t,\tau) \propto\ & \exp\{i[(2\boldsymbol{k}_2-\boldsymbol{k}_1)\cdot\boldsymbol{r}+\omega\tau]\}\int d(\Delta\omega)g(\omega-\omega_{10})\int_0^\infty d\tau_3\tilde{E}(t-\tau_3)\int_0^\infty d\tau_2 \exp\left(-\frac{\tau_2}{T_1}\right)\int_0^\infty d\tau_1 \\
& \{\tilde{E}^*(t-\tau_3-\tau_2+\tau)\tilde{E}(t-\tau_3-\tau_2-\tau_1)\exp\left\{\left[-\frac{1}{T_2}-i(\omega-\omega_{10})\right](\tau_1+\tau_3)\right\}+ \\
& \tilde{E}(t-\tau_3-\tau_2)\tilde{E}^*(t-\tau_3-\tau_2-\tau_1+\tau)\exp\left(-\frac{\tau_1+\tau_3}{T_2}\right)\exp[-i(\omega-\omega_{10})(\tau_1-\tau_3)]\}
\end{aligned} \tag{A.1.5}$$

where we have averaged over the distribution function of the transition frequencies $g(\omega-\omega_{10})$. Now we assume that the population relaxation time is much larger than both the dephasing and correlation time of the light. Also, we will assume extreme inhomogeneous broadening, such that $g(\omega-\omega_{10})$ is a constant over the entire spectrum. Performing the integration over $\Delta\omega$, we get

$$\begin{aligned}
P^{(3)}(t,\tau) \propto\ & \exp\{i[(2\boldsymbol{k}_2-\boldsymbol{k}_1)\cdot\boldsymbol{r}+\omega\tau]\}\int_0^\infty d\tau_3\tilde{E}(t-\tau_3)\int_0^\infty d\tau_2\int_0^\infty d\tau_1 \\
& \{\tilde{E}^*(t-\tau_3-\tau_2+\tau)\tilde{E}(t-\tau_3-\tau_2-\tau_1)\exp\left(-\frac{\tau_1+\tau_3}{T_2}\right)\delta(\tau_1+\tau_3)+ \\
& \tilde{E}(t-\tau_3-\tau_2)\tilde{E}^*(t-\tau_3-\tau_2-\tau_1+\tau)\exp\left(-\frac{\tau_1+\tau_3}{T_2}\right)\delta(\tau_1-\tau_3)\}
\end{aligned} \tag{A.1.6}$$

After integration in $\tau_1$, the first parcel in the integrand is null except for $\tau_1=\tau_3=0$. After integration in $\tau_3$, this term vanishes. Thus

$$P^{(3)}(t,\tau) \propto \exp\{i[(2\boldsymbol{k}_2 - \boldsymbol{k}_1)\cdot \boldsymbol{r} + \omega\tau]\} \int_0^\infty d\tau_3 \tilde{E}(t-\tau_3) \int_0^\infty d\tau_2 \\ \tilde{E}(t-\tau_3-\tau_2)\tilde{E}^*(t-\tau_3-\tau_2-\tau_3+\tau)\exp\left(-\frac{2\tau_3}{T_2}\right) . \tag{A.1.7}$$

Integrating over $\tau_3$ it furnishes

$$P^{(3)}(t,\tau) \propto \exp\{i[(2\boldsymbol{k}_2 - \boldsymbol{k}_1)\cdot \boldsymbol{r} + \omega\tau]\} \int_0^\infty d\tau_3 \tilde{E}(t-\tau_3) G(\tau_3-\tau)\exp\left(-\frac{2\tau_3}{T_2}\right), \tag{A.1.8}$$

where $G(\tau') \equiv \int \tilde{E}(t)\tilde{E}^*(t-\tau')dt$ is the autocorrelation function of the electric field amplitude. The integrated intensity of the signal is given by

$$I(\tau) \propto \int_{-\infty}^{\infty} dt \left\langle P^{(3)}(t,\tau)\left[P^{(3)}(t,\tau)\right]^* \right\rangle, \tag{A.1.9}$$

where $\langle\ \rangle$ denotes the statistical average over the statistical process. Therefore:

$$I(\tau) \propto \int_0^\infty d\tau_3 \int_0^\infty d\sigma_3 G(\sigma_3-\tau_3) G(\tau_3-\tau) G^*(\sigma_3-\tau)\exp\left[-\frac{2(\tau_3+\sigma_3)}{T_2}\right] \tag{A.1.10}$$

and it is independent of the statistics of the light field.

# B. Source code in Mathcad® for solving rate equations (5.6)

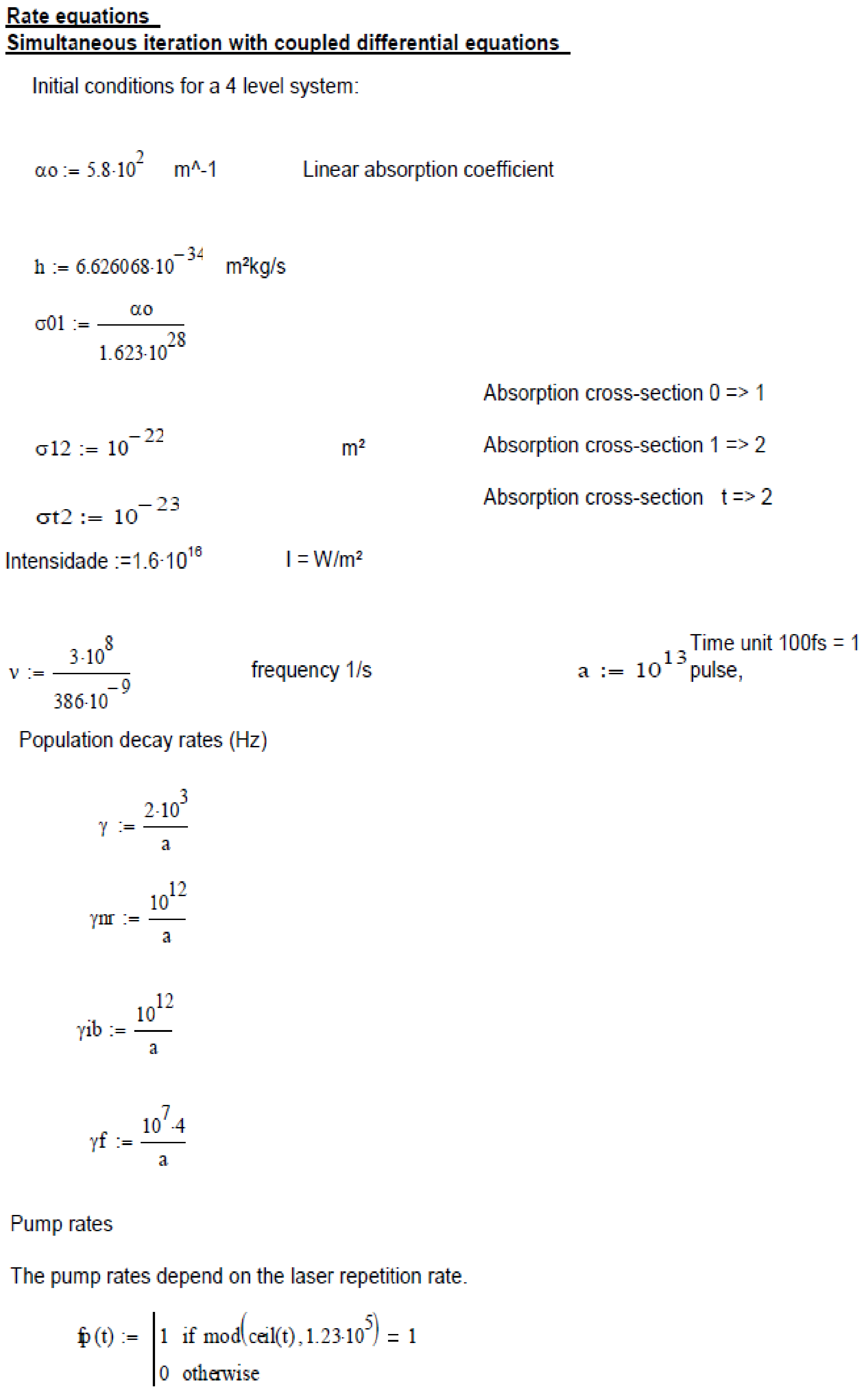

**Rate equations**
**Simultaneous iteration with coupled differential equations**

Initial conditions for a 4 level system:

$\alpha o := 5.8 \cdot 10^{2}$ m^-1 Linear absorption coefficient

$h := 6.626068 \cdot 10^{-34}$ m²kg/s

$\sigma 01 := \dfrac{\alpha o}{1.623 \cdot 10^{28}}$

Absorption cross-section 0 => 1

$\sigma 12 := 10^{-22}$ m² Absorption cross-section 1 => 2

$\sigma t2 := 10^{-23}$ Absorption cross-section t => 2

Intensidade $:= 1.6 \cdot 10^{16}$ I = W/m²

$\nu := \dfrac{3 \cdot 10^{8}}{386 \cdot 10^{-9}}$ frequency 1/s

$a := 10^{13}$ Time unit 100fs = 1 pulse,

Population decay rates (Hz)

$\gamma := \dfrac{2 \cdot 10^{3}}{a}$

$\gamma nr := \dfrac{10^{12}}{a}$

$\gamma ib := \dfrac{10^{12}}{a}$

$\gamma f := \dfrac{10^{7} \cdot 4}{a}$

Pump rates

The pump rates depend on the laser repetition rate.

$$fp(t) := \begin{cases} 1 & \text{if } \mathrm{mod}\left(\mathrm{ceil}(t), 1.23 \cdot 10^{5}\right) = 1 \\ 0 & \text{otherwise} \end{cases}$$

$$\mathrm{wp01}(t) := \frac{\frac{\sigma 01 \cdot \mathrm{intensidade}}{h \cdot \nu}}{a} \cdot \mathrm{fp}(t)$$

$$\mathrm{wp12}(t) := \frac{\frac{\sigma 12 \cdot \mathrm{intensidade}}{h \cdot \nu}}{a} \cdot \mathrm{fp}(t)$$

$$\mathrm{wpt2}(t) := \frac{\frac{\sigma t2 \cdot \mathrm{intensidade}}{h \cdot \nu}}{a} \cdot \mathrm{fp}(t)$$

Coupled differential equation system:

$$D(t,y) := \begin{bmatrix} -\mathrm{wp01}(t)\, y_0 + \gamma f \cdot y_1 + \gamma \cdot y_3 \\ \mathrm{wp01}(t) \cdot y_0 - (\gamma + \gamma nr + \mathrm{wp12}(t)) \cdot y_1 + \gamma ib \cdot y_2 \\ \mathrm{wp12}(t) \cdot y_1 + \mathrm{wpt2}(t) \cdot y_3 - \gamma ib \cdot y_2 \\ \gamma nr \cdot y_1 - (\mathrm{wpt2}(t) + \gamma) \cdot y_3 \end{bmatrix}$$

$ci := \begin{pmatrix} 1 \\ 0 \\ 0 \\ 0 \end{pmatrix}$ => initial conditions

$t1 := 0$ Initial time

$t2 := 1.22 \cdot 10^5$ final time

$num := t2$ number of steps up to the next pulse

$$S := \mathrm{Bulstoer}(ci, t1, t2, num, D)$$

$t := S^{\langle 0 \rangle}$ $n1 := S^{\langle 2 \rangle}$ $nt := S^{\langle 4 \rangle}$

$n0 := S^{\langle 1 \rangle}$ $n2 := S^{\langle 3 \rangle}$

Results are stored in a table, where each column refers to the time from level 0 to 4.

maxx := 82000 Maximum number of pulses

Routine to calculate all the pulses in the experimente and store in .dat files

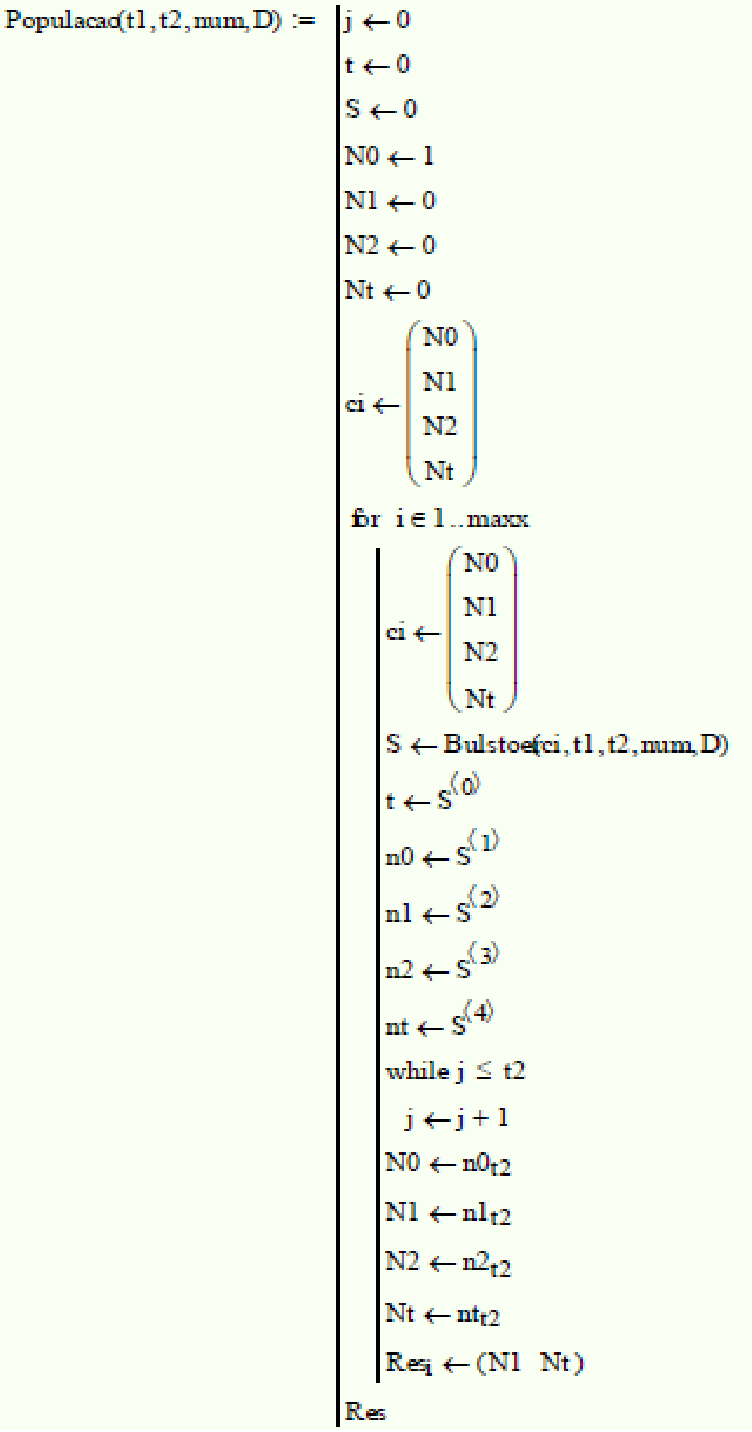

```
$Populacao(t1, t2, num, D) :=$
    $j \leftarrow 0$
    $t \leftarrow 0$
    $S \leftarrow 0$
    $N0 \leftarrow 1$
    $N1 \leftarrow 0$
    $N2 \leftarrow 0$
    $Nt \leftarrow 0$
    $ci \leftarrow \begin{pmatrix} N0 \\ N1 \\ N2 \\ Nt \end{pmatrix}$
    for $i \in 1..maxx$
        $ci \leftarrow \begin{pmatrix} N0 \\ N1 \\ N2 \\ Nt \end{pmatrix}$
        $S \leftarrow Bulstoer(ci, t1, t2, num, D)$
        $t \leftarrow S^{\langle 0 \rangle}$
        $n0 \leftarrow S^{\langle 1 \rangle}$
        $n1 \leftarrow S^{\langle 2 \rangle}$
        $n2 \leftarrow S^{\langle 3 \rangle}$
        $nt \leftarrow S^{\langle 4 \rangle}$
        while $j \le t2$
            $j \leftarrow j + 1$
        $N0 \leftarrow n0_{t2}$
        $N1 \leftarrow n1_{t2}$
        $N2 \leftarrow n2_{t2}$
        $Nt \leftarrow nt_{t2}$
        $Res_i \leftarrow (N1 \;\; Nt)$
    $Res$
```

$i := 1..maxs$

$PP := Populacao(t1, t2, num, D)$

$d1_i := \left| \left( PP_i \right)^{\langle 0 \rangle} \right|$ $dt_i := \left| \left( PP_i \right)^{\langle 1 \rangle} \right|$

$dt := round(dt, 15)$

$d1 := round(d1, 15)$

# References

[Ab66] Photon Echoes: I. D. Abella, N. A. Kurnit, S. R. Hartmann. Physical Review 141, 391 (1966).

[Ac89] Não-Linearidades Óticas em Nanocristais de Cd(S,Se): Lúcio H. Acioli. Ph.D. thesis. Universidade Federal de Pernambuco (1989).

[Al10a] Optical Applications of Glass-ceramics: I. Alekseeva, O. Dymshits, M. Tsenter, A. Zhilin, V. Golubkov, I. Denisov, N. Skoptsov, A. Malyarevich, K. Yumashev. Journal of Non-Crystalline Solids 356, 3042 (2010).

[Al10b] Effect of Ligands on Thermal Dissipation from Gold Nanorods: J. Alpert, K. Hammad-Schifferli. Langmuir 26, 3786 (2010).

[Am11] Nanoestruturas Plasmônicas para Ótica não-linear: Anderson M. Amaral. M.Sc. dissertation. Universidade Federal de Pernambuco (2011).

[An05] Ultrafast Electron Transfer at the Molecule-Semiconductor Nanoparticle Interface: N. A. Anderson, T. Lian. Annual Review of Physical Chemistry 56, 491 (2005).

[An10] Few-Femtosecond Plasmon Dephasing of a Single Metallic Nanostructure from Optical Response Function Reconstruction by Interferometric Frequency Resolved Optical Gating: A. Anderson, K. S. Deryckx, X. G. Xu, G. Steinmeyer, M. B. Raschke. Nano Letters 10, 2519 (2010).

[Ar03] Electron-Phonon Scattering in Metal Clusters: A. Arbouet, C. Voisin, D. Christofilos, P. Langot, N. Del Fatti, F. Vallée, J. Lermé, G. Celep, E. Cottancin, M. Gaudry, M. Pellarin, M. Broyer, M. Maillard, M. P. Pileni, M. Treguer. Physical Review Letters 90, 177401-1 (2003).

[Ar04] Direct Measurement of the Single-Metal-Cluster Optical Absoption: A. Arbouet, D. Christofilos, N. Del Fatti, F. Vallée, J. R. Huntizinger, L. Arnaud, P. Billaud, M. Broyer. Physical Review Letters 93, 127401 (2004).

[As84] Accumulated Photon Echoes with Incoherent Light in $Nd^{3+}$-doped Silicate Glass: S. Asaka, H. Nakatsuka, M. Fujiwara, M. Matsuoka. Physical Review A 29, 2286 (1984).

[Au10] Plasmonic Light-Harvesting Devices over the Whole Visible Spectrum: A. Aubry, D. Y. Lei, A. I. Fernández-Domínguez, Y. Sonnefraud, S. A. Maier, J. B. Pendry. Nano Letters 10, 2574 (2010).

[Ba09] Quantitative Determination of the Size Dependence of Surface Plasmon Resonance Damping in Single Ag@$SiO_2$ Nanoparticles: H. Baida, P. Billaud, S. Marhaba, D. Christofilos, E. Cottacin, A. Crut, J. Lermé, P. Maioli, M. Pellarin, M. Broyer, N. del Fatti, F. Vallée, A. Sánchez-Iglesias, I. Pastoriza-Santos, L. M. Liz-Marzán, Nano Letters 9, 3463 (2009).

[Be84] Incoherent Photon Echoes: R. Beach, S. R. Hartmann. Physical Review Letters 53, 663 (1984).

[Be88] Femtosecond Photon Echoes from Band-to-Band Transitions in GaAs: P. C. Becker, H. L. Fragnito, C. H. Brito Cruz, R. L. Fork, J. E. Cunningham, J. E. Henry, C. V. Shank. Physical Review Letters 61, 1647 (1988).

[Be99] Nanophase Glass-Ceramics: G. H. Beall, L. R. Pinckney. Journal of American Ceramic Society 82, 5 (1999).

[Be00] Role of Nanoparticles in Photocatalysis: D. Beydoun, R. Amal, G. Low, S. McEvoy. Journal of Nanoparticle Research 1, 439 (1999).

[Be04] Photothermal Heterodyne Imaging of Individual Nonfluorescent Nanoclusters and Nanocrystals: S. Berciaud, L. Cognet, G. A. Blab, B. Lounis. Physical Review Letters 93, 257402 (2004).

[Be05] Observation of Intrinsic Size Effects in the Optical Response of Individual Gold Nanoparticles: S. Berciaud, L. Cognet, P. Tamarat, B. Lounis. Nano Letters 05, 515 (2005)

[Be06] Photothermal Heterodyne Imaging of Individual Metallic Nanoparticles: Theory versus Experiment. Physical Review B 73, 045424 (2006).

[Bi82] Surface Studies by Scanning Tunneling Microscopy: G. Binnig, H. Rohrer, Ch. Gerber, E. Weibel. Physical Review Letters 49, 57 (1982).

[Bi86] Atomic Force Microscope: G. Binnig, C. F. Quate, Ch. Gerber. Physical Review Letters 56, 930 (1986).

[Bi91] Two-dimensional Carrier-Carrier Screening in a Quantum Well: J.-Y. Bigot, M. T. Portella, R. W. Schoenlein, J. E. Cunningham, C. V. Shank. Physical Review Letters 67, 636 (1991).

[Bo83] Absorption and Scattering of Light by Small Particles. C. F. Bohren, D. R. Huffman. Wiley, New York (1983).

[Bo02] Ultrafast Dephasing of Surface Plasmon Excitation in Silver Nanoparticles: Influence of Particle Size, Shape, and Chemical Surrounding: J. Bosbach, C. Hendrich, F. Stietz, T. Vartanyan, F. Träger. Physical Review Letters 89, 257404 (2002).

[Br10] Laser Ablated Silver Nanoparticles with Nearly the Same Size in Different Carrier Media: A. M. Brito-Silva, L. A. Gómez, Cid B. de Araújo, A. Galembeck. Journal of Nanomaterials 2010, 1, (2010).

[Br11] Fabricação e Caracterização de Compósitos Fotônicos Contendo Nanopartículas Dielétricas e Metálicas: Antonio M. Brito-Silva. PhD Thesis. Universidade Federal de Pernambuco (2010).

[Co06] Suppressing Brownian Motion of Individual Biomolecules in Solution: A. E. Cohen, W. E. Moerner. Proceedings of the National Academy of Sciences 103, 4362 (2006).

[Cr02] Characterization of the Interfacial Dipole at Organic/Metal Interfaces: X. Crispin, V. Geskin, A. Crispin J. Cornil, R. Lazzaroni, W. R. Salaneck, J.-L. Brédas: Journal of the American Chemical Society 124, 8131 (2002).

[Da04] Two Photon Absorption and Coherent Control with Broadband Down-Converted Light: B. Dayan, A. Pe’er, A. A. Friesem, Y. Silberberg. Physical Review Letters 93, 023005-1 (2004).

[Da05] Quantum Transport: Atom to Transistor: S. Datta. Cambridge University Press, Cambridge (2005).

[Di08] Gold Nanorod Assisted Near-infrared Plasmonic Photothermal Therapy (PPTT) of Squamous Cell Carcinoma in Mice: E. B. Dickerson, E. C. Dreaden, X. Huang, I. H. El-Sayed, H. Chu, S. Pushpanketh, J. F. McDonald, M. El-Sayed. Cancer Letters 269, 57 (2008).

[Do02] Single-Molecule and Single-Nanoparticle SERS: Examining the Roles of Surface Active Sites and Chemical Enhancement: W. E. Doering, S. Nie. Journal of Physical Chemistry B 106, 311 (2002).

[Du91] Radiation-Matter Oscillations and Spectral Line Narrowing in Field-Correlated Four-Wave Mixing. I. Theory: M. A. Dugan, A. C. Albrecht. Physical Review A 43, 3877 (1991).

[Du02] Single-Pulse Coherently Controlled Nonlinear Raman Spectroscopy and Microscopy: N. Dudovich, D. Oron, Y. Silberberg. Nature 418, 512 (2002).

[Dr94] Discrete-Dipole Approximation for Scattering Calculations: B. T. Draine, P. J. Flatau. Journal of the Optical Society of America B 11, 1491 (1994).

[Ed85] Handbook of Optical Constants of Solids: D. Edward, I. Palik. Academic Press, Orlando (1985).

[Fa92b] Direct Measurement of Nonequilibrium Electron-Energy Distributions in Subpicosecond Laser-Heated Gold Films: W. S. Fann, R. Storz, H. W. K. Tom, J. Bokor. Physical Review Letters 68, 2834 (1992).

[Fa92a] Electron Thermalization in Gold: W. S. Fann, R. Storz, H. W. K. Tom, J. Bokor. Physical Review B 46, 13592 (1992).

[Fa04] Third-order Optical Nonlinearity of a Transparent Glass Ceramic Containing Sodium Niobate Nanocrystals: E. L. Falcão-Filho, C. A. C. Bosco, G. S. Maciel, L. H. Acioli, Cid B. de Araújo, A. A. Lipovskii, D. K. Tagantsev. Physical Review B 69, 134204 (2004).

[Fe59] "There's plenty of room at bottom". Richard Feynman. http://calteches.library.caltech.edu/47/2/1960Bottom.pdf

[Fe03] Ultrafast Hydrogen-Bond Dynamics in the Infrared Spectroscopy of Water: C. J. Fecko, J. D. Eaves, J. J. Loparo, A. Tokmakoff, P. L. Geissler. Science 301, 1698 (2003).

[Fe05] Quantum Interference in Atomic Vapor Observed by Four-wave Mixing with Incoherent Light: J. Ferraz, D. Felinto, L. H. Acioli, S. S. Vianna. Optics Letters 30, 1876 (2005).

[Fo01] Optical Properties of Solids: M. Fox. Oxford University Press, Oxford (2001).

[Fr04] Gaussian 03, Revision C.02. M. J. Frisch, G. W. Trucks, H. B. Schlegel, G. E. Scuseria, M. A. Robb, J. R. Cheeseman, J. A Montgomery Jr., T. Vreven, K. N. Kudin, J. C. Burant, J. M. Millam, S. S. Iyengar, J. Tomasi, V. Barone, B. Mennucci, M. Cossi, G. Scalmani, N. Rega, G. A. Petersson, H. Nakatsuji, M. Hada, M. Ehara, K. Toyota, R. Fukuda, J. Hasegawa, M. Ishida, T. Nakajima, Y. Honda, O. Kitao, H. Nakai, M. Klene, X. Li, J. E. Knox, H. P. Hratchian, J. B. Cross, V. Bakken, C. Adamo, J. Jaramillo, R. Gomperts, R. E. Stratmann, O. Yazyev, A. J. Austin, R. Cammi, C. Pomelli, J. W. Ochterski, P. Y. Ayala, K. Morokuma, G. A. Voth, P. Salvador, J. J. Dannenberg, V. G. Zakrzewski, S. Dapprich, A. D. Daniels, M. C. Strain, O. Farkas,; D. K. Malick, A. D. Rabuck, K. Raghavachari, J. B. Foresman, J. V. Ortiz, Q. Cui, A. G. Baboul, S. Clifford, J. Cioslowski, B. B. Stefanov, G. Liu, A. Liashenko, P. Piskorz, I. Komaromi, R. L. Martin, D. J. Fox, T. Keith, M. A. Al-Laham, C. Y. Peng, A. Nanayakkara, M. Challacombe, P. M. W. Gill, B. Johnson, W. Chen, M. W. Wong, C. Gonzalez, J. A. Pople, Gaussian, Inc., Wallingford CT, 2004.

[Ga03] Dye-Sensitized Solar Cells: M. Grätzel. Journal of Photochemistry and Photobiology C: Photochemistry Reviews 4, 145, (2003).

[Go89] Dispersion of Coherence Spikes of Incoherent Broadband Dye Lasers: A. S. L. Gomes, L. H. Acioli, Cid B. de Araújo, J. R. Rios Leite. Optics Communications 73, 475 (1989).

[Go07] Influence of Stabilizing Agents on the Nonlinear Susceptibiliy of Silver Nanoparticles: L. A. Gómez, A. M. Brito-Silva, A. Galembeck, Cid B. de Araújo. Journal of the Optical Society of America B 24, 2136 (2007).

[Gr00] Thiols and Disulfides on the Au(111) Surface: The Headgroup-Gold Interaction: H. Grönbeck, A. Curioni, W. Andreoni. Journal of the American Chemical Society 122, 3839 (2000).

[Gr03] Dye-Sensitized Solar Cells: M. Grätzel. Journal of Photochemistry and Photobiology C: Photochemistry Reviews 4, 145 (2003).

[Gr07] Characterisation of a New Sol-Gel Precursor for a $SiO_2$-Rhodamine 6G Hybrid Class II material: S. Grandi, C. Tomasi, P. Mustarelli, F. Clemente, C. M. Carbonaro. Journal of Sol-Gel Science and Technology 41, 57 (2007).

[Ha87] Coherent Stokes Raman Scattering with Incoherent Light for Vibrational-Dephasing-Time Measurement. T. Hattori, A. Terasaki, T. Kobayashi. Physical Review A, 35, 715 (1987).

[Ha06] Coherent Excitation of Vibrational Modes in Metallic Nanoparticles: G. V. Hartland. Annual Review of Physical Chemistry 57, 403 (2006).

[Ha10] Ultrafast Studies of Single Semiconductor and Metal Nanostructures through Transient Absorption Microscopy: G. V. Hartland. Chemical Science 1, 303 (2010).

[Ha11a] Concepts and Methods of 2D Infrared Spectroscopy: P. Hamm, M. Zanni. Cambridge University Press, New York 2011.

[Ha11b] Optical Studies of Dynamics in Noble Metal Nanostructures: G. V. Hartland. Chemical Reviews 111, 3858 (2011).

[Ha12] The Renaissance of Dye-Sensitized Solar Cells: B. E. Hardin, H. J. Snaith, M. D. McGehee. Nature Photonics 6, 162 (2012).

[He03] Chemical Interface Damping of Surface Plasmon Excitation in Metal Nanoparticles: a Study by Persistent Spectral Hole Burning: C. Hendrich, J. Bosbach, F. Stietz, F. Hubenthal, T. Vartanyan, F. Träger. Applied Physics B 76, 869 (2003).

[He07] Toward Control of the Metal-Organic Interfacial Electronic Structure in Molecular Electronics: A First-Principles Study on Self-Assembled Monolayers of $\pi$-Conjugated Molecules on Noble Metals: G. Heimel, L. Romaner, E. Zojer, J.-L. Brédas. Nano Letters 7, 932 (2007)..

[Ho98] Observation of Acoustic Quantum Beats in Nanometer Sized Au Particles: J. H. Hodak, I. Martini, G. V. Hartland. Journal of Chemical Physics 108, 9210 (1998).

[Ho98] Spectroscopy and Dynamics of Nanometer-Sized Noble Metal Particles: J. H. Hodak, I. Martini, G. V. Hartland. Journal of Physical Chemistry B 102, 6958 (1998).

[Hö93] Width of Cluster Plasmon Resonances: Bulk Dielectric Functions and Chemical Interface Damping: H. Hövel, S. Fritz, A. Hilger, U. Kreibig, M. Vollmer. Physical Review B 48, 18178 (1993).

[Hu87] Statistical Mechanics, 2nd Edition: K. Huang. John Wiley & Sons, New York (1987).

[Hu96] Photochemical Formation of Silver Nanoparticles in Poly(*N*-vinylpyrrolidone): H. H. Huang, X. P. Ni, G. L. Loy, C. H. Chew, K. L. Tan, F. C. Loh, J. F. Deng, G. Q. Xu. Langmuir 12, 909 (1996).

[Hu07] Ultrafast Dephasing Time of Localized Surface Plasmon Polariton Resonance and the Involved Damping Mechanisms in Colloidal Gold Nanoparticles: F. Hubenthal. Progress in Surface Science 82, 378 (2007).

[Hu08] Dark-field Microscopy Studies of Single Metal Nanoparticles: Understanding the Factors that Influence the Linewidth of the Localized Surface Plasmon Resonance: M. Hu, C. Novo, A. Funston, H. Wang, H. Staleva, S. Zou, P. Mulvaney, Y. Xia, G. V. Hartland. Journal of Materials Chemistry 18, 1949 (2008).

[Hu10] Damping of Localized Surface Plasmon Polariton Resonance of Gold Nanoparticles: F. Hubenthal, C. Hendrich, F. Träger. Applied Physics B 100, 225 (2010).

[Hu11] Noble Metal Nanoparticles: Synthesis and Optical Properties: F. Hubenthal in Comprehensive Nanoscience and Technology, volume 1, 393ff. Academic Press, Oxford (2011).

[Hu11b] Chemical Damping of the Localized Surface Plasmon Polariton Resonance: Influence of Different Chemical Environments: F. Hubenthal, F. Träger. Proceedings of SPIE 7922, 79220D (2011).

[Ip75] Picosecond Response of a High-Repetition-Rate $CS_2$ Optical Kerr Gate: E. P. Ippen, C. V. Shank. Applied Physics Letters 26, 92 (1975).

[Ja08] DFT Studies on the Phenol and Thiophenol Interaction on an Undecagold Cluster Surface: N. Jayanthi, J. Cruz, T. Pandiyan. Chemical Physics Letters 455, 64 (2008).

[Jo96] Pump-Probe Polarization Anisotropy Study of Femtosecond Energy Transfer Within the Photosynthetic Reaction Center of *Rhodobacter sphaeroides* R26: D. M. Jonas, M. J. Lang, Y. Nagasawa, T. Joo, G. R. Fleming. Journal of Physical Chemistry 100, 12660 (1996).

[Jo97] Heavy-Light Hole Quantum Beats in the Band-to-Band Continuum of GaAs Observed in 20 Femtosecond Pump-Probe Experiments. M. Joschko, M. Woerner, T. Elsaesser, E. Binder, T. Kuhn, R. Hey, H. Kostial, K. Ploog. Physical Review Letters 78, 737 (1997).

[Jo03] Two-dimensional Femtosecond Spectroscopy: D. M. Jonas. Annual Review of Physical Chemistry 54, 425 (2003).

[Ka02] Photophysical, Photochemical and Photocatalytic Aspects of Metal Nanoparticles: P. V. Kamat. Journal of Physical Chemistry B 106, 7729 (2002).

[Ke03] The Optical Properties of Metal Nanoparticles: The Influence of Size, Shape, and Dielectric Environment: K. L. Kelly, E. Coronado, L. L. Zhao, G. C. Schatz. Journal of Physical Chemistry B 107, 668 (2003).

[Ki08] Shape-Controlled Synthesis of Silver Nanoparticles: *Ab initio* Study of Preferential Surface Coordination with Citric Acid: D. S. Kilin, O. V. Prezhdo, Y. Xia. Chemical Physics Letters 458, 113 (2008).

[Kl98] Surface-Plasmon Resonances in Single Metallic Nanoparticles: T. Klar, M. Perner, S. Grosse, G. Von Plessen, W. Spirkl, J. Feldmann. Physical Review Letters 80, 4249 (1998).

[Kl00] Optical Nonlinearities and Ultrafast Carrier Dynamics in Semiconductor Nanocrystals: V. I. Klimov, The Journal of Physical Chemistry B 104, 26 (2000).

[Kn97] Single-Molecule Detection Using Surface-Enhanced Raman Scattering (SERS): K. Kneipp, Y. Wang, H. Kneipp, L. T. Perelman, I. Itzkan, R. R. Dasari, M. S. Feld. Physical Review Letters 78, 1667 (1997).

[Kn09] Substrates Matter: Influence of an Adjacent Dielectric on an Individual Plasmonic Nanoparticle: M. K. Knight, Y. Wu, J. B. Lassiter, P. Nordlander, N. J. Halas. Nano Letters 9, 2188 (2009).

[Ko88] The Application of Incoherent Light for the Study of Femtosecond-Picosecond Relaxation in Condensed Phase: T. Kobayashi, A. Terasaki, T. Hattori, K. Kurokawa. Applied Physics B 47, 107 (1988).

[Ko99] Light-Induced Inhomogeneous Broadening in Dye Solution Probed by Wave-mixing with broadband lasers: V. Kozich, L. de S. Menezes, Cid B. de Araújo. Optics Communications 171, 125 (1999).

[Ko01] A Chemist’s Guide to Density Functional Theory: W. Koch, M. C. Holthausen. Wiley-VCH Verlag GmbH, Weinheim Germany (2001).

[Kr76] Small Silver Particles in Photosensitive Glass: Their Nucleation and Growth: U. Kreibig. Applied Physics 10, 255 (1976).

[Kr95] Optical Properties of Metal Clusters: U. Kreibig, M. Vollmer. Springer, Berlin 1995.

[Ku87] Subpicosecond Molecular Dynamics Studied by Degenerate Four-Wave Mixing with Incoherent Light: K. Kurokawa, T. Hattori, T. Kobayashi. Physical Review A 36, 1298 (1987).

[Ku94] Forced Light Scattering by Broad-Bandwidth Incoherent Pump Lasers: A. Kummrow, S. Woggon, A. Lau. Physical Review A 50, 4264 (1994).

[La97] Femtosecond Decay-Time Measurement of Electron-plasma Oscillation in Nanolithographically Designed Silver Particles: B. Lamprecht, A. Leitner, F. R. Aussenegg. Applied Physics B 64, 269 (1997).

[La99] SHG Studies of Plasmon Dephasing in Nanoparticles: B. Lamprecht, A. Leitner, F. R. Aussenegg. Applied Physics B 68, 419 (1999).

[Le83] Surface-Enhanced Raman Scattering of Colloid-Stabilizer Systems: P. C. Lee, D. Meisel. Chemical Physics Letters 99, 262 (1983).

[Le00] Surface Plasmon Dynamics in Silver Nanoparticles Studied by Femtosecond Time-Resolved Photoemission: J. Lehmann, M. Merschdorf, W. Pfeiffer, A. Thon, S. Voll, G. Gerber. Physical Review Letters 85, 2921 (2000).

[Le10] Electronic Mapping of Molecular Orbitals at Molecule-Metal Interface: M. C. Lennartz, V. Caciuc, N. Atodiresei, S. Karthäuser, S. Blügel. Physical Review Letters 105, 066801 (2010).

[Li99] How Long Does it Take to Melt a Gold Nanorod? A Femtosecond Pump-Probe Absorption Spectroscopy Study: S. Link, C. Burda, B. Nikoobakht, M. A. El-Sayed. Chemical Physics Letters 315, 12 (1998).

[Li00] Femtosecond Transient-Absorption Dynamics of Colloidal Gold Nanorods: Shape Independence of the Electron-Phonon Relaxation Time: S. Link, C. Burda, M. B. Mohamed, B. Nikoobakht, M. A. El-Sayed. Physical Review B 61, 6086 (2000).

[Li01a] Principles and Applications of Ferroelectrics and Related Materials: M. E. Lines, A. M. Glass. Oxford University Press, New York (2004).

[Li01b] Ultrafast Dephasing of Single Nanoparticles Studied by Two-Pulse Second-Order Interferometry: Y-H. Liau, A. N. Unterreiner, Q. Chang, N. F. Scherer. Journal of Physical Chemistry B 105, 2135 (2001).

[Li03a] Optical Properties and Ultrafast Dynamics of Metallic Nanocrystals: S. Link, M. A. El-Sayed. Annual Review of Physical Chemistry 54, 331, (2003).

[Li03b] The Origin of Electrooptical Sensitivity of Glassy Materials: Crystal Motifs in Glasses: A. A. Lipovskii, D. K. Tagantsev, B. V. Tatarintsev, A. A. Vetrov. Journal of Non-Crystalline Solids 318, 268 (2003).

[Li03c] Study of Citrate Adsorbed on the Au(111) Surface by Scanning Probe Microscopy: Y. Lin, G.-B. Pan, G.-J. Su, X.-H. Fang, L.-J. Wan, C.-L. Bai. Langmuir 19, 10000 (2003).

[Li08] Molecularly Mediated Processing and Assembly of Nanoparticles: Exploring the Interparticle Interactions and Structures: S. I. Lim, C-J. Zhong. Accounts of Chemical Research 42, 798 (2009).

[Lo05] Immunotargeted Nanoshells for Integrated Cancer Imaging and Therapy: C. Loo, A. Lowery, N. Halas, J. West, R. Drezek. Nano Letters 5, 709 (2005).

[Lu09] Chemical Synthesis of Novel Plasmonic Nanoparticles: X. Lu, M. Rycenga, S. E. Skrabalak, B. Wiley, Y. Xia. Annual Review of Physical Chemistry 60, 167 (2009).

[Ma85] Electron Transfers in Chemistry and Biology: R. A. Marcus, N. Sutin. Biochimica et Biophysica Acta 811, 265 (1985).

[Ma95] Optical Coherence and Quantum Optics: L. Mandel, E. Wolf. Cambridge University Press, New York (1995).

[Ma98] Effect of Structure on Electron Transfer Reaction between Anthracene Dyes and $TiO_2$ Nanoparticles: I. Martini, J. H. Hodak, G. V. Hartland. Journal of Physical Chemistry B 102, 9508 (1998).

[Ma03] Local Detection of Electromagnetic Energy Transport below the Diffraction Limit in Metal Nanoparticle Plasmon Waveguides: S. A. Maier, P. G. Kik, H. A. Atwater, S. Meltzer, E. Harel, B. E. Koel, A. A. G. Requicha. Nature Materials 2, 229 (2003).

[Ma04] Dinâmica Ultra-Rápida em Nanopartículas Metálicas. Marcio H. G. de Miranda. M.Sc. dissertation. Universidade Federal de Pernambuco (2004).

[Ma05] Plasmonics: Localization and Guiding of Electromagnetic Energy in Metal/dielectric Structures: S. A. Maier, H. A. Atwater. Journal of Applied Physics 98, 011101 (2005).

[Ma07] Plasmonics: Fundamentals and Applications: S. A. Maier. Springer, New York (2007).

[Mc79] Glass-ceramics: P. W. McMillan. 2nd edition. Academic Press, New York (1979).

[Me01] Espectroscopia Não Linear com Luz Incoerente em Moléculas Orgânicas: Leonardo de S. Menezes. Ph.D. thesis, Universidade Federal de Pernambuco (2001).

[Mi94] Quantum Size Dependence of Femtosecond Electronic Dephasing and Vibrational Dynamics in CdSe nanocrystals: D. M. Mittleman, R. W. Schoenlein, J. J. Shiang, V. L. Colvin, A. P. Alivisatos, C. V. Shank. Physical Review B 49, 14435 (1994).

[Mi96] Frequency and Time Resolved Coherent Stokes Raman Scattering in $CS_2$ Using Incoherent Light: M. J. Stimson, D. J. Ulness, A. C. Albrecht. Chemical Physics Letters 263, 185 (1996).

[Mi08] Beiträge zur Optik Trüber Medien, Speziell Kolloidaler Metallösunger. G. Mie. Annalen der Physik 25, 377 (1908).

[Mo84] Ultrahigh-time-resolution coherent transient spectroscopy with incoherent light: N. Morita, Y. Yajima. Physical Review A 30, 2525 (1984).

[Mu95] Principles of Nonlinear Optical Spectroscopies. S. Mukamel. Oxford University Press, New York, 1995.

[Mu01] Synthesis and Characterization of Indium Oxide Nanoparticles: A. Murali, A. Barve, V. J. Leppert, S. H. Risbud, I. M. Kennedy, H. W. H. Lee. Nano Letters 1, 287 (2001).

[Mu08] Optical Extinction Spectrum of a Single Metal Nanoparticle: Quantitative Characterization of a Particle and of its Local Environment: O. L. Muskens, P. Billaud, M. Broyer, N. Del Fatti, F. Vallée. Physical Review B 78, 205410 (2008).

[Na08] Nanoparticles: Synthesis, Stabilization, Passivation, and Functionalization: ed. R. Nagarajan, T. A. Hatton. ACS Symposium Series 996, American Chemical Society (2008).

[Ne69] Self-Consistent Model of Hydrogen Chemisorption: D. M. Newns. Physical Review 178, 1123 (1969).

[No07] Surface Plasmons on Metal Nanoparticles: The Influence of Shape and Physical Environment: C. Noguez. Journal of Physical Chemistry C 111, 3806 (2007).

[Or02] Narrow-Band Coherent Anti-Stokes Raman Signals from Broad-Band Pulses: D. Oron, N. Dudovich, D. Yelin, Y. Silberberg. Physical Review Letters 88, 063004 (2002).

[Ol07] Nonlinear Absorption of Transparent Glass Ceramic Containing Sodium Niobate Nanocrystals: T. R. Oliveira, L. de S. Menezes, Cid B. de Araújo, A. A. Lipovskii. Physical Review B 76, 134207 (2007).

[Ou05] Laser-Assisted Growth of Gold Nanoparticles: Shaping and Optical Characterization: H. Ouacha, C. Hendrich, F. Hubenthal, F. Träger. Applied Physics B 81, 663 (2005).

[Pa95] Density-Functional Theory of the Electronic Structure of Molecules: R. G. Parr, W. Yang. Annual Review of Physical Chemistry 46, 701 (1995).

[Pa01] Highly Simplified Device for Ultrashort-Pulse Measurement: P. O’Shea, M. Kimmel, X. Gu, R. Trebino. Optics Letters 26, 932 (2001)

[Pa07] Single-Shot Two Dimensional Time Resolved Anti Stokes Raman Scattering: Y. Paskover, I. Sh. Averbukh, Y. Prior. Optics Express 15, 1700 (2007).

[Pe93] Polarizability of Small Spherical Particles: Influence of the Matrix Environment: B. N. J. Persson. Surface Science 281, 153 (1993).

[Pe09] Damping of Acoustic Vibrations in Gold Nanoparticles: M. Pelton, John E. Sader, J. Burgin, M. Liu, P. Guyot-Sionnest, D. Gosztola. Nature Nanotechnology 4, 492 (2009).

[Ph75] Subnanosecond Relaxation Time Measurements Using a Transient Induced Grating Method: D. W. Phillion, D. J. Kuizenga, A. E. Siegman. Applied Physics Letters 27, 85 (1975).

[Pi03] Interface Decay Channel of Particle Surface Plasmon Resonance: A. Pinchuk, U. Kreibig. New Journal of Physics 5, 151 (2003).

[Pl03] Time-resolved X-ray Diffraction on Laser-Excited Metal Nanoparticles: A. Plech, S. Kürbitz, K.-J. Berg, H. Graener, G. Berg, S. Grésillon, M. Kaempfe, J. Feldmann, M. Wulff, G. von Plessen. Europhysics Letters 61, 762 (2003).

[Pl04] Laser-Induced Heating and Melting of Gold Nanoparticles Studied by Time-Resolved X-ray Scattering: A. Plech, V. Kotaidis, S. Grésillon, C. Dahmen, G. von Plessen. Physical Review B 70, 195423 (2004).

[Pl06] Femtosecond Laser Near-Field Ablation from Gold Nanoparticles: A. Plech, V. Kotaidis, M. Lorenc, J. Boneberg. Nature Physics 2, 44 (2006).

[Po78] Picosecond Time Resolved Energy Transfer between Rhodamine 6G and Malachite Green: G. Porter, C. J. Tredwell. Chemical Physics Letters 56, 278 (1978).

[Po08] Application of Spectral Phase Shaping to High Resolution CARS Spectroscopy: S. Postma, A. C. W. van Rhijn, J. P. Korterik, P. Gross, J. L. Herek, H. L. Offerhaus. Optics Express 16, 7985 (2008).

[Pr04] Nanophotonics: P. N. Prasad. Wiley, New York (2004).

[Pr07] Numerical Recipes: The Art of Scientific Computing: W. H. Press, S. A. Teukolsky, W. T. Vetterling, B. P. Flannery. Cambridge University Press, Cambrige UK (2007).

[Py07] Synthesis of Spherical Silver Particles with Controllable Sizes in Aqueous Solutions: Journal of Physical Chemistry C 111, 7910 (2007).

[Ra04] Density Functional Theory Study of the Interaction of Monomeric Water with the Ag(111) surface: V. A. Ranea, A. Michaelides, R. Ramírez, J. A. Vergés, P. L. de Andres, D. A. King. Physical Review B 69, 205411 (2004).

[Ro06] Quantum Dot Solar Cells. Harvesting Light Energy with CdSe Nanocrystals Molecularly Linked to Mesoscopic $TiO_2$ Films. I. Robel, V. Subramanian, M. Kuno, P. V. Kamat. Journal of American Chemical Society 128, 2385 (2006).

[Ru07] Dynamics of Size-Selected Gold Nanoparticles Studied by Ultrafast Electron Nanocrystallography: C-Y. Ruan, Y. Murooka, R. K. Raman, R. A. Murdick. Nano Letters 7, 1290 (2007).

[Sa02] Nickel-doped Nanocrystalline Glass-ceramic Fiber: B. N. Samson, L. R. Pinckney, J. Wang, G. H. Beall, N. F. Borelli. Optics Letters 27, 1309 (2002).

[Sc05] Complete Cancellation of Noise by Means of Color-Locking in Nearly Degenerate, Four-wave Mixing of Noisy Light: T. F. Schulz, P. P. Aung, L. Weisel, K. Cosert, M. W. Gealy, D. J. Ulness. Journal of the Optical Society of America B 22, 1052 (2005).

[Sc08] Probing the Gold Nanorod-Ligand-Solvent Interface by Plasmonic Absorption and Thermal Decay: A. J. Schmidt, J. D. Alper, M. Chiesa, G. Chen, S. K. Das, K. Hammad-Schifferli. Journal of Physical Chemistry C 112, 13320 (2010).

[Sh86] Femtosecond Studies of Nonequilibrium Electronic Processes in Metals: R. W. Schoenlein, W. Z. Lin, J. G. Fujimoto, G. L. Eesley. Physical Review Letters 58, 1680 (1987).

[Sk92] Time-resolved Low Temperature Luminescence of Non-Bridging Oxygen Hole Centers in Silica Glass: L. Skuja. Solid State Communications 84, 613 (1992).

[Sk05] Defects in Oxide Glasses: L. Skuja, M. Hirano, H. Hosono, K. Kajihara. Physica Status Solidi (c) 2, 15 (2005).

[So05] Overcoming Computational Uncertainties to Reveal Chemical Sensitivity in Single Molecule Conduction Calculations: G. C. Solomon, J. R. Reimers, N. S. Hush. The Journal of Chemical Physics 122, 224502 (2005).

[Sö01] Plasmons in Metal Nanostructures: Carsten Sönnichsen. Ph.D. Thesis. Ludwig-Maximilians-University of Munich (2001).

[Sö02a] Drastic Reduction of Plasmon Damping in Gold Nanorods: C. Sönnichsen, T. Franzl, T. Wilk, G. von Plessen, J. Feldmann, O. Wilson, P. Mulvaney. Physical Review Letters 88, 077402-1 (2002).

[Sö02b] Plasmon Resonances in Large Noble-Metal Clusters: C. Sönnichsen, T. Franzl, T. Wilk, G. von Plessen, J. Feldmann. New Journal of Physics 4, 93 (2002).

[St00] Decay Times of Surface Plasmons in Metal Nanoparticles by Persistent Spectral Hole Burning: F. Stietz, J. Bosbach, T. Wenzel, T. Vartanyan, A. Goldmann, F. Träger. Physical Review Letters 84, 5644 (2000).

[St08] Transient Absorption Studies of Single Silver Nanocubes: H. Staleva, G. V. Hartland. The Journal of Physical Chemistry C Letters 112, 7535 (2008).

[Su94] Femtosecond-Tunable Measurement of Electron Thermalization in Gold: C.-K. Sun, F. Vallée, L. H. Acioli, E. P. Ippen, J. G. Fujimoto. Physical Review B 50, 15337 (1994).

[Su08] Formation Mechanism of Amorphous $TiO_2$ Spheres in Organic Solvents. 1. Roles of Ammonia: T. Sugimoto, T. Kojima. Journal of Physical Chemistry C 112, 18760 (2008).

[Sz96] Modern Quantum Chemistry: Introduction to Advanced Electronic Structure Theory: A. Szabo, N. S. Ostlund, Dover, Mineola (1996).

[Ta99] Laser-Induced Size Reduction of Noble Metal Particles: A. Takami, H. Kurita, S. Koda. Journal of Physical Chemistry B 103, 1226 (1999).

[Ti00] The Relationship between Structure and Transparency in Glass-ceramic Materials: P. A. Tick, N. F. Borelli, I. M. Reaney. Optical Materials 15, 81 (2000).

[To86] Ultrafast Pump-Probe Measurement Using Intensity Correlation of Incoherent Light: M. Tomita, M. Matsuoka. Journal of the Optical Society of America B 3, 560 (1986).

[Ts10] Charge-Transfer-Induced Structural Rearrangements at Both Sides of Organic/Metal Interfaces: T.-C. Tseng, C. Urban, Y. Wang, R. Otero, S. Tait, M. Alcami, D. Écjia, M. Trelka, J. Galego, N. Lin, M. Konuma, U. Starke, A. Nefedov, A. Langner, C. Wöll, M. A. Herranz, F. Martín, N. Martín, K. Kern, R. Miranda. Nature Chemistry 2, 374 (2010).

[Ul96] Four-Wave Mixing in a Bloch Two-Level System with Incoherent Laser Light Having a Lorentzian Spectral Density: Analytic Solution and a Diagrammatic Approach. D. J. Ulness, A. C. Albrecht. Physical Review A 53, 1081 (1996).

[Ul98] Electron Emission from Strongly Excited Metal Clusters: C. A. Ulrich, P. –G. Reinhard, E. Suraud. Physical Review A 57, 1938 (1998).

[Ul03] On the Role of Classical Field Time Correlations in Noisy Light Spectroscopy: Color Locking and a Spectral Filter Analogy: D. J. Ulness. Journal of Physical Chemistry A 107, 8111 (2003).

[Va99] Femtosecond Optical Second Harmonic Generation by Metal Clusters: the Influence of Inhomogeneous Line Broadening on the Dephasing Time of Surface Plasmon Excitation: T. Vartanyan, M. Simon, F. Träger. Applied Physics B 68, 425 (1999).

[Va01] Theory of Spectral Hole Burning for the Study of Ultrafast Electron Dynamics in Metal Nanoparticles: T. Vartanyan, J. Bosbach, F. Stietz, F. Träger. Applied Physics B 73, 391 (2001).

[Va07] Phonon Coupling of Non-Bridging Oxygen Hole Center with the Silica Environment: Temperature Dependence of the 1.9 eV Emission Band: L. Vaccaro, M. Cannas, R. Boscaino. Journal of Luminescence 128, 1132 (2008).

[Va08] Luminescence of the Surface Nonbridging Oxygen Hole Center in Silica: Spectral and Decay Properties: L. Vaccaro, M. Cannas, V. Radzig, R. Boscaino. Physical Review B 78, 075421 (2008).

[Ve10] Influence of Particle-Substrate Interaction on Localized Plasmon Resonances: K. C. Vernon, Alison M. Funston, C. Novo, D. E. Gómez, P. Mulvaney, T. J. Davis. Nano Letters 10, 2080 (2010).

[Vi05] Sum-Frequency Generation Spectroscopy of Interfaces: F. Vidal, A. Tadjeddine. Reports on Progress in Physics 68, 1095 (2005).

[Vo94] Review of the Finite-Element Method for Three-Dimensional Electromagnetic Scattering: J. L. Volakis, A. Chatterjee, L. C. Kempel. Journal of the Optical Society of America A 11, 1422 (1994).

[Vo00] Size-Dependent Electron-Electron Interactions in Metal Nanoparticles: C. Voisin, D. Christofilos, N. Del Fatti, F. Vallée, B. Prével, E. Cottancin, J. Lermé, M. Pellarin, M. Broyer. Physical Review Letters 85, 2200 (2000).

[Vo01] Ultrafast Electron Dynamics and Optical Nonlinearities in Metal Nanoparticles: C. Voisin, N. Del Fatti, D. Christofilos, F. Vallée. Journal of Physical Chemistry B 105, 2264 (2001).

[Vo04] Ultrafast Electron-Electron Scattering and Energy Exchange in Noble Metal Nanoparticles: C. Voisin, D. Christofilos, P. A. Loukakos, N. Del Fatti, F. Vallée, J. Lermé, M. Gaudry, E. Cottancin, M. Pellarin, M. Broyer. Physical Review B 69, 195416 (2004).

[Vö89] Hole-Burning Spectroscopy: S. Völker. Annual Review of Physical Chemistry 40, 499 (1989).

[Wa03] Nanomaterials and Singlet Oxygen Photosensitezers: Potential Applications in Photodynamic Therapy: S. Wang, R. Gao, F. Zhou, M. Selke. Journal of Materials Chemistry 14, 487 (2004).

[We85] Three-Pulse Scattering for Femtosecond Dephasing Studies: Theory and Experiment: A. M. Weiner, S. de Silvestri, E. P. Ippen. Journal of the Optical Society of America B 2, 654 (1985).

[We09] Ultrafast Optics: A. M. Weiner. Wiley, New Jersey (2009).

[Wi07] Localized Surface Plasmon Resonance Spectroscopy and Sensing: K. A. Willets, R. P. Van Duyne. Annual Review of Physical Chemistry 58, 267 (2007).

[Wo95] Femtosecond Dephasing in CdS Quantum Dots Determined by Nondegenerate Four-wave Mixing: U. Woggon, M. Portuné. Physical Review B 51, 4719 (1995).

[Wo97] Optical Properties of Semiconductor Quantum Dots: U. Woggon. Springer, Berlin (1997).

[Xu08] Noise Autocorrelation Spectroscopy with Coherent Raman Scattering: X. G. Xu, S. O. Konorov, J. W. Hepburn, V. Milner. Nature Physics 4, 125 (2008).

[Ya92] Landau Damping and Wall Dissipation in Large Metal Clusters: C. Yannouleas, R. A. Broglia. Annals of Physics 217, 105 (1992).

[Ye66] Numerical Solution of Initial Boundary Value Problems Involving Maxwell’s Equation in Isotropic Media: K. S. Yee. IEEE Transactions on Antennas and Propagation 14, 302 (1966).

[Yi04] Zinc Oxide Quantum Rods: M. Yin, Y. Gu, I. L. Kuskovsky, T. Andelman, Y. Zhu, G. F. Neumark, S. O’Brien. Journal of the American Chemical Society 126, 6206 (2004).

[Za10] A Bright Future for Glass-ceramics: E. D. Zanotto. American Ceramic Society Bulletin 89, 19 (2010).

[Zh08] Methods for Describing the Electromagnetic Properties of Silver and Gold Nanoparticles: J. Zhao, A. O. Pinchuk, J. M. Mcmahon, S. Li, L. K. Ausman, A. L. Atkinson, G. C. Schatz. Accounts of Chemical Research 41, 1710 (2008).

[Zh04] Phase Transformation in $Na_2O$-$K_2O$-$Nb_2O_5$-$SiO_2$ glasses: A. A. Zhilin, G. T. Petrovsky, V. V. Golubkov, A. A. Lipovskii, D. K. Tagantsev, B. V. Tatarintsev, M. P. Shepilov. Journal of Non-Crystalline Solids 345-346, 182 (2004).

[Zi04] Dephasing Times of Surface Plasmon Excitation in Au Nanoparticles Determined by Persistent Spectral Hole Burning. T. Ziegler, C. Hendrich, F. Hubenthal, T. Vartanyan, F. Träger. Chemical Physics Letters 386, 319 (2004).

[Zi09] Five-dimensional Optical Recording Mediated by Surface Plasmons in Gold Nanorods. P. Zijlstra, J. W. M. Chon, M. Gu. Nature 459, 410 (2009).